

Superconductivity in strongly correlated systems: Heavy fermions, Cuprates, Infinite-layer Nickelates

A dissertation
submitted in partial fulfillment
of the requirements for the award of the
degree of
Doctor of Philosophy

by
Priyo Adhikary



Department of Physics
Indian Institute of Science
Bangalore - 560012

Declaration

I, hereby, declare that this is original. I worked on this thesis under the supervision of my advisor Prof. Tanmoy Das, Department of Physics, Indian Institute of Science Bangalore.

Priyo Adhikary

Indian Institute of Science,
Bangalore,
July, 2021.

Prof. Tanmoy Das
(Research advisor)

Abstract

The phase diagrams of the heavy fermion, transition-metal (copper-, nickel-) oxides materials have a wide variety of different phases. It is believed that, the strong correlation among electrons governs most of the phases in these materials, and hence, they are called strongly correlated systems. The purpose of the thesis is to understand the microscopic origin of the superconductivity in the strongly correlated systems and subsequently compare/predict the experimental outcomes of the theory. It is well known that heavy fermion, transition-metal oxide systems are unconventional superconductors. However, contrary to the old results, new experiments performed on the heavy fermion systems point towards a fully gapped conventional superconductivity. Similarly, in the cuprate superconductors, the d -wave symmetry of the superconducting order parameter is well known in the copper-oxide layer. However, counter-evidence of nodeless superconductivity is observed in the underdoped region of cuprates. Recently superconductivity is observed in infinite-layer nickelates NdNiO_2 and PrNiO_2 , a maximum $T_c \sim 15$ K. Based on the above-mentioned experimental motivations, we formulate a new mechanism of superconductivity in the heavy fermion system where attractive potential between impurity and conduction electrons are mediated by emergent boson fields in the slave-boson theory. We developed a self-consistent theory for the superconducting gap and found good agreement with experimental results. We found a s -wave like, fully gapped superconducting channel. For the cuprates and nickelates, we use spin-fluctuation mediated pairing potential, with multi-band random phase approximation to predict pairing symmetries of the gap function. In YBCO cuprate, we found that, if we dope the CuO chain state while keeping

the CuO_4 plane state's doping fixed, the pairing symmetry change from the nodal d -wave to a nodal f -wave symmetry. We explore superconductivity in $R\text{NiO}_2$ ($R = \text{Nd, La, Pr}$), based on two orbitals, Ni $d_{x^2-y^2}$, and R axial orbital. The axial orbital consists of Nd/La d , and Ni d_{z^2} orbitals. We found that the superconductivity is orbital-selective in $R\text{NiO}_2$. In this thesis, we use analytical and numerical methods to analyse the superconducting properties relevant from theoretical and experimental perspectives.

Dedicated to my family.

Acknowledgments

I want to thank my thesis advisor, Prof. Tanmoy Das, for the continuous support and guidance during my PhD. I have learnt many theoretical and numerical concepts from the weekly discussion meetings and many unannounced meetings with him. His dedication to physics and work ethics is very inspirational. I am thankful to our past and present group members- Sujay, Gaurav, Partha, Yogendra, Ananya, Priyanshi, Suman for helping me understand critical physical concepts.

During my PhD, I collaborated with various experimental and theoretical groups. I am incredibly thankful to Prof. Anindya Das (IISc), Prof. Sumilan Banerjee (IISc), Prof. Goutam Sheet (IISER Mohali). I am also grateful to Prof. Indra Dasgupta (IACS), Prof. Tanusri Saha-Dasgupta (SNBNCBS). I had an excellent experience working with Chandan Kumar, Saurabh Kumar Srivastav. I acknowledge the assistance of Subhadeep Bandyopadhyay (IACS) in clarifying concepts.

My friends at IISc and especially in the physics department helped me a lot during the difficult times. Indrajit, Debarghya, Moid, Vikas, Mahesh, Arun, Subhodeep have all great support.

Finally, I am thankful to my family, my father (Gopal Adhikary) and sister (Sneha Adhikary), for their love and encouragement. I want to dedicate this thesis to the loving memories of my mother (Nita Adhikary).

List of Publications

A. Included in this thesis:

- (1) **Priyo Adhikary**, Tanmoy Das, *Novel attractive pairing interaction in strongly correlated superconductors*, SciPost Phys. **7**, 078 (2019).
- (2) **Priyo Adhikary**, Tanmoy Das, *Prediction of f-wave pairing symmetry in $YBa_2Cu_3O_{6+x}$ cuprates*, Phys. Rev. B **101**, 214517(2020).
- (3) **Priyo Adhikary**, Subhadeep Bandyopadhyay, Tanmoy Das, Indra Dasgupta, Tanusri Saha-Dasgupta, *Orbital Selective Superconductivity in a Two-band Model of Infinite-Layer Nickelates*, Phys. Rev. B **102**, 100501(R)(2020).
- (4) Subhadeep Bandyopadhyay, **Priyo Adhikary**, Tanmoy Das, Indra Dasgupta, Tanusri Saha-Dasgupta, *Superconductivity in Infinite-layer Nickelates : Role of f orbital*, Phys. Rev. B **102**, 220502(R)(2020).

B. Not included in this thesis:

- (1) Chandan Kumar, Saurabh Kumar Srivastav, **Priyo Adhikary**, Sumilan Banerjee, Tanmoy Das, and Anindya Das, *Localization physics in graphene moire' superlattices*, Phys. Rev. B **98**, 155408,(2018).
- (2) Anshu Sirohi, Shekhar Das, **Priyo Adhikary**, Rajeswari Roy Chowdhury, Amit Vashist, Yogesh Singh, Sirshendu Gayen, Tanmoy Das, Goutam Sheet, *Mixed type I and type II superconductivity due to intrinsic electronic inhomogeneities in the type II Dirac semimetal $PdTe_2$* , J. Phys. Condens. Matter **31**, 085701 (2019).

Contents

1	Introduction	2
1.1	Correlated materials	2
1.2	Heavy fermion superconductors	3
1.3	Anderson impurity model	5
1.3.1	The Kondo model	7
1.3.2	The Doniach model	8
1.3.3	Scaling renormalization group	11
1.3.4	Numerical renormalization group	15
1.3.5	Slave-Boson method	20
1.4	transition-metal oxides superconductors	26
1.5	Infinite-layer Nickelates	28
1.6	Spin-fluctuation theory	31
1.6.1	Spin-fluctuation mediated pairing in one band Hubbard model	33
1.6.2	Spin-fluctuation potential in the multi-band Hubbard model	37
2	Novel attractive pairing interaction in heavy fermions	41
2.1	Introduction	41
2.2	Field theory treatment of the hole states and effective attractive potential	44
2.3	Mean-field results and critical phenomena	49
2.3.1	Transition temperature T_c	50
2.3.2	SC gap amplitude	51
2.3.3	Numerical solution of SC gap and transition temperature . .	51
2.3.4	Connection to coherence temperature T_K	55

2.4	Signatures of pairing structure.	55
2.4.1	Pair susceptibility	55
2.4.2	Meissner effect	58
2.4.3	Spin-resonance mode	63
2.4.4	Other measurements	67
2.5	Discussions and conclusions	68
3	Prediction of f-wave pairing symmetry in $\text{YBa}_2\text{Cu}_3\text{O}_{6+x}$ cuprates	72
3.1	Introduction	72
3.2	Tight binding model	74
3.2.1	Multi-band RPA susceptibility	77
3.3	Results	78
3.3.1	Electronic structure	78
3.3.2	Evolution of FS nesting with chain doping	80
3.3.3	Superconducting properties	83
3.4	Discussions and Conclusions	86
4	Orbital-selective superconductivity of infinite-layer nickelates	90
4.1	Introduction	90
4.2	Two-band model	91
4.3	Results	94
4.3.1	Evolution of nesting in nickelates	94
4.3.2	Calculation of SC properties	97
4.3.3	Spectral function	100
4.4	Doping dependence	102
4.5	Discussions and Conclusions	105
5	Conclusions	108
A	S-matrix expansion of the Kondo model	110
B	RPA spin and charge fluctuations from the Hubbard model	116

Chapter 1

Introduction

1.1 Correlated materials

Correlated materials are defined by those where the electron-electron interactions dominate the kinetic energy terms and govern novel emergent properties at low temperature and extreme conditions. Typically, materials with outer shell electrons residing in the s , p -orbitals are prone to weak coupling. In contrast, d -electrons materials such as transition-metal compounds possess intermediate coupling (where Coulomb repulsion is of the order of electronic bandwidth) [1]. Materials with f -electrons on the outer shells, called heavy fermions, generally reside in the strong coupling region [2, 3]. In the weak and strong coupling regions, one can approach the problem perturbatively, starting from the kinetic energy term and the interaction term, respectively. However, in the intermediate coupling regions, there is no obvious perturbation term. A trademark of the intermediate coupling region is that the electronic spectrum splits into itinerant quasiparticles near the Fermi level and localized electrons at higher energy. The interaction between the itinerant and local electrons is also a canonical behaviour of the heavy fermion compounds, where the itinerant and local electrons stem from conduction (s , p , d) and f -orbitals, respectively. The spectral weight transfer or valence fluctuation between the itinerant and local electrons, obtained by doping, pressure, strain, etc., govern a number of emergent properties such as non-Fermi liquid behaviour, unconventional superconductivity, magnetism, Kondo physics, etc [see Fig. 1.1]

[2, 3, 4, 5]. The present thesis is mainly focused on understanding unconventional superconductivity in the intermediate coupling region of various transition-metal oxides (cuprates, newly discovered infinite-layer nickelates) and the valence fluctuation region of the heavy fermion compound CeCu_2Si_2 .

The discovery of superconductivity in heavy fermion and transition-metal oxides in the '80s shows the importance of electron correlation. In these systems, electron-phonon interaction is very weak compared to the Coulomb repulsion. The superconducting order parameter was found to be anisotropic and nodal in the momentum space, in contrast to the isotropic order parameter of the Bardeen-Cooper-Schrieffer (BCS) theory [6]. Many theoretical models were proposed, including the Hubbard model, Heisenberg model, t - J model, and periodic Anderson model, which describe the quantum phase transition using different tuning parameters of the theory, e.g. onsite Coulomb interactions, intra-inter orbital Hubbard interactions, hopping parameter/bandwidth [2, 3, 4, 7, 8, 9]. The correlation effect is more pronounced at low temperatures, where the many-body ground state is highly degenerate. Thermal fluctuation is very weak at very low temperature, and the quantum fluctuation dominates the phase transition. In this regime, the tuning parameters that drive phase transitions are chemical doping, pressure, magnetic field etc. It is often found that as the magnetic phase is suppressed with these tuning, superconductivity arises.

1.2 Heavy fermion superconductors

We start with the heavy fermion, intermetallic, mixed-valence systems, where f -electrons come from rare-earth or actinide elements, and conduction electrons from the same compound or from other weakly correlated elements. The conduction band has an odd number of electrons, while the f electrons give rise to the local moments. In the heavy fermion systems, the Sommerfeld coefficient, $\gamma = \frac{c_v}{T} \sim 1400 \text{ mJ/molK}^2$, (γ for Cu is 1 mJ/molK^2 [10]). The magnetic susceptibility at high temperature has a Curie like behaviour, and at low temperature, it is constant (Pauli paramagnetism). These heavy fermion systems usually have $4f$ or $5f$ orbitals at their outermost configuration, e.g. electronic configurations of Ce^{+3}

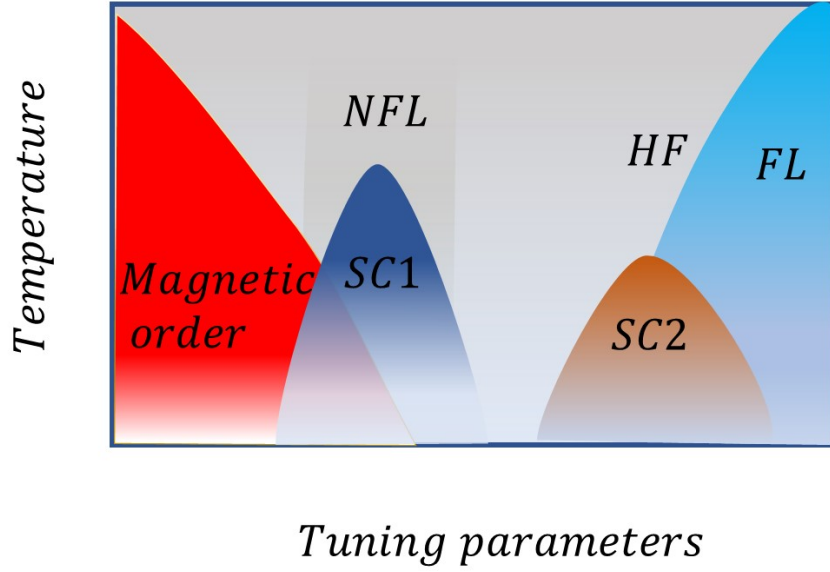


Figure 1.1: Schematic low temperature phase diagram of a heavy fermion system. Tuning parameter can be doping, pressure, magnetic field. FL (NFL) \equiv Fermi liquid (non-Fermi liquid), SC \equiv superconductivity, HF \equiv heavy fermion metal.

and U^{+1} are $4f^1$, $5f^3$ in CeCu_2Si_2 and URu_2Si_2 respectively. Many of these materials become superconductors and are called heavy fermion superconductors (HFSCs). The local moment of the heavy elements gives magnetism, which coexists or competes with superconductivity. We show a schematic phase diagram of HFSC in Fig. 1.1. The superconducting T_c dome often arises around a quantum critical point (QCP) [3], as also seen in cuprates and iron pnictides [4]. With further tuning, the single SC dome often splits into two domes, one near the QCP and the other away from it. A dominant part of the normal state above the first SC dome is Fermi liquid (FL) like, while the second dome often has a non-Fermi liquid (NFL) state.

Commonly studied HFSC families can be grouped into the following categories. **Cerium-122** : CeCu_2Si_2 is the first known HFSC discovered by Steglich *et. al* (1979) [11, 2]. Soon after many Cerium, Uranium based superconductors were reported e.g. CeRh_2Si_2 of $T_c = 0.3$ K at critical pressure (P_c) = 9 kbar, CePd_2Si_2

($T_c = 0.43$ K), CeCu_2Ge_2 ($T_c = 0.6$ K). In the Ce-122 family, tuning parameters are pressure or chemical doping and magnetic order; the magnetic order is mainly an antiferromagnetic phase. Another Ce based HFSC family is $\text{Ce}T\text{In}_5$ ($T = \text{Ir, Co, Cu, Rh}$). T_c of CeCoIn_5 is 2.3 K, at ambient pressure, however $P = 21$ kbar is required to obtain superconductivity in CeRhIn_5 .

Uranium : In UCoGe ($T_c = 0.8$ K), a superconducting dome is recorded below the ferromagnetic phase (below 3 K) [3]. Other Uranium based HFSC includes UBe_{13} ($T_c = 0.9$ K), URu_2Si_2 ($T_c = 1.2$ K) [2], UPt_3 ($T_c = 0.5$ K) [12].

Plutonium : Recently, Pu based HFSC, in PuCoGa_5 ($T_c = 18.5$ K) , PuRhGa_5 ($T_c = 8.6$ K), PuCoIn_5 ($T_c = 2.5$ K), PuRhIn_5 ($T_c = 1.7$ K) were discovered [13]. Magnetic order is either absent or weak in these materials.

Ytterbium : Superconductivity was also reported in Ytterbium based mixed-valence compound $\beta\text{-YbAlB}_4$ [14] with $T_c = 80$ mK [15]; also in YbRh_2Si_2 with $T_c = 1$ mK [16]. These materials exhibit NFL behaviour without any tuning.

1.3 Anderson impurity model

We briefly review two models for the HF compounds, namely the Anderson impurity model (AIM) and the Kondo model, and how they are related. In HF systems, localized f -electrons give local moments, where conduction electrons provide Fermi surface (FS). The interaction between the two states, either in terms of Kondo coupling between local and itinerant spins or via the charge/valence fluctuation between them, giving mixed-valence states. The latter is described by the Anderson impurity model, proposed by P. W. Anderson in 1961 [17]. He wrote down a model which includes onsite Coulomb interaction between the f -electrons and tunnelling between local and conduction electrons. The conduction (c) electrons are the Bloch states in a lattice, and the localized electron (f) acts as an impurity. Hybridization between the c and f -electrons is represented by $v_{\mathbf{k}}$.

The Hamiltonian of Anderson impurity model (AIM) is given by,

$$H = H_c + H_f + H_{cf}, \quad (1.3.1)$$

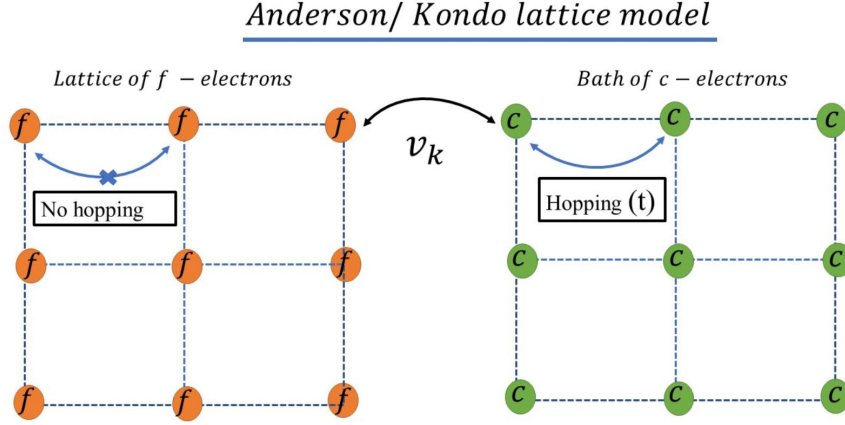


Figure 1.2: Schematic representation of Anderson lattice model. Since c -electrons number at a given site is not conserved, it is called the c -electron bath. However, the total number of f and c -electrons is conserved.

where,

$$H_f = \xi_f \sum_m f_m^\dagger f_m + U \sum_m f_m^\dagger f_m f_{-m}^\dagger f_{-m}, \quad (1.3.2)$$

$$H_c = \sum_{\mathbf{k}, \sigma} \xi_{\mathbf{k}} c_{\mathbf{k}\sigma}^\dagger c_{\mathbf{k}\sigma}, \quad (1.3.3)$$

$$H_{cf} = \sum_{\mathbf{k}, \sigma, m} v_{\mathbf{k}} c_{\mathbf{k}\sigma}^\dagger f_m + \text{h.c.} \quad (1.3.4)$$

$c_{\mathbf{k}\sigma}$, f_m are annihilation operators for the conduction electron and localized electron, respectively with momentum \mathbf{k} and spin level $\sigma = \pm 1/2$. Due to spin-orbit coupling total angular momentum of the f -electron has m multiplets. H_f is known as atomic level Hamiltonian. ξ_f is the onsite energy of the f -electron, U is the onsite Hubbard interaction. f -electron does not have any dispersion. H_c is the conduction electron Hamiltonian having a dispersion $\epsilon_{\mathbf{k}}$ and chemical potential μ ; $\xi_{\mathbf{k}} = \epsilon_{\mathbf{k}} - \mu$. Eigenstates of c -electrons are Bloch waves. H_{cf} is hybridisation between c - f electron. $v_{\mathbf{k}} = \int dr \psi_f^*(r) v(r) \psi_{\mathbf{k}}(r)$ [18], where ψ_f is orbital of the f -electron and $\psi_{\mathbf{k}}$ is the Bloch state of conduction electron.

The AIM can be solved in the (A) weak coupling ($U \rightarrow 0$) and (B) strong coupling limit ($U \sim$ very high).

(A) The weak coupling limit of the PAM describes a resonance of f -electron around the conduction electron, and form a virtual bound state (VBS). The non-interacting state is governed by a two orbital model. The eigen-energies are $E_{\mathbf{k}}^{\pm} = \xi_{\mathbf{k}} + \xi_f \pm \sqrt{(\xi_{\mathbf{k}} - \xi_f)^2 + v_{\mathbf{k}}^2}$, which opens a band gap (Δ) between two states.

$$\begin{aligned}\Delta &= E_{\mathbf{k}}^+ - E_{\mathbf{k}}^-, \\ &= 2\sqrt{(\xi_{\mathbf{k}} - \xi_f)^2 + v_{\mathbf{k}}^2}, \\ &\approx 2(\xi_{\mathbf{k}} - \xi_f) + \frac{v_{\mathbf{k}}^2}{(\xi_{\mathbf{k}} - \xi_f)}.\end{aligned}\tag{1.3.5}$$

This is called the non-interacting mixed-valence insulator. Resonance width of the VBS is given by hybridization function, [18],

$$\Delta_h(\omega) = \sum_{\mathbf{k}} \pi v_{\mathbf{k}}^2 N(\xi_{\mathbf{k}} - \omega).\tag{1.3.6}$$

Δ_h determines the effect of the c -electrons on the impurity energy level. The range of Δ_h lies within the conduction bandwidth (D), $-D < \Delta_h < D$. It also plays a fundamental role in the numerical renormalization group method in finding full spectra of the Kondo model.

(B) In the strong coupling limit, there are various model solutions of the AIM, (i) Kondo model, (ii) numerical renormalization group, (iii) Slave-Boson model.

1.3.1 The Kondo model

The mean-field solution of the Anderson model [17] describes the origin of the local moment when $U \gg |v|$ [18, 19]. The resonance at the Fermi level for the non-interacting model persists for $U \neq 0$, if we adiabatically tune the Coulomb interaction for a fixed f -electron density. This resonance is known as Kondo resonance [18]. The high energetic charge fluctuations can be eliminated by the Schrieffer-Wolf transformation [18, 19, 20, 21], resulting model is known as the

Kondo model [22].

$$\begin{aligned}
H_K = & \sum_{\mathbf{k}\sigma} \xi_{\mathbf{k}} c_{\mathbf{k}\sigma}^\dagger c_{\mathbf{k}\sigma} + \sum_{\mathbf{k},\mathbf{k}'} J_K(\mathbf{k}, \mathbf{k}') \vec{S}_f \cdot \vec{S}_c(\mathbf{k}, \mathbf{k}') + \frac{1}{4} \sum_{\mathbf{k},\mathbf{k}'} J_K(\mathbf{k}, \mathbf{k}') \rho_f c_{\mathbf{k}',\sigma'}^\dagger c_{\mathbf{k},\sigma} \\
& + \frac{1}{2} \sum_{\mathbf{k},\mathbf{k}',\sigma} \mathcal{J}_c(\mathbf{k}, \mathbf{k}') \rho_c(\mathbf{k}, \sigma) \rho_c(\mathbf{k}', -\sigma). \tag{1.3.7}
\end{aligned}$$

Where $\rho_f = \sum_m f_m^\dagger f_m$ and $\rho_c = \sum_{\mathbf{k},\sigma} c_{\mathbf{k},\sigma}^\dagger c_{\mathbf{k},\sigma} = \sum_{\mathbf{k},\sigma} \rho_c(\mathbf{k}, \sigma)$ are the number density of f and c -electrons. $\vec{S}_f = \sum_{m,m'=-j}^j f_m^\dagger \vec{\Gamma}_{m,m'} f_{m'}$ (j is the multiplets of impurity electrons) and $\vec{S}_c(\mathbf{k}, \mathbf{k}') = \sum_{\alpha\beta=\uparrow\downarrow} c_{\mathbf{k}\alpha}^\dagger \vec{\sigma}_{\alpha\beta} c_{\mathbf{k}'\beta}$ are the spin of impurity electron and conduction electron level. $\vec{\Gamma}, \vec{\sigma}$ are the spin operators. J_K is the Kondo exchange interaction,[18, 19, 21, 23]

$$J_K(\mathbf{k}, \mathbf{k}') = v_{\mathbf{k}} v_{\mathbf{k}'} \left[\frac{1}{\xi_f + U - \xi_{\mathbf{k}}} + \frac{1}{\xi_{\mathbf{k}} - \xi_f} + \frac{1}{\xi_f + U - \xi_{\mathbf{k}'}} + \frac{1}{\xi_{\mathbf{k}'} - \xi_f} \right]. \tag{1.3.8}$$

At the Fermi level, $J_K(\mathbf{k}, \mathbf{k}' = k_F) = -\frac{2Uv^2}{\xi_f(\xi_f+U)}$. [19] Therefore, if the impurity level is below the Fermi level, $\xi_f = -|\xi_f|$, Kondo coupling becomes positive, $J_K > 0$, and we have an antiferromagnetic coupling between the impurity spin and conduction spin. Otherwise interaction is ferromagnetic.

The third and fourth terms in Eq.(1.3.7) also arise from the Schrieffer-Wolf transformation [19]. The Kondo impurity model can be generalised to a Kondo lattice model [see Fig. 1.2]; this was first suggested by S. Doniach [24] to study antiferromagnetism in the HF systems.

1.3.2 The Doniach model

The Kondo lattice model is described by the (a) Kondo interaction between the spin of the impurity electron and the spin of the conduction electron, and (b) the RKKY interaction (Ruderman-Kittel-Kasuya-Yosida)[25, 26, 27], which describes the interaction between neighbouring impurity spins via the intermediate conduction electrons. As an impurity spin is emerged in the conduction electron bath, the magnetic moment around it is screened. Therefore, effective spin-spin interaction is reduced in the same way as the Coulomb interaction is screened via the Thomas-Fermi mechanism [28]. The effective spin-spin interaction ($\phi(r)$) is cosi-

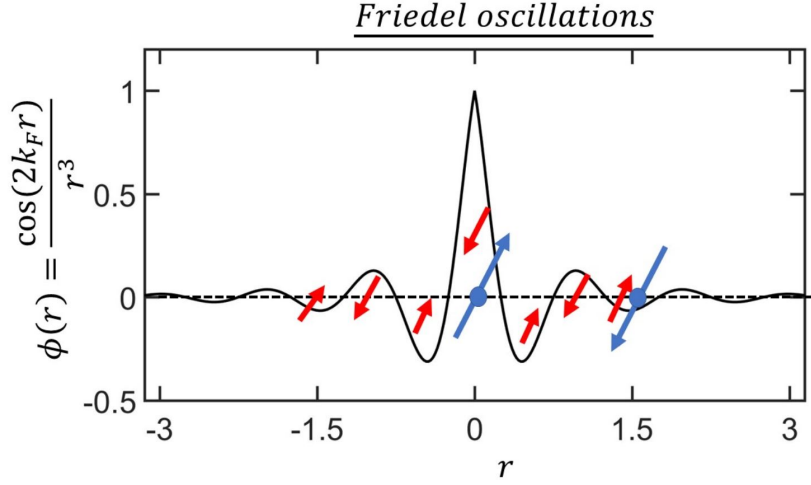


Figure 1.3: Schematic diagram of Friedel oscillations of the effective interaction between impurity spin and conduction electron bath. Red arrows represent the spin of conduction electrons, and blue arrows denote the impurity spin. Here we illustrate the RKKY interaction between two impurity spins mediated by conduction electrons spins.

oscillatory, but amplitude decreases from the impurity position, $\phi(r) = \frac{\cos(2k_F r)}{r^3}$ [see Fig. 1.3] [18, 29]; r is the distance from magnetic impurity and k_F is the Fermi momentum of the conduction electrons. This oscillatory behaviour of effective screened interaction is called the Friedel oscillation. The average magnetic moment of the impurity due to screening is given as [18] $\langle \vec{M} \rangle = -J_K \chi_0(\mathbf{q}, \omega) \langle \vec{S}_f \rangle$, where Lindhard susceptibility of the conduction electron is given by,

$$\begin{aligned} \chi_0(\mathbf{q}, i\omega_n) &= \int_0^\beta d\tau e^{-i\omega_n \tau} \langle S_c(\mathbf{q}, \tau) S_c(-\mathbf{q}, 0) \rangle, \\ &= \frac{1}{\Omega_{BZ}} \sum_{\mathbf{k}} \frac{f(\xi_{\mathbf{k}+\mathbf{q}}) - f(\xi_{\mathbf{k}})}{\xi_{\mathbf{k}+\mathbf{q}} - \xi_{\mathbf{k}} - i\omega_n}. \end{aligned} \quad (1.3.9)$$

Where $\xi_{\mathbf{k}}$ is the dispersion of conduction electrons, $f(\xi_{\mathbf{k}}) = \frac{1}{e^{\beta \xi_{\mathbf{k}}} + 1}$ is the Fermi distribution function. and Ω_{BZ} is the area of the Brillouin zone (BZ). We use the Matsubara summation in the last step of Eq. (1.6.9). After performing analytic continuation in real frequency (ω), $i\omega_n \rightarrow \omega + i\eta$ (η is small positive number) we

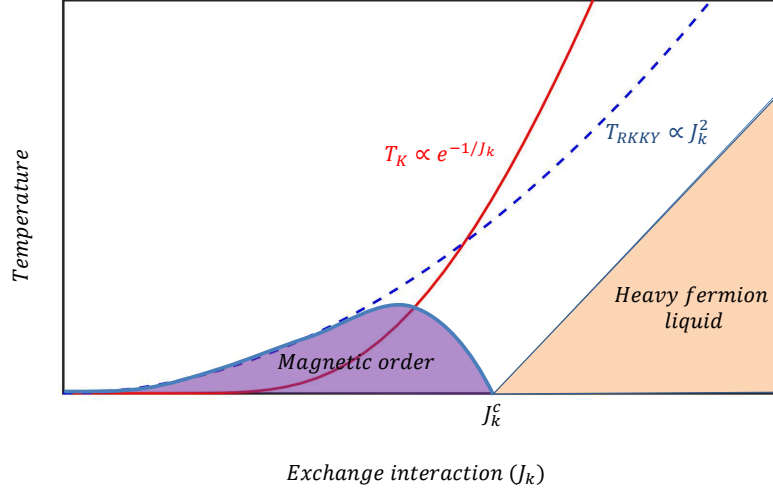


Figure 1.4: Schematic representation of Doniach phase diagram.

obtain the Lindhard susceptibility,

$$\chi_0(\mathbf{q}, \omega) = \frac{1}{\Omega_{BZ}} \sum_{\mathbf{k}} \frac{f(\xi_{\mathbf{k}+\mathbf{q}}) - f(\xi_{\mathbf{k}})}{\xi_{\mathbf{k}+\mathbf{q}} - \xi_{\mathbf{k}} - \omega - i\eta}. \quad (1.3.10)$$

In the RKKY interaction, impurity spins interact with the average moment due to the Friedel oscillation of screened potential between impurity and conduction electrons,

$$H_{RKKY} = \sum_{\langle i,j \rangle} J_{RKKY} \vec{S}_f^i \cdot \vec{S}_f^j, \quad (1.3.11)$$

where the exchange coupling is given by,

$$J_{RKKY} = J_K^2 \chi_0(\mathbf{q}, \omega). \quad (1.3.12)$$

At long wavelength limit $\mathbf{q} \rightarrow 0$ ($\omega = 0$), $\chi_0(\mathbf{q} \rightarrow 0, \omega = 0) \approx N(E_F)$, $N(E_F)$ being density of states (DOS) of the conduction electrons at the Fermi level. Therefore,

$J_{RKKY} \sim N(E_F)J_K^2$, which is shown in Fig. 1.4, along with Kondo temperature (T_K). This is called the Doniach phase diagram [18, 24], where RKKY interaction and Kondo coupling competes, giving an antiferromagnetic dome when $J_{RKKY} > J_K$ and a Fermi liquid phase otherwise.

1.3.3 Scaling renormalization group

The effect of strong Coulomb interactions between impurity electrons, on the conduction electron can be given by the many body Greens function of the conduction electron. The perturbation series of J_K can be calculated from the S-matrix expansion of the Kondo Hamiltonian [see Appendix A] [18, 19, 30]. From the Dyson equation, we get,

$$\mathcal{G}(\mathbf{k}, \mathbf{k}', i\omega_n) = \delta_{\mathbf{k}, \mathbf{k}'} \mathcal{G}_0(\mathbf{k}, i\omega_n) + \mathcal{G}_0(\mathbf{k}, i\omega_n) \Sigma(\mathbf{k}, \mathbf{k}', i\omega_n) \mathcal{G}_0(\mathbf{k}', i\omega_n). \quad (1.3.13)$$

The three lowest order terms in the Dyson series are shown in Fig. 1.5. Since the non-interacting part of the Hamiltonian in Eq. (1.3.7) does not depend on the local spin, there is no first-order term in S-matrix, $\Sigma^{(1)}(\mathbf{k}, \mathbf{k}', i\omega_n) = 0$. The second-order term in the self-energy is given by [30],

$$\Sigma^{(2)}(\mathbf{k}, \mathbf{k}', i\omega_n) = \frac{3J_K^2}{16} \sum_{\mathbf{p}} \mathcal{G}_0(\mathbf{p}, i\omega_n). \quad (1.3.14)$$

In the second and higher-order terms in the self-energy, no Fermion loop contributes. There is no spin-fluctuation term present in the non-interacting ground state, and at each vertex, total spin conservation is done by taking trace over Pauli matrices, $\text{Tr}[\vec{\sigma}] = 0$.

The third-order term in self-energy is given by,

$$\Sigma^{(3)}(\mathbf{k}, \mathbf{k}', i\omega_n) = -\frac{3J_K^3}{4\beta^3} \sum_{p_n, q_n, \omega_n} \sum_{\mathbf{p}, \mathbf{q}} \int d\tau_1 d\tau_2 \left[\mathcal{G}_0(\mathbf{p}, ip_n) \mathcal{G}_0(\mathbf{q}, iq_n) \frac{2}{i\omega_n} \right] e^{-ip_n(\tau_1 - \tau_2)} e^{-iq_n\tau_3} e^{ik_n\tau_1} e^{i\omega_n(\tau_1 - \tau_2)}. \quad (1.3.15)$$

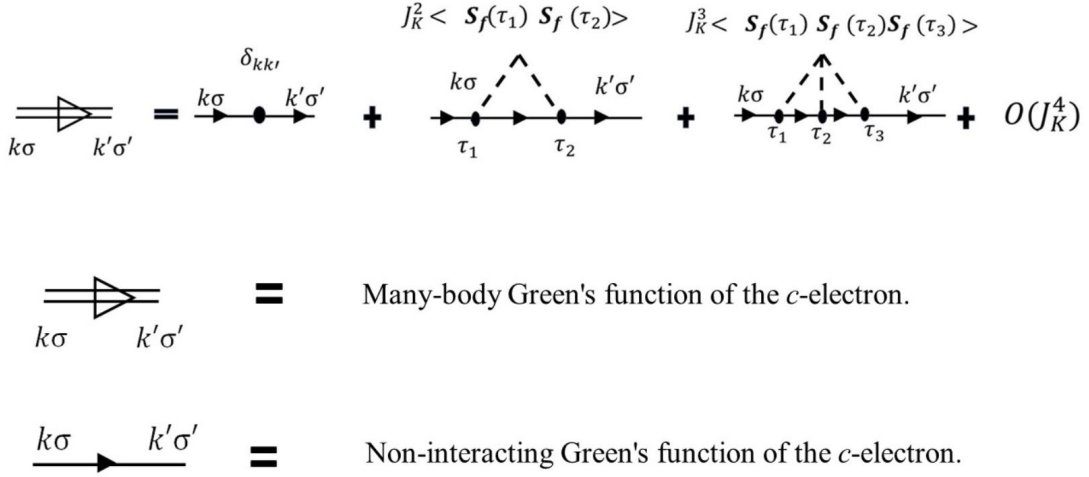


Figure 1.5: Feynman diagram of the many-body Green's function of conduction electron.

After doing the Matsubara summation on the p_n frequencies, we obtain [30]

$$\Sigma^{(3)}(\mathbf{k}, \mathbf{k}', i\omega_n) = \frac{3J_K^3}{4} \sum_{\mathbf{p}, \mathbf{q}} \frac{1 - 2f(\xi_{\mathbf{q}})}{\xi_{\mathbf{p}} - \xi_{\mathbf{q}}} \mathcal{G}(\mathbf{p}, i\omega_n). \quad (1.3.16)$$

Therefore, total self-energy up to third order of J_K ,

$$\begin{aligned} \Sigma(\mathbf{k}, \mathbf{k}', i\omega_n) &= \Sigma^{(2)}(\mathbf{k}, \mathbf{k}', i\omega_n) + \Sigma^{(3)}(\mathbf{k}, \mathbf{k}', i\omega_n), \\ &= \frac{3}{4} \sum_{\mathbf{p}} \mathcal{G}_0(\mathbf{p}, i\omega_n) \left[J_K^2 + J_K^3 \sum_{\mathbf{q}} \frac{1 - 2f(\xi_{\mathbf{q}})}{\xi_{\mathbf{p}} - \xi_{\mathbf{q}}} \right]. \end{aligned} \quad (1.3.17)$$

The imaginary part of the retarded self-energy ($\Sigma(\mathbf{k}, \mathbf{k}', \omega + i0^+)$) gives inverse lifetime ($\tau(\omega)$) of the conduction electrons, $\frac{1}{\tau(\omega)} = -\text{Im}\Sigma(\omega + i0^+)$, where 0^+ is the small positive quantity above the real axis. $\Sigma(\mathbf{k}, \mathbf{k}', \omega + i0^+)$ is obtained from $\Sigma(\mathbf{k}, \mathbf{k}', i\omega_n)$ by analytic continuation, $i\omega_n \rightarrow \omega + i0^+$

$$\text{Im}\Sigma(\mathbf{k}, \mathbf{k}', \omega + 0^+) = \frac{3}{4} \sum_{\mathbf{p}} \text{Im}\mathcal{G}_0(\mathbf{p}, \omega + 0^+) \left[J_K^2 + J_K^3 \sum_{\mathbf{q}} \frac{\tanh\left(\frac{\beta\xi_{\mathbf{q}}}{2}\right)}{\xi_{\mathbf{p}} - \xi_{\mathbf{q}}} \right]. \quad (1.3.18)$$

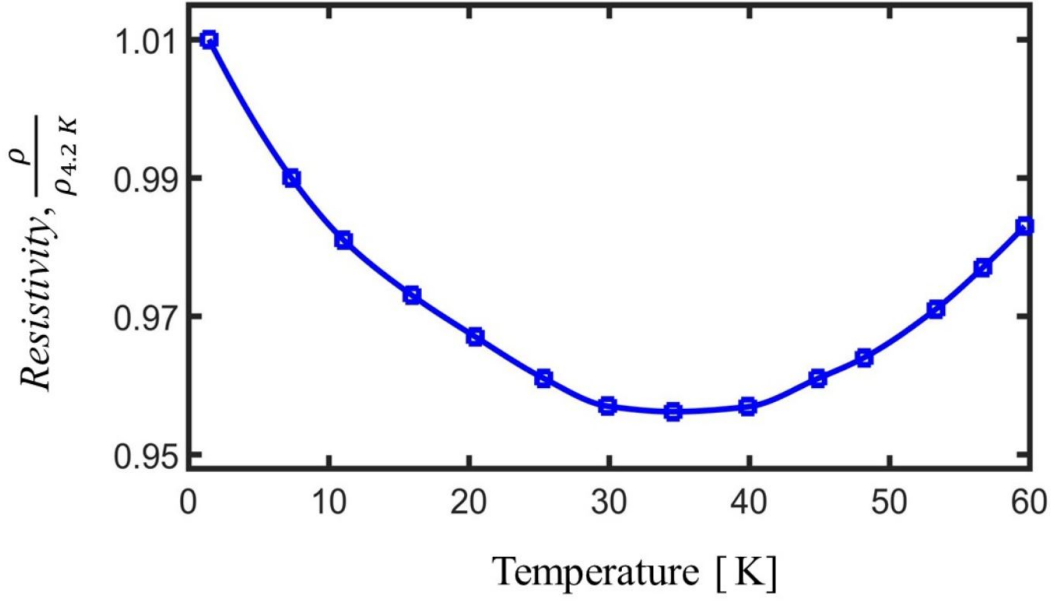


Figure 1.6: Temperature dependent resistivity (normalized with resistivity at 4.2 K) of $\text{Mo}_{1-x}\text{Nb}_x$ ($x = 0.1$). The resistivity minimum is the prominent feature of Kondo behaviour. The data used here is replotted from Ref.[31].

$\text{Im}\mathcal{G}_0(\mathbf{p}, \omega + 0^+) = -\pi\delta(\omega - \xi_{\mathbf{p}})$. The second term of Eq. (1.3.18) can be calculated by replacing the discrete momentum summation with continuous energy integration,

$$\text{Im}\Sigma^{(3)}(\mathbf{k}, \mathbf{k}', \omega) \sim \int_{-D}^D N(0)d\xi \frac{\tanh(\beta\xi/2)}{\omega - \xi} = N(0)\log\left[\frac{D_\gamma}{\sqrt{\omega^2 + (2k_B T)^2}}\right]. \quad (1.3.19)$$

$D_\gamma = 2D\gamma/\pi$ with $\gamma = 1.78$ being the Euler constant. The impurity scattering rate is given by,

$$\frac{1}{\tau(\omega)} = \frac{3\pi}{4} \sum_{\mathbf{p}} J_K^2 \delta(\omega - \xi_{\mathbf{p}}) \left[1 + J_K N(0) \log\left(\frac{D_\gamma}{\sqrt{\omega^2 + (2k_B T)^2}}\right) \right]. \quad (1.3.20)$$

The resistivity due to impurity scattering is proportional to $\frac{1}{\tau(\omega)}$. In Fig. 1.6 we show the experimental results of resistivity, which depicts a minimum due to the logarithmic temperature ($\log(1/T)$) dependence. However, $T \rightarrow 0$, $\log(1/T)$ diverges. The origin of the infra-red divergence is, $\sum_{\mathbf{q}} 1/\xi_{\mathbf{q}}$ dependence of $\text{Im}\Sigma$

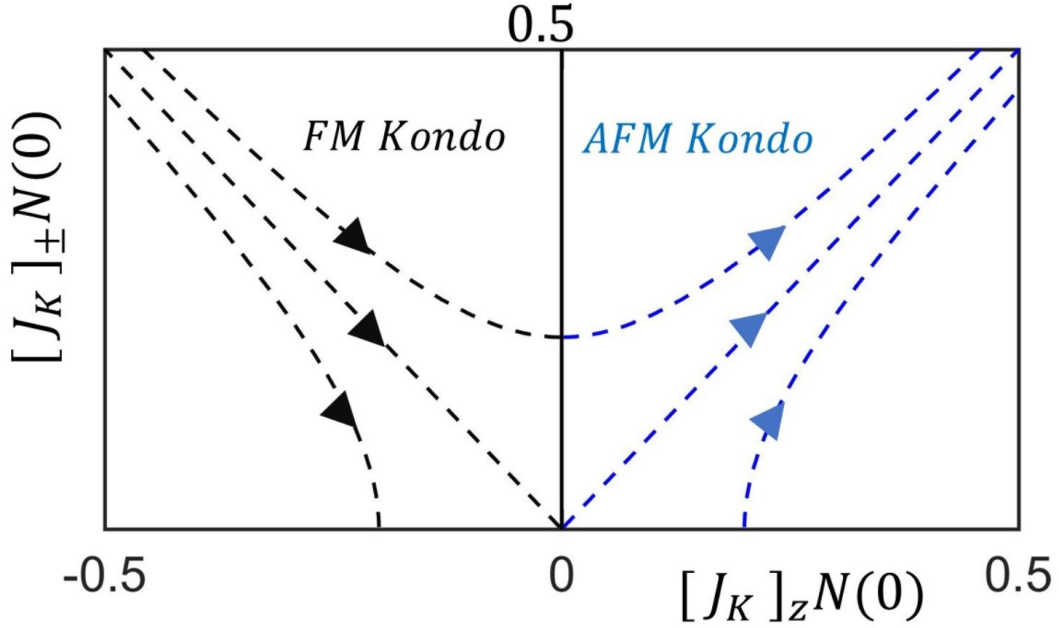


Figure 1.7: Poor man's scaling renormalization group flow diagram of the Kondo model.[23] **Attractive fixed point:** Antiferromagnetic coupling grows as we remove high energy mode $\pm D$ (bandwidth of the conduction electron). **Repulsive fixed point:** Ferromagnetic coupling becomes smaller and smaller, finally goes to zero along the line, $[J_K]_z = [J_K]_{\pm}$. $N(0)$ is the DOS at the Fermi level of the conduction electrons. $[J_K]_z$ and $[J_K]_{\pm}$ are Kondo coupling along z direction and at $x - y$ plane, between conduction electron and impurity spin.

in Eq.(1.3.18) and sharp FS ($\xi_{\mathbf{p}} = 0$) [32]. The divergence of the self-energy at $T = 0$ signifies that the perturbation theory is not valid at low temperature. In the following sections, we will discuss scaling theory and renormalization group theory to solve the Kondo problem.

Poor man's renormalization group

The poor man's renormalization group (RG) theory [18, 19] solves the Kondo problem by "integrating out" high energy modes, modes near bandwidth (D), and obtain scaling relation between coupling constants. From Eq. (1.3.18) we see that due to perturbation by Kondo interaction, Kondo coupling changes by, $J_K^2 \rightarrow J_K^2 + \delta(J_K^2)$. Where $\delta(J_K^2)$ is given by,

$$\delta(J_K^2) = \left[J_K^3 \sum_{\mathbf{q}} \frac{\tanh\left(\frac{\beta\xi_{\mathbf{q}}}{2}\right)}{\xi_{\mathbf{p}} - \xi_{\mathbf{q}}} \right], \quad (1.3.21)$$

[Here ' δ ' is used to indicate the variation or change.]

As we reach lower and lower temperature tanh term reaches to its maximum value,

1. At the Fermi level, $\xi_p = 0$, therefore we get from Eq. (1.3.21),

$$\delta(J_K) = -\frac{J_K^2}{2} \sum_{\mathbf{q}} \frac{1}{\xi_{\mathbf{q}}}. \quad (1.3.22)$$

The momentum summation can be transferred to integral over energy (ξ) and we restrict energy integral between $D - \delta D < \xi < D$. From Eq. (1.3.22) correction to Kondo coupling is

$$\delta(J_K) = J_K(D) - J_K(D') = -J_K^2 \int_{D'=D-\delta D}^D d\xi \frac{N(0)}{\xi}. \quad (1.3.23)$$

$N(0)$ is the DOS per spin of the conduction electron at the Fermi level. Beta function is given by,

$$\boxed{\beta = \frac{\delta J_K}{\delta \log(D)} = -N(0)J_K^2}. \quad (1.3.24)$$

Renormalization group flow diagram is plotted in Fig. 1.7. For antiferromagnetic case, $J_K > 0$, Kondo coupling grows as we move toward lower and lower energy or temperature. It becomes an attractive fixed point. Whereas for ferromagnetic case, $J_K < 0$, Kondo coupling flow towards zero along the line $J_K = [J_K]_z = [J_K]_{\pm}$, therefore it is a repulsive fixed point.

1.3.4 Numerical renormalization group

The discussion on the poor man's RG above emphasizes that, at low-temperature total self-energy has a logarithmic divergence. If such a divergence is present, it should be observed in experimental data such as resistivity, specific heat, quasi-particle lifetime etc. However, no such anomalies were found in experiments in the HF systems. By formulating the Numerical renormalization group (NRG)

technique, K. G. Wilson [33] solved this problem, hence giving the ground state of the Kondo system, which is a singlet between impurity electron and conduction electron. Later, using NRG, Krishna-murthy *et al* [34] solve the Anderson impurity model and obtain different fixed points of RG.

The steps of NRG are following [35],

1. The hybridization function, Δ_h [see Eq.(1.3.6)], is discretized into a set of logarithmic energy interval (Λ), $\epsilon_n = \pm\Lambda^{-n}$, for $n = 0, 1, 2, \dots$ and width of the interval $d_n = \Lambda^{-n}(1 - \Lambda^{-1})$. In Fig. 1.8 we use a constant Δ_h [which Wilson [33] used to solve Kondo model], however, for general non-constant Δ_h , the same procedure was used in Ref. [35].
2. The continuous spectra of the c -electrons are replaced by a discrete set of plane wave states at the energy interval.
3. The discretized model is mapped into a semi-infinite chain, with the impurity at the origin. [see Fig. 1.9]
4. Diagonalize the chain Hamiltonian by iteratively as a function of chain sites (N) will give total energy E_N .
5. Analysis of E_N provide relevant, marginal, or irreverent fixed points.

Steps 1-3 : We replace the momentum summation in Eq. (1.3.3) and Eq.(1.3.4) by an energy integral (ϵ), with $D = 1$,

$$H = H_f + \sum_{\sigma} \int_{-1}^1 d\epsilon E_{\epsilon} c_{\epsilon\sigma}^{\dagger} c_{\epsilon\sigma} + \sum_{\sigma} \int_{-1}^1 d\epsilon v_{\epsilon} c_{\epsilon\sigma}^{\dagger} f_{\sigma} + \text{h.c.} \quad (1.3.25)$$

H_f is given in Eq.(1.3.2). E_{ϵ} is the energy of the conduction electrons and v_{ϵ} is the hybridization. Anticommutation relation is given by, $[c_{\epsilon\sigma}, c_{\epsilon'\sigma'}^{\dagger}]_{+} = \delta(\epsilon - \epsilon')\delta_{\sigma\sigma'}$. The electron field operators are expanded in the plane wave basis at each discrete energy state,

$$c_{\epsilon\sigma} = \frac{1}{d_n} \sum_n \left(\alpha_{n\sigma} \psi_{np}^{+} + \psi_{np}^{-} \beta_{n\sigma} \right). \quad (1.3.26)$$

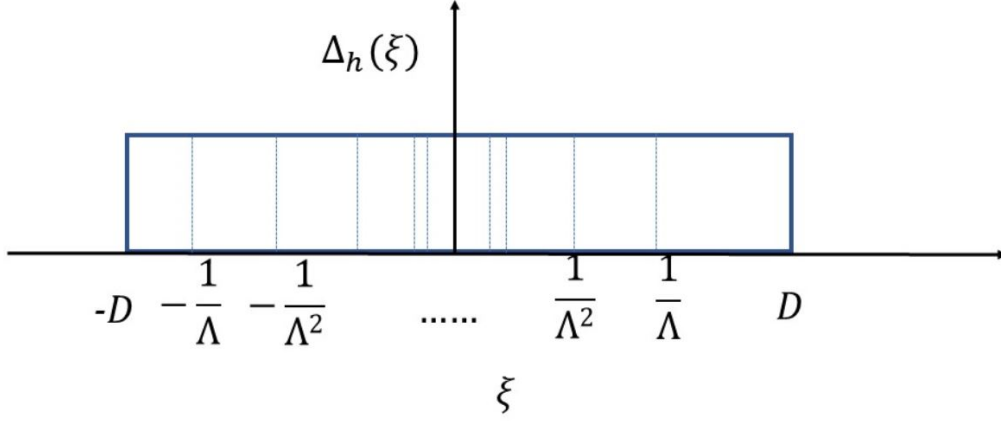


Figure 1.8: Logarithmic discretization used in step 1 in NRG. $D = 1$ in the calculations.

Where $\alpha_{n\sigma}$ and $\beta_{n\sigma}$ are fermionic annihilation operators, ψ_{np}^\pm is given by,

$$\psi_{np}^\pm(\epsilon) = \begin{cases} \frac{1}{\sqrt{d_n}} e^{i\frac{2\pi p\epsilon}{d_n}}, & \text{for } \epsilon_{n+1} < \pm\epsilon < \epsilon_n, \\ 0, & \text{otherwise.} \end{cases}$$

For a constant v_ϵ , using the integral in Eq.(1.3.25),

$$\frac{1}{d_n} \int_{-1}^1 d\epsilon \psi_{np}^+ f_\sigma = \frac{1}{d_n} \sum_{np} \int_{\xi_{n+1}}^{\xi_n} d\epsilon \psi_{np}^+ f_\sigma = \sum_{np} \delta_{p0} f_\sigma, \quad (1.3.27)$$

i.e., only $p = 0$ mode survives. We get similar result for ψ_{np}^- , $\frac{1}{d_n} \int_{-1}^1 d\epsilon \psi_{np}^- f_\sigma = \sum_{np} \delta_{p0} f_\sigma$. Substituting, Eq. (1.3.26) into Eq. (1.3.25) we obtain,

$$H_c = \sum_{n,\sigma} \left[E_n^+ \alpha_{n\sigma}^\dagger \alpha_{n\sigma} + E_n^- \beta_{n\sigma}^\dagger \beta_{n\sigma} \right], \quad (1.3.28)$$

$$H_{cf} = \frac{1}{\sqrt{\pi}} \sum_{n,\sigma} f_\sigma^\dagger \left(a_n \alpha_{n\sigma} + b_n \beta_{n\sigma} \right) + h.c., \quad (1.3.29)$$

where,

$$\begin{aligned} E_n^+ &= \frac{1}{a_n} \int_{\epsilon_{n+1}}^{\epsilon_n} d\epsilon \epsilon \Delta_h, & E_n^- &= \frac{1}{b_n} \int_{-\epsilon_n}^{-\epsilon_{n+1}} d\epsilon \xi \Delta_h, \\ a_n &= \int_{\xi_{n+1}}^{\xi_n} d\xi \Delta_h, & b_n &= \int_{-\xi_n}^{-\xi_{n+1}} d\xi \Delta_h. \end{aligned} \quad (1.3.30)$$

The third step of NRG is to transform the AIM into a model of semi-infinite chain, where the impurity electron is at the one end of the chain (origin), and hybridizes with the conduction electron [see Fig. 1.9]. We define a new conduction electron operator at $n = 0$, $\gamma_{0\sigma} = \frac{1}{\sqrt{\pi}} \sum_n (a_n \alpha_{n\sigma} + b_n \beta_{n\sigma})$.

$$H_{cf} = \sum_{\sigma} f_{\sigma}^{\dagger} \gamma_{0\sigma} + h.c. \quad (1.3.31)$$

Other fermionic operators ($\gamma_{n\sigma}$), for $n > 0$ are constructed from $\gamma_{0\sigma}$, $\alpha_{n\sigma}$ and $\beta_{n\sigma}$ by tridiagonalization,

$$\gamma_{n\sigma} = \sum_m \left[U_{mn} \alpha_{m\sigma} + V_{mn} \beta_{m\sigma} \right]. \quad (1.3.32)$$

U_{mn} and V_{mn} are the coefficients of the orthogonal matrices. $\gamma_{n\sigma}$ is the fermionic operator. After substituting $\alpha_{n\sigma}$ and $\beta_{n\sigma}$ from Eq. (1.3.32) in Eq.(1.3.28) and Eq.(1.3.29) we obtain,

$$H_c = \sum_{\sigma, n} \left[\mu_n \gamma_{n\sigma}^{\dagger} \gamma_{n\sigma} + t_n \gamma_{n+1\sigma}^{\dagger} \gamma_{n\sigma} + h.c. \right], \quad (1.3.33)$$

where t_n is the effective hopping parameter and μ_n is the onsite energy. The value of t_n and μ_n can be obtained by comparing Eq.(1.3.28) and Eq.(1.3.33). Wilson [33] first derived the t_n for a constant Δ_h , he found that $\mu_n = 0$ and for large n , [35] $t_n \sim \Lambda^{-n/2}$. Total Hamiltonian of AIM after the transformation becomes,

$$H = H_f + \sum_{\sigma, n} t_n \left[\gamma_{n+1\sigma}^{\dagger} \gamma_{n\sigma} + \gamma_{n\sigma}^{\dagger} \gamma_{n+1\sigma} \right] + \sum_{\sigma} \left(f_{\sigma}^{\dagger} \gamma_{0\sigma} + \gamma_{0\sigma}^{\dagger} f_{\sigma} \right). \quad (1.3.34)$$

Steps 4-5 : We need to diagonalize the NRG Hamiltonian Eq. (1.3.34). However, full diagonalization for an arbitrary number of chain sites is impossible to do.

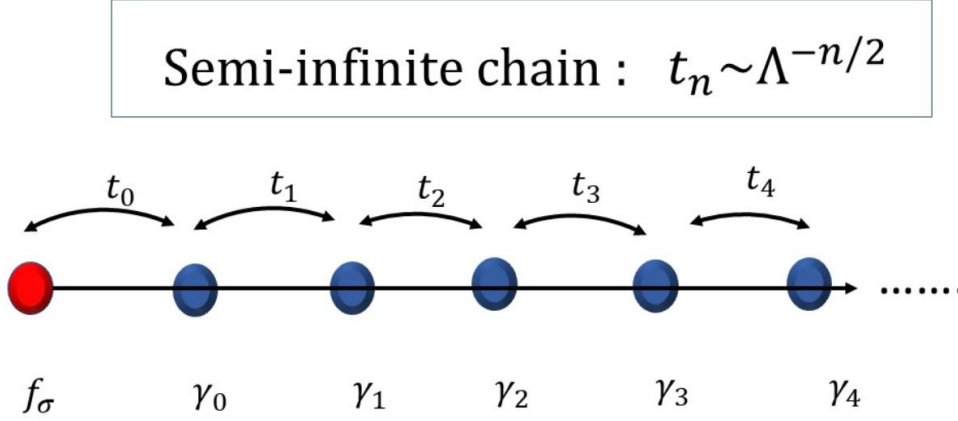


Figure 1.9: The semi-infinite chain model where the impurity site is at the origin.

Hence, it is diagonalized for a finite number of sites, say N , as $N \rightarrow \infty$ we get the complete solution of the Hamiltonian.

$$H = \lim_{N \rightarrow \infty} \Lambda^{-(N-1)/2} H_N. \quad (1.3.35)$$

Where H_N is given by,

$$H_N = \Lambda^{(N-1)/2} \left[H_f + \sum_{\sigma} \sum_{n=0}^N \left(t_n \gamma_{n+1\sigma}^\dagger \gamma_{n\sigma} + f_\sigma^\dagger \gamma_{0\sigma} + h.c. \right) \right]. \quad (1.3.36)$$

RG transformation is defined by the recursion relation,

$$H_{N+1} = \sqrt{\Lambda} H_N + \Lambda^{N/2} \sum_{\sigma} t_N \gamma_{N+1\sigma}^\dagger \gamma_{N\sigma} + h.c. \quad (1.3.37)$$

The RG flow diagrams are obtained by the diagonalization of the Hamiltonian Eq. (1.3.36), with eigenvalues and eigenfunction are E_N , ψ_N respectively. So far, the procedure is exact. The approximation used in NRG is to truncate the size of the Hilbert space. Since adding electrons site to the N -th site, the size of the Hilbert space increases exponentially. If N_s is the dimension of H_N then, N_s number of eigenstates are chosen for H_{N+1} . The eigenstates of H_{N+1} , is constructed from the H_N , $|\psi\rangle_{N+1} = \gamma_{N+1,\sigma}^\dagger |\psi\rangle_N$. The states are characterized by total charge

(Q) and spin (S_z). NRG solution of the AIM first done by Krishna-murthy *et al* [34], they found that three different fixed points,

1. Unstable fixed point for $N < 10$. This is called free orbital fixed point, $U = 0$.
2. $11 < N < 60$, crossover from free orbital to local moment fixed point.
3. Stable fixed point $N > 60$, local moment are coupled with the conduction electron via J_K .

We conclude the discussion on NRG with the remark that this method is not limited to only AIM, other quantum impurity systems such as quantum dot, quantum dissipative system, Mott transitions can be analyzed within the framework of NRG [35].

1.3.5 Slave-Boson method

Different techniques were developed over the last forty years, such as auxiliary field (particle) by S. E. Barnes [36], Gutzwiller projection [37, 38], t - J model [39, 40, 41], Hubbard–Stratonovich transformation [42, 43], Holstein–Primakoff transformation [44], Abrikosov fermions [18, 32], etc. Slave boson method [45] is such a method developed by S. E. Barnes [36] and P. Coleman [46] implemented it for the HF systems at the strong coupling limit..

The Hilbert space of f -state for large Coulomb repulsion consists of two degenerate singly occupied states $f_{\uparrow/\downarrow}^1$, one doubly occupied state f^2 , and an unoccupied or empty state f^0 . These states are often called spinon (fermion : \bar{f}_σ), holon (boson: e) and doublon (boson: d). In the strong correlation limit, Coulomb interaction (U) is much greater than D and the doubly occupied states lie at higher energy than other three states. So, it is desirable to find a ground state by systematically eliminating the high energy states. The f -electron state is hence expanded in the parton formalism as,

$$f_\sigma = e^\dagger \bar{f}_\sigma + \sigma \bar{f}_\sigma^\dagger d, \quad (1.3.38)$$

where, \bar{f}_σ represents fermionic states and e, d are bosonic states. If we use Eq. (1.3.38) and evaluate the operator products, $[f_\sigma f_{\sigma'}^\dagger + f_{\sigma'}^\dagger f_\sigma]$, we obtain

$$\left[f_\sigma, f_{\sigma'}^\dagger \right]_+ = \delta_{\sigma, \sigma'} (e^\dagger e + d^\dagger d + \sum_\sigma \bar{f}_\sigma^\dagger \bar{f}_\sigma). \quad (1.3.39)$$

Hence, the necessary condition to maintain fermionic nature of f -electrons is $e^\dagger e + d^\dagger d + \sum_\sigma \bar{f}_\sigma^\dagger \bar{f}_\sigma = 1$. Let, $n_{\bar{f}}, n_e, n_d$ are the number operators for \bar{f} electron, holon and doublon respectively. Conservation of atomistic f -electron number at every lattice sites gives, $n_f = n_{\bar{f}} + n_e + n_d = 1$. We will use the Bernes representation [36, 45], together with the doublon occupancy zero, $n_d = 0$, because of strong Coulomb repulsion. The constraint condition on the Fock space thus becomes,

$$Q = n_{\bar{f}} + n_e = 1. \quad (1.3.40)$$

Using Eq. (1.3.40) as constraint with Lagrange multiplier ω_e , we obtain the Hamiltonian of periodic Anderson model (PAM),

$$H = \underbrace{\sum_{\mathbf{k}, \sigma} \xi_{\mathbf{k}} c_{\mathbf{k}\sigma}^\dagger c_{\mathbf{k}\sigma}}_{\text{Conduction band}} + \underbrace{\bar{\xi}_f \sum_{\sigma} \bar{f}_\sigma^\dagger \bar{f}_\sigma}_{\text{Impurity orbital}} + \sum_{\mathbf{k}, \sigma} \left[\underbrace{v_{\mathbf{k}} c_{\mathbf{k}\sigma}^\dagger e^\dagger \bar{f}_\sigma}_{\text{Holon emission}} + \underbrace{v_{\mathbf{k}}^\dagger \bar{f}_\sigma^\dagger e c_{\mathbf{k}\sigma}}_{\text{Holon absorption}} \right] + \underbrace{\omega_e (e^\dagger e - 1)}_{\text{constraint}}. \quad (1.3.41)$$

Where $\bar{\xi}_f = \xi_f + \omega_e$. Eq. (1.3.41) cannot be solved exactly, hence we use a mean-field approximation about bosonic field, $e_0 = \langle e \rangle$. Hamiltonian Eq. (1.3.41) becomes,

$$H = \sum_{\mathbf{k}, \sigma} \xi_{\mathbf{k}} c_{\mathbf{k}\sigma}^\dagger c_{\mathbf{k}\sigma} + \bar{\xi}_f \sum_{\sigma} \bar{f}_\sigma^\dagger \bar{f}_\sigma + e_0 \sum_{\mathbf{k}, \sigma} v_{\mathbf{k}} c_{\mathbf{k}\sigma}^\dagger \bar{f}_\sigma + \omega_e (e_0^2 - 1) + h.c. \quad (1.3.42)$$

The action functional [18, 45, 47] of the Hamiltonian Eq. (1.3.42) is,

$$S = S_c + S_{\bar{f}} + S_v, \quad (1.3.43)$$

where,

$$\mathcal{S}_c = \int_0^\beta d\tau \sum_{\mathbf{k},\sigma} \tilde{c}_{\mathbf{k}\sigma}(\tau) (\partial_\tau + \xi_{\mathbf{k}}) c_{\mathbf{k}\sigma}(\tau), \quad (1.3.44)$$

$$\mathcal{S}_{\bar{f}} = \int_0^\beta d\tau \sum_{\sigma} \tilde{f}_{\sigma}(\tau) (\partial_\tau + \bar{\xi}_f) \bar{f}_{\sigma}(\tau), \quad (1.3.45)$$

$$\mathcal{S}_v = e_0 \int_0^\beta d\tau \sum_{\mathbf{k},\sigma} (v_{\mathbf{k}} \tilde{c}_{\mathbf{k}\sigma}(\tau) \bar{f}_{\sigma}(\tau) + \text{h.c.}). \quad (1.3.46)$$

Here \tilde{e}, e are bosonic coherent states and $\tilde{f}, \bar{f}, \tilde{c}, c$ are Grassmann variables for singly occupied f -states, and conduction electrons respectively ('tilde' means conjugation). τ is imaginary time axis. Thermodynamic properties of the system can be calculated from the partition function $\mathcal{Z} = \text{Tr} e^{-\mathcal{S}}$,

$$\begin{aligned} \mathcal{Z} &= \mathcal{Z}_0 \int \mathcal{D}[\tilde{c}, c] \mathcal{D}[\tilde{f}, \bar{f}] e^{-\mathcal{S}_c - \mathcal{S}_{\bar{f}} - \mathcal{S}_v}, \\ &= \mathcal{Z}_0 \int \mathcal{D}[\tilde{f}, \bar{f}] e^{-\mathcal{S}_{\bar{f}}} \left[\int \mathcal{D}[\tilde{c}, c] e^{-\mathcal{S}_c - \mathcal{S}_v} \right], \\ &= \mathcal{Z}_0 \prod_{\mathbf{k}, k_n} [\beta(-ik_n + \xi_{\mathbf{k}})] \int \mathcal{D}[\tilde{f}, \bar{f}] e^{-\mathcal{S}_{eff}[\tilde{f}, \bar{f}]}, \end{aligned} \quad (1.3.47)$$

Where, $\mathcal{Z}_0 = e^{-\beta\omega_e(e_0^2-1)} = e^{-\beta\mathcal{F}_0}$, is the free energy contribution from the bosonic saddle point. In the last line of Eq. (1.3.47), we Fourier transform the conduction electron in Matsubara frequency using, $c_{\mathbf{k}\sigma}(\tau) = \frac{1}{\sqrt{\beta}} \sum_n c_{\mathbf{k}\sigma}(ik_n) \exp(-ik_n\tau)$. [47]. Then we integrate out the conduction electron states.

The effective action is given by,

$$\mathcal{S}_{eff}[\tilde{f}, \bar{f}] = \int d\tau \sum_{\sigma} \tilde{f}_{\sigma}(\tau) (\partial_\tau + \bar{\xi}_f - \Sigma_f(\tau)) \bar{f}_{\sigma}(\tau). \quad (1.3.48)$$

Where, $\Sigma_f(\tau) = \sum_{\mathbf{k}'} \frac{\tilde{v}_{\mathbf{k}'}^2}{\partial_\tau + \xi_{\mathbf{k}'}}$ is the self-energy of the f -electron [18] and $\tilde{v}_{\mathbf{k}} = v_{\mathbf{k}} e_0$ is renormalized hybridization energy [45]. We then Fourier transform the fermion fields to the Matsubara space, $\bar{f}_{\sigma}(\tau) = \frac{1}{\sqrt{\beta}} \sum_n \bar{f}_{\sigma}(ip_n) \exp(-ip_n\tau)$.

Since Eq. (1.3.48) is in a quadratic form, we can easily do the Grassmann

integral. The result is

$$\mathcal{Z} = \mathcal{Z}_0 \left[\beta \prod_{\mathbf{k}, k_n} (ik_n - \xi_{\mathbf{k}}) \right] \left[\beta \prod_{p_n} \left(ip_n - \bar{\xi}_f - \sum_{\mathbf{k}'} \frac{\tilde{v}_{\mathbf{k}'}^2}{ip_n - \xi_{\mathbf{k}'}} \right) \right]. \quad (1.3.49)$$

The free energy is given by

$$\begin{aligned} \mathcal{F} &= -\frac{1}{\beta} \ln(\mathcal{Z}), \\ &= \mathcal{F}_0 - \frac{1}{\beta} \sum_{\mathbf{k}, k_n} \ln \left[\beta (ik_n - \xi_{\mathbf{k}}) \right] - \sum_{p_n} \frac{1}{\beta} \ln \left[\beta \left(ip_n - \bar{\xi}_f - \sum_{\mathbf{k}'} \frac{\tilde{v}_{\mathbf{k}'}^2}{ip_n - \xi_{\mathbf{k}'}} \right) \right], \\ &= \mathcal{F}_0 + \mathcal{F}_c + \mathcal{F}_f, \end{aligned} \quad (1.3.50)$$

where $\mathcal{F}_c = -\frac{1}{\beta} \sum_{\mathbf{k}, k_n} \ln \left[\beta (ik_n - \xi_{\mathbf{k}}) \right] = -\frac{1}{\beta} \sum_{\mathbf{k}} \ln [1 + e^{-\beta \xi_{\mathbf{k}}}]$ is the free energy of the conduction electron.

$$\begin{aligned} \mathcal{F}_f &= -\sum_{k_n} \frac{1}{\beta} \ln \left[\beta \left(ik_n - \bar{\xi}_f - \sum_{\mathbf{k}} \frac{\tilde{v}_{\mathbf{k}}^2}{ik_n - \xi_{\mathbf{k}}} \right) \right], \\ &= -\frac{2}{\pi \beta} \int d\omega \ln(1 + e^{-\beta \omega}) \operatorname{Im} \left(\frac{\partial}{\partial \omega} \ln(\mathcal{G}_f(\omega + i\delta)) \right). \end{aligned} \quad (1.3.51)$$

In the second line we use the Matsubara summation over the fermion frequency k_n [47] and a factor 2 comes from two spin of conduction electrons (up/down spin). Using integration by parts we have,

$$\begin{aligned} \mathcal{F} - \mathcal{F}_c &= \mathcal{F}_0 + \frac{2}{\pi} \int d\omega f(\omega) \operatorname{Im} \left(\ln(\mathcal{G}_f(\omega + i\delta)) \right), \\ &= (\bar{\xi}_f - \xi_f)(e_0^2 - 1) + \frac{2}{\pi} \int d\omega f(\omega) \tan^{-1} \left[\frac{\tilde{\Delta}_h}{\omega - \bar{\xi}_f} \right]. \end{aligned} \quad (1.3.52)$$

In the last line we substituted the resonance width [see Eq. (1.3.6)], [18] $\tilde{\Delta}_h(\xi) = \sum_{\mathbf{k}} \pi \tilde{v}_{\mathbf{k}}^2 N(\epsilon_{\mathbf{k}} - \xi)$. $f(\omega) = \frac{1}{e^{\beta \omega} + 1}$ is the Fermi distribution function. [See 1] ¹

¹ $z = x + iy = r e^{i\theta}$, $\operatorname{Im}[\ln(z)] = \tan^{-1}(y/x)$

From Eq. (1.3.51) we have the Green's function of f -electron,

$$\mathcal{G}_f(i\omega_n) = \left[i\omega_n - \bar{\xi}_f - \Sigma_f(i\omega_n) \right]^{-1}. \quad (1.3.53)$$

Where self-energy is given by,

$$\Sigma_f(i\omega_n) = \sum_{\mathbf{k}} \frac{\tilde{v}_{\mathbf{k}}^2}{i\omega_n - \xi_{\mathbf{k}}}, \quad (1.3.54)$$

After performing analytic continuation in the real axis, $i\omega_n$ by $\omega + i\eta$, and replacing momentum summation by integration over continuum of energy ξ , [18]

$$\begin{aligned} \Sigma_f(\omega + i\eta) &= N(0)\tilde{v}^2 \int_{-D}^D \frac{1}{\omega - \xi + i\eta}, \\ &= \frac{\tilde{\Delta}_h}{\pi} \ln \left[\frac{\omega + D + i\eta}{\omega - D + i\eta} \right], \\ &= \frac{\tilde{\Delta}_h}{\pi} \ln \left| \frac{\omega + D}{\omega - D} \right| - i\tilde{\Delta}_h. \end{aligned} \quad (1.3.55)$$

In the second line of Eq. (1.3.55) we assume \tilde{v}_k is momentum independent and $N(0)$ is the density of state at the Fermi level, $\tilde{\Delta}_h = \pi N(0)\tilde{v}^2$. Real part of the self-energy is at the order of $\frac{\omega}{D}$, hence we can neglect it. Therefore, we obtain,

$$\Sigma_f(\omega + i\eta) = -i\tilde{\Delta}_h. \quad (1.3.56)$$

Using self-energy in Eq. (1.3.53),

$$\mathcal{G}_f^{-1}(\omega + i\eta) = \omega - \bar{\xi}_f + i\tilde{\Delta}_h + i\eta. \quad (1.3.57)$$

So, it is evident that mean-field solution of $U \rightarrow \infty$ model normalises the parameters of non-interacting model $U = 0$, $\tilde{\Delta}_h = e_0^2 \Delta_h$ [18]. At $T = 0$, Eq. (1.3.52) can

be solved exactly, $f(\omega) = \Theta(-\omega)$ is the step function.

$$\begin{aligned} \mathcal{F} - \mathcal{F}_c \Big|_{T=0} &= \mathcal{E}[\tilde{\Delta}_h, \bar{\xi}_f], \\ &= (\bar{\xi}_f - \xi_f) \left(\frac{\tilde{\Delta}_h}{\Delta_h} - 1 \right) + \frac{2\tilde{\Delta}_h}{2\pi} \ln \left[\frac{\tilde{\Delta}_h^2 + \bar{\xi}_f^2}{D^2} \right] + \frac{2\bar{\xi}_f}{\pi} \tan^{-1} \left(\frac{\tilde{\Delta}_h}{\bar{\xi}_f} \right). \end{aligned} \quad (1.3.58)$$

At the saddle point, the ground state energy Eq. (1.3.58) is minimized w.r.t the re-normalised parameters, i.e. $\tilde{\Delta}_h$, $\bar{\xi}_f$. From the minimizing $\frac{\partial \mathcal{E}}{\partial \tilde{\Delta}_h} = 0$, we obtain,

$$\frac{(\bar{\xi}_f - \xi_f)}{\Delta_h} + \frac{1}{\pi} \ln \left[\frac{\tilde{\Delta}_h^2 + \bar{\xi}_f^2}{D^2} \right] \approx 0, \quad (1.3.59)$$

$$\bar{\xi}_f = \xi_f - \frac{2\Delta_h}{\pi} \ln \left[\frac{\sqrt{\tilde{\Delta}_h^2 + \bar{\xi}_f^2}}{D} \right]. \quad (1.3.60)$$

Second minimisation condition gives, (2) $\frac{\partial \mathcal{E}}{\partial \bar{\xi}_f} = 0$,

$$\left(\frac{\tilde{\Delta}_h}{\Delta_h} - 1 \right) + \frac{2}{\pi} \tan^{-1} \left(\frac{\tilde{\Delta}_h}{\bar{\xi}_f} \right) = 0, \quad (1.3.61)$$

$$\tilde{\Delta}_h = \Delta_h - \frac{2\Delta_h}{\pi} \tan^{-1} \left(\frac{\tilde{\Delta}_h}{\bar{\xi}_f} \right). \quad (1.3.62)$$

From the constraint condition Eq. (1.3.40) we obtain,

$$\begin{aligned} n_{\bar{f}} &= 1 - n_e, \\ &= 1 - e_0^2, \\ &= 1 - \frac{\tilde{\Delta}_h}{\Delta_h}, \\ &= \frac{2}{\pi} \tan^{-1} \left(\frac{\tilde{\Delta}_h}{\bar{\xi}_f} \right). \end{aligned} \quad (1.3.63)$$

$\tilde{\Delta}_h \ll \bar{\xi}_f$, $\tan^{-1} \left(\frac{\tilde{\Delta}_h}{\bar{\xi}_f} \right) \rightarrow \frac{\pi}{2}$ and $n_{\bar{f}} = 1$; which implies that the local moment formation at sufficiently high $\bar{\xi}_f$, since average occupation of f -electron, $n_f =$

$n_{\bar{f}} = 1$ ($n_e = 0$), otherwise $n_{\bar{f}} < 1$ ($n_e \neq 0$). At low temperature, this average local moment density at every site will be quenched by the surrounding conduction electrons. When $\bar{\xi}_f$ is near the Fermi level local moments will form a resonance with conduction electrons via the hybridization interaction. The width of the resonance is given by the coherence temperature (T_K). From Eq. (1.3.59) we obtain,

$$0 = -|\xi_f| - \frac{2\Delta_h}{\pi} \ln \left[\frac{T_K}{D} \right], \quad (1.3.64)$$

$$\boxed{T_K = D e^{-\frac{\pi|\xi_f|}{2\Delta_h}} = D e^{-\frac{1}{2N(0)J_K}}}. \quad (1.3.65)$$

We discussed different theoretical methods to solve the PAM in the strong coupling limit. The infra-red divergence of the Kondo model at low temperature was solved by two methods namely, (a) NRG developed by Wilson [33], then subsequently solved for Anderson model by Krishna-murthy *et al.* [34] and (b) Slave-boson method developed by S. E. Barnes [36] and P. Coleman [46]. The Slave-boson method was generalized to multi-band Hubbard model and spin rotational invariant form by Kotliar and Ruckenstein [45]. We discussed the solution of PAM using saddle point approximation about bosonic fields. In the later chapter, we will discuss fluctuation about the mean-fields, which will give rise to superconductivity.

1.4 transition-metal oxides superconductors

Soon after the discovery of superconductivity in HF metals, high-temperature superconductivity was discovered in Lanthanum–Barium Copper Oxide compounds [49]. Afterwards many families of copper oxides superconductors were discovered with high temperature are obtained in $\text{YBa}_2\text{Cu}_3\text{O}_{6+x}$ (YBCO) ($T_c = 93$ K) [50] and $\text{HgBa}_2\text{CuO}_{4+x}$ ($T_c = 133$ K) [51, 52]. This family is called cuprates. Cuprates consist of a common copper-oxide plane, with the higher number of layers scales with higher T_c , but eventually saturates the value of T_c above a few-layer [53]. YBCO compound has an additional metallic chain layer, in which a chain of CuO is missing from the CuO_4 plane layer.

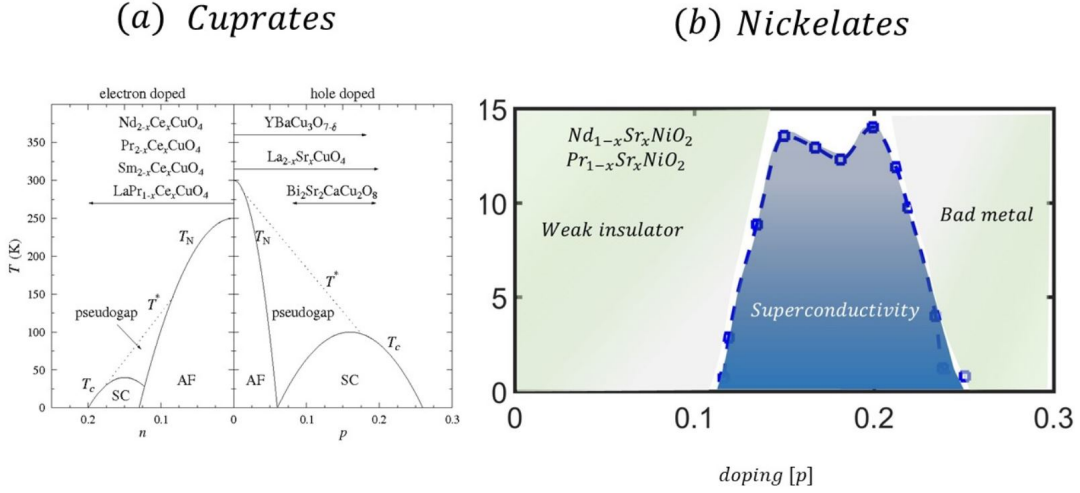


Figure 1.10: (a) Schematic phase diagram of cuprate superconductors [48]. (b) Experimental phase diagram of $(\text{Nd/Pr})_{1-x}\text{Sr}_x\text{NiO}_x$. We replot the experimental data from [58].

In the CuO_4 layer, Cu has a d^9 state, which gives a half-filled d -orbital near the Fermi level. d -orbital strongly hybridize with the ligand O-atoms surrounding the Cu-atom in the octahedral structure. An effective one band picture of strongly hybridized Cu $d_{x^2-y^2}$ and O p_x, p_y orbitals, describes the low energy physics. A one-band Hubbard model in a square lattice thus dominates the theoretical study of cuprates, as done from the weak-coupling perturbation theory to strong coupling t - J model [8, 9, 39, 40] to the intermediate coupling local-itinerant dual picture [1]. Such a model also thus become an easy platform to study via dynamical mean-field theory (DMFT) [54, 55, 56] and quantum Monte Carlo (QMC)[4] method. These models give the Mott insulating antiferromagnetic (AFM) ground state at half filling and superconductivity at finite doping.

The above story changes if we consider a three-band model with Cu $d_{x^2-y^2}$ and O p_x, p_y orbitals. It is then found that in the strong coupling limit, the lower Hubbard band of the Cu d orbital is pushed below the O p band, giving a charge transfer insulator [see Fig. 1.13]. The three-band picture also reveals that a nearly flat, singlet state of Cu d spin-1/2 and O p spin-1/2 arises inside the insulating gap, which is called Zhang-Rice singlet [see Fig. 1.11] [57].

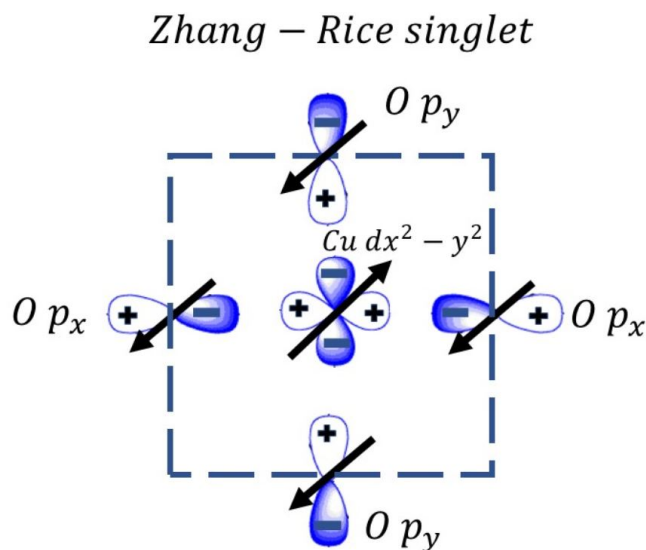
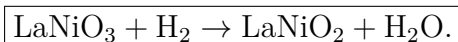


Figure 1.11: Schematic representation of the Zhang-Rice singlet in cuprate superconductor.

1.5 Infinite-layer Nickelates

The discovery of high-temperature superconductivity in cuprates [41] consisting of two-dimensional (2D) CuO_2 planes has prompted the search for other transition-metal oxide compounds. This raised the interest in the existence of nickelate compounds with a two-dimensional NiO_2 plane as the common structural element, in which Ni^{1+} ions have the same electronic configuration of d^9 , as in the Cu^{2+} ion in CuO_2 plane.²

NdNiO_3 has a perovskite structure, with Ni valency +3 [59]. With low temperature reduction under hydrogen NdNiO_3 becomes NdNiO_2 . This hydrogen reduction removes the apical oxygen, and the Ni valency becomes +1. The synthesis reaction of LaNiO_2 from LaNiO_3 was obtained as [60]



²We will denote compounds with NiO_2 plane as infinite-layer nickelates throughout the thesis.

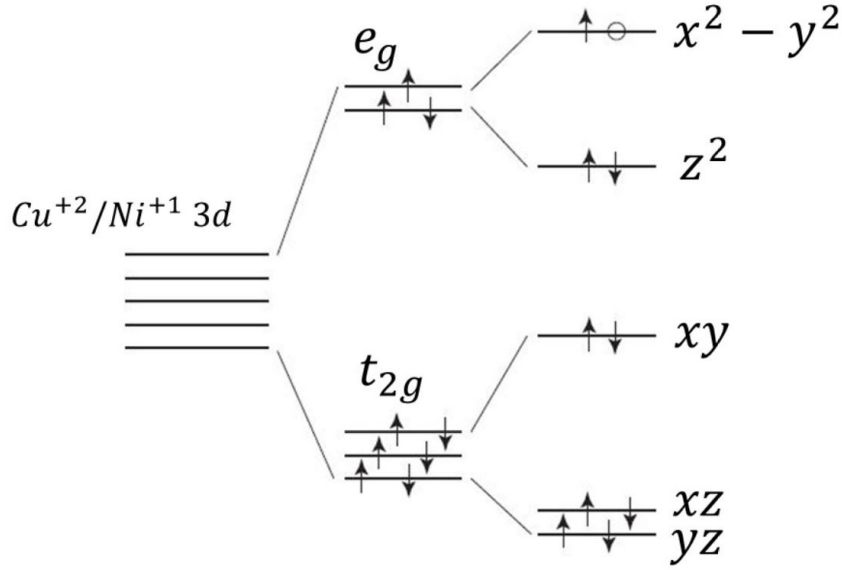


Figure 1.12: Splitting of d orbitals of Cu^{+2} and Ni^{+1} in tetragonal environment.

The successful synthesis of the $Ni 3d^9$ configuration has prompted many researchers to investigate this compound as an analogy of cuprates. However, subsequent density functional theory (DFT) studies reveal many characteristic differences between cuprates and infinite-layer nickelates, as compared in Table 1.1. Initially, it was thought [61] that the undoped NiO_2 compound would be a magnetic insulator analogous to cuprates. However, it was observed that NiO_2 is a bad metal. The electronic configuration Ni is, $[Ar] 3d^9 4s^1$; where the valency of Ni in NiO_2 is Ni^{+1} , which is identical to the Cu^{+2} ions in CuO_4 . $NdNiO_2$ arranged in a tetragonal structure. The electron arrangement of Ni^{+1} is shown in Fig. 1.12, where the $3d$ orbital has nine electron and outermost $d_{x^2-y^2}$ orbital contains one hole.

The similarity of the $Ni 3d^9$ ion with $Cu 3d^9$ prompted theoretical studies by Anisimov *et al.*, in 1999 [61], exhibiting some band structure similarity. But soon, it was realized by Lee and Pickett, in 2004 [62] that even at the band structure level, there are crucial differences between infinite-layer nickelates and cuprates, including reduction of $3d - 2p$ hybridization in the infinite-layer nickelates compared to cuprates. The same authors also showed that there are additional Nd

Table 1.1: Comparison of relevant properties of cuprates and nickelates.

	Cuprates	Nickelates
Structure	Octahedral with apical oxygen present.	Infinite-layer with apical oxygen removed.
Half-filling	Mott/antiferromagnetic insulator.	Weak insulator/bad metal.
Zhang-Rice singlet	Zhang-Rice singlet.	No Zhang-Rice singlet.
Charge transfer gap	Charge transfer gap.	No charge transfer gap.
Effective model	One-band effective model.	Two-orbital model (Ni $d_{x^2-y^2}$ and Nd d_{z^2} orbital).
Superconducting gap symmetry	$d_{x^2-y^2}$ pairing (with signature/ predictions of nodeless s , p , f)-wave pairing at special tuning.	Prediction of two-gap scenario ($d_{x^2-y^2}$ and d_{z^2}).

$3d_{z^2}$ bands present at the Fermi level, making it a multi-band compound. Therefore, the physics obtained at the 3-band picture in cuprates are different in the infinite-layer nickelates.

It turns out that infinite-layer nickelates do not have Zhang-Rice singlet state like cuprates. It is also not a charge transfer insulator. In fact, at half-filling, the material is not a Mott insulator, but a weak insulator or bad metal. Moreover, it is found experimentally that Ni $3d_{x^2-y^2}$ orbital is more correlated than Nd $3d_{z^2}$ orbital. There is a hybridization between the two orbitals which produces an emergent Kondo physics in this compound [63].

Recently, infinite-layer NdNiO₂ was prepared by Shengwei Zeng *et.al.* [58] by the mechanism (soft-chemistry topotactic reduction) developed at SLAC National Accelerator Laboratory [59]. This material was then hole doped with chemical substitution using Sr on the Nd site. Then, in the doping range 0.12 and 0.235 [64, 58], superconductivity appears, and show a dome (or a split dome) feature in the T_c value with optimal T_c about 15 K around doping $x \sim 0.2$. Subsequently, LaNiO₂ and PrNiO₂ are also synthesized, and PrNiO₂ is found to be superconducting with

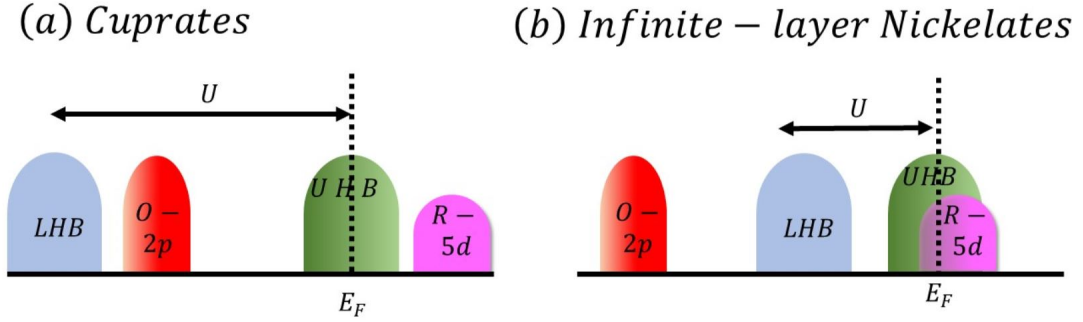


Figure 1.13: Comparison of relevant electronic orbitals near Fermi level with U , of cuprates and nickelates.

a similar dome [65], while LaNiO_2 shows superconductivity at low temperature [66]. The electronic structure properties of these compounds are very similar, with NdNiO_2 and PrNiO_2 being almost identical, while LaNiO_2 has a La-Ni hybridized band being pushed down, rendering a small FS pocket than in the other two compounds. We investigate all three compounds to understand their electronic properties and differences. Next, we deduce a low energy two orbital model with the Wannier orbital method. We find that superconductivity is orbital selective, being a two dimensional $d_{x^2-y^2}$, for Ni d orbital and a three dimensional d_{z^2} , for Nd axial orbital.

1.6 Spin-fluctuation theory

An arbitrary amount of small attraction between electrons in a metal can cause bound paired states of two electrons. This bound state is known as a Cooper pair [67]. BCS [6] later consider a many-body ground state, in which many such Cooper pairs are formed. This pair formation leads to opening a gap in the continuous spectra of single-particle states at the FS.

The superconducting gap function is,

$$\begin{aligned} \Delta_{\mathbf{k}} &= - \sum_{\mathbf{k}'} V_{\mathbf{k}\mathbf{k}'} \langle c_{-\mathbf{k}'\downarrow} c_{\mathbf{k}'\uparrow} \rangle, \\ &= - \sum_{\mathbf{k}'} V_{\mathbf{k}\mathbf{k}'} \frac{\Delta_{\mathbf{k}'}}{2E_{\mathbf{k}'}} \tanh(\beta E_{\mathbf{k}'}/2), \end{aligned} \quad (1.6.1)$$

where, $E_{\mathbf{k}'} = \sqrt{\xi_{\mathbf{k}'}^2 + \Delta_{\mathbf{k}'}^2}$, and $V_{\mathbf{k}\mathbf{k}'}$ is interaction energy between Cooper pairs at $(\mathbf{k} \uparrow, -\mathbf{k} \downarrow)$ and $(\mathbf{k}' \uparrow, -\mathbf{k}' \downarrow)$. $\xi_{\mathbf{k}}$ is the single particle continuous spectra ($\epsilon_{\mathbf{k}}$) compared to Fermi energy (E_F), $\xi_{\mathbf{k}} = \epsilon_{\mathbf{k}} - E_F$. $E_{\mathbf{k}}$ denotes that, in the excitation spectra of metal, there must be a minimum energy gap. $E_{\mathbf{k}}$ is known as the quasi-particle (*Bogoliubons* [68]) dispersion of the metal. Thus superconducting quasi-particle behaves as if it is an insulator. The BCS gap equation Eq. (1.6.1) has two possible solutions,

1. **Attractive potential** ($V_{\mathbf{k}\mathbf{k}'} < 0$): $\Delta_{\mathbf{k}}$ is positive, onsite, fully gapped. This is called conventional superconductivity.
2. **Repulsive potential** ($V_{\mathbf{k}\mathbf{k}'} > 0$): $\Delta_{\mathbf{k}}$ have to change sign (positive to negative) between \mathbf{k} and \mathbf{k}' , $\Delta_{\mathbf{k}} = -\Delta_{\mathbf{k}'}$, $\mathbf{k}' = \mathbf{k} + \mathbf{q}$. This pairing is favoured by the potential $V_{\mathbf{k}\mathbf{k}'}$, which has a peak at FS nesting vector \mathbf{q} . This is known as unconventional superconductivity.

BCS theory showed that an effective, attractive potential between electrons could emanate from the electron-phonon coupling, resulting in a fully gapped, constant sign superconducting (SC) gap (conventional *s*-wave symmetry).[6] Interestingly, discussions of unconventional superconductivity from repulsive interactions dates back to 1965.[7] It was shown that Cooper pairs could be formed in a repulsive interaction medium, provided the corresponding gap function changes sign in the momentum space[7, 9, 69, 70].

The basic understanding of the spin-fluctuation mediated pairing symmetry is that when the FS nesting is strong at a preferential wavevector, say \mathbf{Q} , it leads to a pairing symmetry which changes sign across the momentum \mathbf{k} and $\mathbf{k} + \mathbf{Q}$ on the FS.[71, 72, 73, 74, 75, 76, 77] In cuprates, the FS nesting is dominated by the spin-fluctuation wavevector $\mathbf{Q} = (\pi, \pi)$ which connects the Fermi momenta near the ‘magnetic hot-spot’ (MHS) (where the plane FS meets the magnetic zone boundary), and one obtains a $d_{x^2-y^2}$ -wave solution.[73] the pairing potential arising from the spin-fluctuation mechanism, with the many-body interaction captured within the multi-band Hubbard model.[71, 72, 73, 74, 75, 76, 77] The leading eigenvalue and its corresponding eigenfunction of the static pairing potential gives the SC coupling constant and the pairing symmetry of the system, respectively.

1.6.1 Spin-fluctuation mediated pairing in one band Hubbard model

Although we will study the multi-band Hubbard model for both YBCO cuprate and infinite-layer nickelates, we first present a one-band Hubbard model and show the derivation of the spin-fluctuation mediated pairing potential. One band Hubbard model is given by,

$$\mathcal{H} = \sum_{\mathbf{k},\sigma} \xi_{\mathbf{k}} c_{\mathbf{k},\sigma}^\dagger c_{\mathbf{k},\sigma} + \sum_{\mathbf{k},\mathbf{k}',\mathbf{q}} U c_{\mathbf{k}+\mathbf{q},\uparrow}^\dagger c_{\mathbf{k}'-\mathbf{q},\downarrow}^\dagger c_{\mathbf{k}',\downarrow} c_{\mathbf{k},\uparrow}. \quad (1.6.2)$$

We define spin operator as,

$$\mathcal{S}^+(\mathbf{q}) = \sum_{\mathbf{k}} c_{\mathbf{k},\uparrow}^\dagger c_{\mathbf{k}+\mathbf{q},\downarrow}, \quad \mathcal{S}^-(\mathbf{q}) = \sum_{\mathbf{k}} c_{\mathbf{k},\downarrow}^\dagger c_{\mathbf{k}+\mathbf{q},\uparrow}, \quad \mathcal{S}^z(\mathbf{q}) = \sum_{\mathbf{k}} [c_{\mathbf{k},\uparrow}^\dagger c_{\mathbf{k}+\mathbf{q},\uparrow} - c_{\mathbf{k},\downarrow}^\dagger c_{\mathbf{k}+\mathbf{q},\downarrow}]. \quad (1.6.3)$$

Transverse and longitudinal susceptibilities are defined as (unit $\hbar = 1$),

$$\chi^{+-}(\mathbf{q}, \tau - \tau') = \left\langle T_\tau \mathcal{S}^+(\mathbf{q}, \tau) \mathcal{S}^-(\mathbf{-q}, \tau') \right\rangle, \quad \chi^{zz}(\mathbf{q}, \tau - \tau') = \left\langle T_\tau \mathcal{S}^z(\mathbf{q}, \tau) \mathcal{S}^z(\mathbf{-q}, \tau') \right\rangle. \quad (1.6.4)$$

The Green's function of the electron is [21]

$$\mathcal{G}_{\mathbf{k},\sigma}(\tau - \tau') = - \left\langle T_\tau c_{\mathbf{k},\sigma}(\tau) c_{\mathbf{k},\sigma}^\dagger(\tau') \right\rangle. \quad (1.6.5)$$

Substituting the Green's function formula in Eq. (B.0.16), we obtain,

$$\chi^{+-}(\mathbf{q}, \tau - \tau') = - \sum_{\mathbf{k}} \mathcal{G}_{\mathbf{k}-\mathbf{q},\uparrow}(\tau' - \tau) \mathcal{G}_{\mathbf{k},\downarrow}(\tau - \tau'), \quad (1.6.6)$$

$$\chi^{zz}(\mathbf{q}, \tau - \tau') = - \sum_{\mathbf{k},\sigma=\uparrow\downarrow} \mathcal{G}_{\mathbf{k}-\mathbf{q},\sigma}(\tau' - \tau) \mathcal{G}_{\mathbf{k},\sigma}(\tau - \tau'). \quad (1.6.7)$$

By expanding the interaction term of the Hamiltonian in Eq.(1.6.2) into different

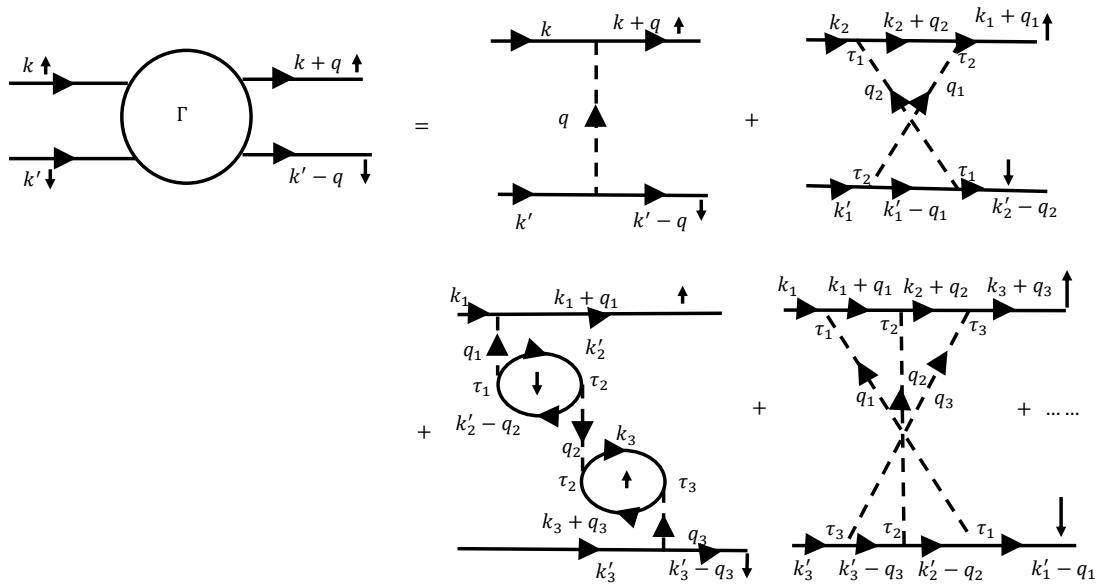


Figure 1.14: Feynman diagrams of the Hubbard model for the spin-fluctuation mediated pairing strength. The incoming and outgoing solid lines represent fermionic operators, and the dashed line represents Coulomb interactions U . The circle on the left side of the figure is the effective interaction vertex potential. To the right side of the figure, the first diagram is the bare interaction, the second and fourth diagram is the second and third-order ladder diagrams, and the third diagram is called bubble diagram.

interaction channels, [see Fig. 1.14] we obtain spin-fluctuation potential, [for detail calculation see Appendix B]

$$\begin{aligned}
\Gamma^{RPA}(\mathbf{k}', \mathbf{k}) &= U + \Gamma_{Ladder}^{RPA}(\mathbf{k}' + \mathbf{k}) + \Gamma_{Bubble}^{RPA}(\mathbf{k}' - \mathbf{k}), \\
&= U + \frac{U^2 \chi^{+-}(\mathbf{k}' + \mathbf{k})}{1 - U \chi^{+-}(\mathbf{k}' + \mathbf{k})} + \frac{U^3 (\chi^{zz}(\mathbf{k}' - \mathbf{k}))^2}{1 - U^2 (\chi^{zz}(\mathbf{k}' - \mathbf{k}))^2}, \\
&= U + \frac{U^2 \chi^{+-}(\mathbf{k}' + \mathbf{k})}{1 - U \chi^{+-}(\mathbf{k}' + \mathbf{k})} + \frac{U^2}{2} \left[\frac{\chi^{zz}(\mathbf{k}' - \mathbf{k})}{1 - U \chi^{zz}(\mathbf{k}' - \mathbf{k})} - \frac{\chi^{zz}(\mathbf{k}' - \mathbf{k})}{1 + U \chi^{zz}(\mathbf{k}' - \mathbf{k})} \right], \\
&= U + U^2 \chi_s(\mathbf{k}' + \mathbf{k}) + \frac{U^2}{2} [\chi_s(\mathbf{k}' - \mathbf{k}) - \chi_c(\mathbf{k}' + \mathbf{k})]. \tag{1.6.8}
\end{aligned}$$

Where χ_s and χ_c are spin susceptibility and charge susceptibility, respectively, within random phase approximations (RPA). In the paramagnetic phase, χ^{zz} and χ^{+-} are given by Lindhard susceptibility,

$$\chi_0(\mathbf{q}, i\omega_n) = \frac{1}{\Omega_{BZ}} \sum_{\mathbf{k}} \frac{f(\xi_{\mathbf{k}+\mathbf{q}}) - f(\xi_{\mathbf{k}})}{\xi_{\mathbf{k}+\mathbf{q}} - \xi_{\mathbf{k}} - i\omega_n}. \tag{1.6.9}$$

Where Ω_{BZ} is the area of BZ and ω_n is the bosonic Matsubara frequency. In the static case, Matsubara frequencies are neglected in the calculation.

Singlet potential

The singlet effective potential is given as [78, 79],

$$\begin{aligned}
V_{singlet}(\mathbf{k}, \mathbf{k}') &= \frac{1}{2} \left[\Gamma^{RPA}(\mathbf{k}', \mathbf{k}) + \Gamma^{RPA}(-\mathbf{k}', \mathbf{k}) \right], \\
&= \frac{1}{2} \left[2U + \frac{U^2}{2} \left(3\chi_s(\mathbf{k} - \mathbf{k}') - \chi_c(\mathbf{k} - \mathbf{k}') \right) + \frac{U^2}{2} \left(3\chi_s(\mathbf{k} + \mathbf{k}') \right. \right. \\
&\quad \left. \left. - \chi_c(\mathbf{k} + \mathbf{k}') \right) \right], \\
&= \frac{1}{2} \left[\Gamma_{singlet}(\mathbf{k} - \mathbf{k}') + \Gamma_{singlet}(\mathbf{k} + \mathbf{k}') \right]. \tag{1.6.10}
\end{aligned}$$

Where $\Gamma_{singlet}$ is given as,

$$\boxed{\Gamma_{singlet}(\mathbf{k} - \mathbf{k}') = U + \frac{U^2}{2} \left[3\chi_s(\mathbf{k} - \mathbf{k}') - \chi_c(\mathbf{k} - \mathbf{k}') \right]} \tag{1.6.11}$$

Triplet potential

The effective triplet potential is given by [79],

$$\begin{aligned}
 V_{triplet}(\mathbf{k}, \mathbf{k}') &= \frac{1}{2} \left[\Gamma^{RPA}(\mathbf{k}', \mathbf{k}) - \Gamma^{RPA}(-\mathbf{k}', \mathbf{k}) \right] \\
 &= -\frac{U^2}{2} \left[\chi_s(\mathbf{k} - \mathbf{k}') + \chi_c(\mathbf{k} - \mathbf{k}') + \chi_s(\mathbf{k} + \mathbf{k}') + \chi_c(\mathbf{k} + \mathbf{k}') \right] \\
 &= \frac{1}{2} \left[\Gamma_{triplet}(\mathbf{k} - \mathbf{k}') + \Gamma_{triplet}(\mathbf{k} + \mathbf{k}') \right] \tag{1.6.12}
 \end{aligned}$$

Where $\Gamma_{triplet}$ is given as,

$$\boxed{\Gamma_{triplet}(\mathbf{k} - \mathbf{k}') = -\frac{U^2}{2} \left[\chi_s(\mathbf{k} - \mathbf{k}') + \chi_c(\mathbf{k} - \mathbf{k}') \right]} \tag{1.6.13}$$

The singlet and triplet pairing potential given in Eq. (1.6.11) and Eq. (1.6.13) respectively depends upon the the Lindhard susceptibility, χ_0 [see Eq. (1.6.9)]. The divergence of χ_0 at the nesting vector gives a strong peak in the RPA spin susceptibility and corresponding pairing potential. Due to the factor $(1 - U\chi_0)$ in the denominator in spin susceptibility enhanced due to nesting, but charge susceptibility suppressed due to presence of $(1 + U\chi_0)$ in the denominator of charge susceptibility. Hence, we can say that the dominant effect to the spin-fluctuation potential comes from RPA spin-spin correlation function, spin channel, and charge channel is suppressed. This spin-fluctuation mediated pairing is believed to be the possible pairing mechanism in cuprates where Mott antiferromagnetic phase is in proximity with the superconductivity.

1.6.2 Spin-fluctuation potential in the multi-band Hubbard model

We consider a multi-band Hubbard model [80],

$$\begin{aligned}
H = & \sum_{\alpha,\beta,\mathbf{k},\sigma} \xi_{\alpha,\beta}(\mathbf{k}) c_{\mathbf{k},\alpha,\sigma}^\dagger c_{\mathbf{k},\beta,\sigma} + \sum_{\alpha} \sum_{\mathbf{k},\mathbf{k}',\mathbf{q}} U_{\alpha} c_{\mathbf{k},\alpha,\uparrow}^\dagger c_{\mathbf{k}',\alpha,\downarrow}^\dagger c_{\mathbf{k}'-\mathbf{q},\alpha,\downarrow} c_{\mathbf{k}+\mathbf{q},\alpha,\uparrow} \\
& + \sum_{\alpha<\beta} \sum_{\sigma,\sigma'} \sum_{\mathbf{k},\mathbf{k}',\mathbf{q}} \left[V_{\alpha,\beta} c_{\mathbf{k},\alpha,\sigma}^\dagger c_{\mathbf{k},\alpha,\sigma} c_{\mathbf{k}',\beta,\tilde{\sigma}}^\dagger c_{\mathbf{k}',\beta,\tilde{\sigma}} c_{\mathbf{k}'-\mathbf{q},\beta,\tilde{\sigma}} c_{\mathbf{k}+\mathbf{q},\alpha,\sigma} + \left(V_{\alpha,\beta} - J_H \right) c_{\mathbf{k},\alpha,\sigma}^\dagger \right. \\
& \left. c_{\mathbf{k}',\beta,\sigma}^\dagger c_{\mathbf{k}'-\mathbf{q},\beta,\sigma} c_{\mathbf{k}+\mathbf{q},\alpha,\sigma} \right] + \sum_{\alpha<\beta} \sum_{\sigma,\sigma'} \sum_{\mathbf{k},\mathbf{k}',\mathbf{q}} J_H c_{\mathbf{k},\alpha,\sigma}^\dagger c_{\mathbf{k}',\beta,\tilde{\sigma}}^\dagger c_{\mathbf{k}'-\mathbf{q},\alpha,\tilde{\sigma}} c_{\mathbf{k}+\mathbf{q},\beta,\sigma}.
\end{aligned} \tag{1.6.14}$$

Here, $c_{\mathbf{k},\alpha,\sigma}^\dagger$ and $c_{\mathbf{k},\beta,\sigma}$ are creation and annihilation operator for electron in orbital α and β . \mathbf{k} is the crystal momenta and σ is the \uparrow or \downarrow spin index, $\tilde{\sigma}$ is opposite of σ . In the multi-orbital model, Coulomb interaction U of the one-band model becomes an tensor of U_{α} , intra-orbital Coulomb interaction, $V_{\alpha,\beta}$ inter-orbital Coulomb interaction and J_H , Hund's coupling. We define a interaction tensor, $\tilde{U}_{s/c}$ for charge (c) and spin (s) fluctuations in the multi-orbital Hubbard model as [71, 80, 81]:

$$\tilde{U}_{s,\alpha,\alpha}^{\alpha,\alpha} = U, \quad \tilde{U}_{s,\alpha,\alpha}^{\beta,\beta} = \frac{1}{2} J_H, \quad \tilde{U}_{s,\alpha,\beta}^{\alpha,\beta} = \frac{1}{4} J_H + V, \tag{1.6.15}$$

$$\tilde{U}_{c,\alpha,\alpha}^{\alpha,\alpha} = U, \quad \tilde{U}_{c,\alpha,\alpha}^{\beta,\beta} = 2V, \quad \tilde{U}_{c,\alpha,\beta}^{\alpha,\beta} = \frac{3}{4} J_H - V. \tag{1.6.16}$$

All other components (e.g. pair hopping) of \tilde{U} are zero.

We now generalise the one-band spin-fluctuation potential in multi-orbital case. The spin operator for the orbital α :

$$\begin{aligned}
\mathcal{S}_{\alpha}^{+}(\mathbf{q}) &= \sum_{\mathbf{k}} c_{\mathbf{k},\alpha,\uparrow}^\dagger c_{\mathbf{k}+\mathbf{q},\alpha,\downarrow}, & \mathcal{S}_{\alpha}^{-}(\mathbf{q}) &= \sum_{\mathbf{k}} c_{\mathbf{k},\alpha,\downarrow}^\dagger c_{\mathbf{k}+\mathbf{q},\alpha,\uparrow}, \\
\mathcal{S}_{\alpha}^z(\mathbf{q}) &= \sum_{\mathbf{k}} [c_{\mathbf{k},\alpha,\uparrow}^\dagger c_{\mathbf{k}+\mathbf{q},\alpha,\uparrow} - c_{\mathbf{k},\alpha,\downarrow}^\dagger c_{\mathbf{k}+\mathbf{q},\alpha,\downarrow}]
\end{aligned} \tag{1.6.17}$$

Similarly, transverse and longitudinal susceptibilities are given by,

$$\left[\chi^{+-}(\mathbf{q}, \tau - \tau')\right]_{\alpha, \beta}^{\gamma, \delta} = - \sum_{\mathbf{k}} \mathcal{G}_{\mathbf{k}-\mathbf{q}, \alpha, \beta, \uparrow}(\tau' - \tau) \mathcal{G}_{\mathbf{k}, \gamma, \delta, \downarrow}(\tau - \tau'), \quad (1.6.18)$$

$$\left[\chi^{zz}(\mathbf{q}, \tau - \tau')\right]_{\alpha, \beta}^{\gamma, \delta} = - \sum_{\mathbf{k}, \sigma=\uparrow\downarrow} \mathcal{G}_{\mathbf{k}-\mathbf{q}, \alpha, \beta, \sigma}(\tau' - \tau) \mathcal{G}_{\mathbf{k}, \gamma, \delta, \sigma}(\tau - \tau'). \quad (1.6.19)$$

The single-particle Green's function in the orbital basis is defined as, [81]

$$\mathcal{G}_{\mathbf{k}, \alpha, \beta, \sigma}(\tau - \tau') = - \left\langle T_{\tau} c_{\mathbf{k}, \alpha, \sigma}(\tau) c_{\mathbf{k}, \beta, \sigma}^{\dagger}(\tau') \right\rangle. \quad (1.6.20)$$

A unitary transformation (\mathcal{U}) can diagonalize the non-interacting part of the Hamiltonian Eq. (1.6.14), into band basis (ν), $c_{\mathbf{k}, \alpha, \sigma} = \sum_{\nu} \mathcal{U}_{\alpha}^{\nu} \gamma_{\mathbf{k}, \nu, \sigma}$. The orthogonality condition of the eigenvectors are satisfied by, $\sum_{\alpha} \mathcal{U}_{\alpha}^{\nu} [\mathcal{U}_{\alpha}^{\nu'}]^{\dagger} = \delta_{\nu\nu'}$.

In Matsubara frequency space, the Green's function is given by,

$$\mathcal{G}_{\mathbf{k}, \alpha, \beta, \sigma}(ik_n) = \sum_{\nu} \frac{\phi_{\alpha}^{\nu}(\mathbf{k}) \phi_{\beta}^{\dagger \nu}(\mathbf{k})}{ik_n - E_{\nu}(\mathbf{k})}, \quad (1.6.21)$$

where, $\phi_{\alpha}^{\nu}(\mathbf{k})$ and $E_{\nu}(\mathbf{k})$ are the eigenfunction and eigenvalues of the non-interacting Hamiltonian Eq.(1.6.14), ϕ^{\dagger} is the Hermitian conjugate of ϕ . The non-interacting density-density response function is known as Lindhard susceptibility, which we define in Eq. (1.6.9), now for the multi-orbital case we get,

$$\begin{aligned} [\chi_0(\mathbf{q})]_{\alpha\beta}^{\gamma\delta} &= - \frac{1}{\Omega_{BZ}} \sum_{\mathbf{k}, \nu\nu'} \phi_{\beta}^{\nu}(\mathbf{k}) \phi_{\alpha}^{\nu \dagger}(\mathbf{k}) \phi_{\delta}^{\nu'}(\mathbf{k} + \mathbf{q}) \phi_{\gamma}^{\nu' \dagger}(\mathbf{k} + \mathbf{q}) \\ &\quad \times \frac{f(E_{\nu'}(\mathbf{k} + \mathbf{q})) - f(E_{\nu}(\mathbf{k}))}{E_{\nu'}(\mathbf{k} + \mathbf{q}) - E_{\nu}(\mathbf{k}) + i\epsilon}. \end{aligned} \quad (1.6.22)$$

RPA spin and charge susceptibilities are,

$$\tilde{\chi}_{s/c}(\mathbf{q}) = \tilde{\chi}_0(\mathbf{q}) \left(\tilde{\mathbb{I}} \mp \tilde{U}_{s/c} \tilde{\chi}_0(\mathbf{q}) \right)^{-1}, \quad (1.6.23)$$

where $\tilde{\mathbb{I}}$ is the unit matrix. $\tilde{\chi}_{s/c}$ are the density-density correlators (tensors in the same orbital basis) for the spin and charge density channels.

By expanding the interaction term to multiple interaction channels [see Fig. 1.14], and collecting the terms which give a pairing interaction (both singlet and triplet channels are considered) we obtain the effective pairing potential, $\Gamma_{\alpha\beta}^{\gamma\delta}(\mathbf{q})$ as [71, 72, 73, 74] The pairing potentials in the singlet ($\tilde{\Gamma}_s$) and triplet ($\tilde{\Gamma}_t$) channels are,

$$\tilde{\Gamma}_s(\mathbf{q}) = \frac{1}{2} [3\tilde{U}_s\tilde{\chi}_s(\mathbf{q})\tilde{U}_s - \tilde{U}_c\tilde{\chi}_c(\mathbf{q})\tilde{U}_c + \tilde{U}_s + \tilde{U}_c], \quad (1.6.24a)$$

$$\tilde{\Gamma}_t(\mathbf{q}) = -\frac{1}{2} [\tilde{U}_s\tilde{\chi}_s(\mathbf{q})\tilde{U}_s + \tilde{U}_c\tilde{\chi}_c(\mathbf{q})\tilde{U}_c]. \quad (1.6.24b)$$

The strong FS nesting features captured within the Lindhard susceptibility in Eq. (1.6.22) is automatically translated into strong peaks in the RPA susceptibilities in Eq. (1.6.23). The RPA denominator for the spin channel, having value < 1 , enhances the FS nesting strength in the bare susceptibility $\tilde{\chi}_0(\mathbf{q})$. On the other hand, the RPA denominator for the charge channel is > 1 suppressing the charge fluctuations. In addition, the zeros of the RPA denominator for the spin can render new collective modes with dispersion defined by $\tilde{\mathbb{I}} = \tilde{U}_s\tilde{\chi}_0(\mathbf{q})$. These are called magnon peaks and are strongly suppressed in the optimal hole doping region of YBCO, being away from the AFM critical point. [3, 82, 83]. Finally, all the strong FS nesting features in the RPA susceptibilities directly enter into the SC pairing channels through Eqs. (1.6.24a), and (1.6.24b) and determine the pairing symmetry accordingly.

Interacting part of the Hamiltonian Eq. (1.6.14) becomes,

$$H_{\text{int}} \approx \frac{1}{\Omega_{\text{BZ}}^2} \sum_{\alpha\beta\gamma\delta} \sum_{\mathbf{k}\mathbf{q},\sigma\sigma'} \Gamma_{\alpha\beta}^{\gamma\delta}(\mathbf{q}) c_{\alpha\sigma}^\dagger(\mathbf{k}) c_{\beta\sigma'}^\dagger(-\mathbf{k}) c_{\gamma\sigma'}(-\mathbf{k}-\mathbf{q}) c_{\delta\sigma}(\mathbf{k}+\mathbf{q}). \quad (1.6.25)$$

$\sigma' = \pm\sigma$ give triplet and singlet pairing channels, respectively. Eq. (1.6.25) gives the pairing interaction for pairing between orbitals. However, we solve the BCS gap equation in the band basis. To make this transformation, we make use of the unitary transformation, $c_{\mathbf{k},\alpha,\sigma} = \sum_{\nu} \mathcal{U}_{\alpha}^{\nu} \gamma_{\mathbf{k},\nu,\sigma}$, for all \mathbf{k} and spin σ . With this

substitution we obtain the pairing interaction Hamiltonian in the band basis as

$$H_{\text{int}} \approx \sum_{\nu\nu'} \sum_{\mathbf{k}\mathbf{q},\sigma\sigma'} \Gamma'_{\nu\nu'}(\mathbf{k}, \mathbf{q}) \frac{1}{\Omega_{\text{BZ}}^2} \gamma_{\nu\sigma}^\dagger(\mathbf{k}) \gamma_{\nu\sigma'}^\dagger(-\mathbf{k}) \gamma_{\nu'\sigma'}(-\mathbf{k} - \mathbf{q}) \gamma_{\nu'\sigma}(\mathbf{k} + \mathbf{q}). \quad (1.6.26)$$

The same equation holds for both singlet and triplet pairing and thus henceforth we drop the corresponding symbol for simplicity. The band pairing interaction $\Gamma'_{\nu\nu'}$ is related to the corresponding orbital one as,

$$\Gamma'_{\nu\nu'}(\mathbf{k}, \mathbf{q}) = \sum_{\alpha\beta\gamma\delta} \Gamma_{\alpha\beta}^{\gamma\delta}(\mathbf{q}) \phi_\alpha^{\nu\dagger}(\mathbf{k}) \phi_\beta^{\nu\dagger}(-\mathbf{k}) \phi_\gamma^{\nu'}(-\mathbf{k} - \mathbf{q}) \phi_\delta^{\nu'}(\mathbf{k} + \mathbf{q}) \quad (1.6.27)$$

We define the SC gap in the ν^{th} -band as

$$\Delta_\nu(\mathbf{k}) = -\frac{1}{\Omega_{\text{BZ}}} \sum_{\nu',\mathbf{q}} \Gamma'_{\nu\nu'}(\mathbf{k}, \mathbf{q}) \langle \gamma_{\nu'\sigma'}(-\mathbf{k} - \mathbf{q}) \gamma_{\nu'\sigma}(\mathbf{k} + \mathbf{q}) \rangle, \quad (1.6.28)$$

where the expectation value is taken over the BCS ground state. In the limit $T \rightarrow 0$ we have $\langle \gamma_{\nu\sigma}(-\mathbf{k}) \gamma_{\nu\sigma}(\mathbf{k}) \rangle \rightarrow \lambda \Delta_\nu(\mathbf{k})$, with λ is the SC coupling constant. Substituting this in Eq. (1.6.28), we get

$$\Delta_\nu(\mathbf{k}) = -\lambda \frac{1}{\Omega_{\text{BZ}}} \sum_{\nu',\mathbf{q}} \Gamma'_{\nu\nu'}(\mathbf{k}, \mathbf{q}) \Delta_{\nu'}(\mathbf{k} + \mathbf{q}). \quad (1.6.29)$$

This is an eigenvalue equation of the pairing potential $\Gamma'_{\nu\nu'}(\mathbf{q} = \mathbf{k} - \mathbf{k}')$ with eigenvalue λ and eigenfunction $\Delta_\nu(\mathbf{k})$. The \mathbf{k} -dependence of $\Delta_\nu(\mathbf{k})$ dictates the pairing symmetry for a given eigenvalue. While there are many solutions (as many as the \mathbf{k} -grid), however, we consider the highest eigenvalue since this pairing symmetry can be shown to have the lowest Free energy value in the SC state.[72].

Chapter 2

Novel attractive pairing interaction in heavy fermions

2.1 Introduction

The first HF superconductor CeCu_2Si_2 [11] was widely believed to be an unconventional superconductor.[84, 85, 86, 87] Subsequently, more HF superconductors,[2] followed by cuprate, and pnictide superconductors are discovered to feature unconventional pairings with either nodal d -wave, or nodeless but sign-reversal s^\pm -pairing symmetry, or their various irreducible combinations.[4] In particular, it is widely argued by various groups that the vertex correction due to valence-fluctuation exchange can directly mediate a pairing channel,[86, 88, 89] or can augment pairing strength arising from other sources[90, 91]. Kondo coupling can induce various unconventional pairings.[87, 92, 93, 94, 95, 96, 97] Following the overwhelming evidence of conventional pairing symmetry, the electron-phonon coupling problem with strong Coulomb interaction is revisited recently.[80, 91, 98] In general, electron-phonon coupling, if present, can be overturned by the strong on-site Coulomb repulsion in the HF quasiparticles exhibiting effective mass $\sim 10^3$ times the bare mass.

However, the pairing symmetry, and the pairing mechanism in the first-discovered HF compound CeCu_2Si_2 are recently called into questions. Earlier reports of nuclear quadrupole resonance (NQR) data revealed a T^3 behavior in the relaxation

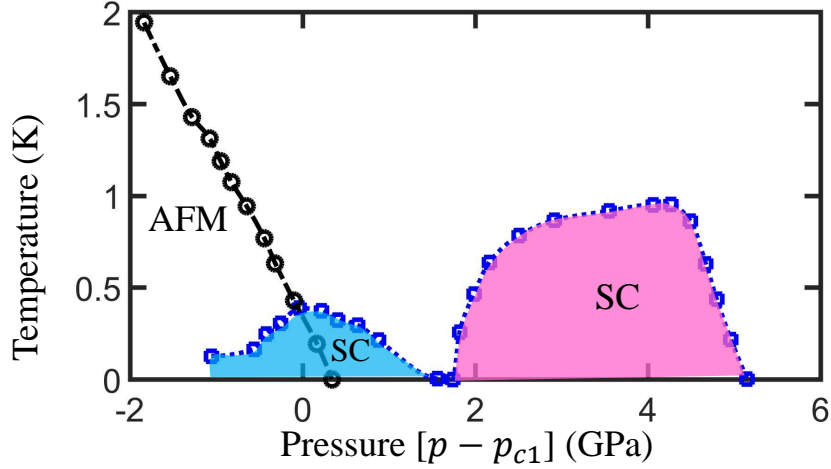


Figure 2.1: Experimental phase diagram of CeCu_2Si_2 . The AFM and SC transition temperature variation is shown as a function of relative pressure. For pure CeCu_2Si_2 p_{c1} is 0.4 GPa. We replot the figure by using the data given in paper [112].

rate without a coherence peak, suggesting the presence of line nodes in the SC gap structure.[99, 100, 101] Observation of four-fold modulation in the upper critical field H_{c2} in CeCu_2Si_2 can predict a point-node d -wave pairing state[102], provided the FS anisotropy is small enough to cause the same modulation.[103] Finally, the observation of a spin resonance in the SC state by inelastic neutron scattering measurement[104] can be interpreted as to arise from sign-reversal of the SC gap if the resonance peak is very sharp and its energy lies within the SC gap amplitude. More recently, counter-evidence of fully gapped superconductivity are obtained in various measurements including point-contact tunneling spectroscopy,[105, 106] specific heat,[107, 108, 109] magnetic penetration depth,[109, 110] and thermal conductivity[109]. The field-angle dependence of the specific heat data also shows no evidence of gap anisotropy.[108] Furthermore, the observed robustness of superconductivity to disorder supports the absence of sign-reversal in the pairing symmetry scenario.[109, 111] These results collectively signal towards a conventional, isotropic pairing symmetry in CeCu_2Si_2 .

CeCu_2Si_2 has an interesting phase diagram [see Fig. 2.1] exhibiting two SC domes under pressure, with an AFM QCP lying beneath the first SC dome, while

a valence fluctuation critical point is possibly present at the second dome.[112, 113, 3] The valence fluctuation, which is ubiquitous in HF compounds, can promote superconductivity with unconventional pairing mechanism.[85, 86, 88, 89, 112, 113].

Our present work is motivated by the question: Can there be other source of attractive potential for superconductivity in general? Here, we provide a new mechanism of attractive potential originating from the interplay between the Coulomb interaction and valence fluctuations. The physical picture is illustrated in Fig. 2.2. When the Coulomb interaction is strong on the f -electron's site, double f -electron's occupancy is prohibited. Within the field theory view, a singly occupied f -electron site is annexed with an unoccupied f -state – a bosonic holon field – which repels another f -electrons to occupy the state. However, the unoccupied f -site can be occupied by a conduction electron since the presence of valence fluctuation channel allows mutation between the f - and conduction electrons. Remarkably, we show here that the doubly occupied state with f - and conduction electrons condense like a Cooper pair. Mathematically, as we integrate out the boson fields (unoccupied holons), we obtain a robust, new attractive potential channel between the conduction electrons and singly occupied f -sites, naturally commencing onsite, constant sign, s -wave like superconductivity. Conceptually, this process is somewhat analogous to the theory of meson mediated attractive nuclear force, except here the attraction commences between onsite electrons. We formulate the corresponding theory of superconductivity, and find excellent agreement with the recently observed fully gap, constant sign gap features in CeCu₂Si₂, [105, 106, 107, 108, 109, 110, 111] as well as in the Yb-doped CeCoIn₅ superconductors[114]. We predict definite relationship between SC T_c and valence fluctuation (coherence) temperature T_K , and other unique properties of the present theory.

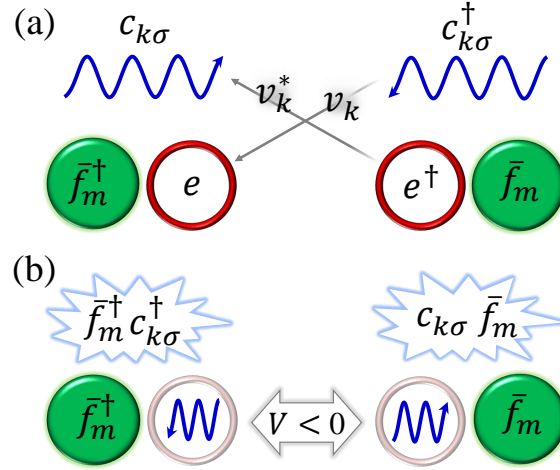


Figure 2.2: Illustration of the valence fluctuation mediated attractive potential. (a) The unoccupied state (holon) in each valence fluctuation term can attract another conduction electron through the valence fluctuation channel. The conjugate process also occurs simultaneously. Wavy lines depict conduction electrons (c, c^\dagger), while filled (\bar{f}, \bar{f}^\dagger) and open (e, e^\dagger) circles give singly occupied and unoccupied f -sites, respectively. Bar symbol over f -operators emphasize that they are single- f -electrons occupied states. Arrows dictate valence fluctuation channels. (b) As we integrate out the unoccupied states (e, e^\dagger), we obtain an effective interaction $V < 0$, forming Cooper pair between the single site \bar{f} -electron and conduction c electron.

2.2 Field theory treatment of the hole states and effective attractive potential

The Hamiltonian of the slave-boson model is given by,

$$H = \sum_{\mathbf{k}, \sigma} \xi_{\mathbf{k}} c_{\mathbf{k}\sigma}^\dagger c_{\mathbf{k}\sigma} + \xi_{\bar{f}} \sum_m \bar{f}_m^\dagger \bar{f}_m + \omega_e e^\dagger e + \sum_{\mathbf{k}, \sigma, m} \left(v_{\mathbf{k}} c_{\mathbf{k}\sigma}^\dagger e^\dagger \bar{f}_m + v_{\mathbf{k}}^\dagger \bar{f}_m^\dagger e c_{\mathbf{k}\sigma} \right). \quad (2.2.1)$$

We discussed this Hamiltonian in the previous chapter, Eq. (1.3.41). Here, we ignore the constant ω_e term of Eq. (1.3.41), which is a constant shift of the energy state. The action of the Hamiltonian in Eq. (2.2.1) is broken into four components,

$$S = S_c + S_{\bar{f}} + S_e + S_v, \quad (2.2.2)$$

where

$$\mathcal{S}_c = \int d\tau \sum_{\mathbf{k},\sigma} \tilde{c}_{\mathbf{k}\sigma}(\tau)(\partial_\tau + \xi_{\mathbf{k}})c_{\mathbf{k}\sigma}(\tau), \quad (2.2.3)$$

$$\mathcal{S}_{\bar{f}} = \int d\tau \sum_m \tilde{\bar{f}}_m(\tau)(\partial_\tau + \bar{\xi}_f)\bar{f}_m(\tau), \quad (2.2.4)$$

$$\mathcal{S}_e = \int d\tau \tilde{e}(\tau)(\partial_\tau + \omega_e)e(\tau), \quad (2.2.5)$$

$$\mathcal{S}_v = \int d\tau \sum_{\mathbf{k},\sigma,m} \left(v_{\mathbf{k}} \tilde{c}_{\mathbf{k}\sigma}(\tau) \tilde{e}(\tau) \bar{f}_m(\tau) + \text{h.c.} \right). \quad (2.2.6)$$

Here \tilde{e}, e are bosonic coherent states and $\tilde{f}, \bar{f}, \tilde{c}, c$ are Grassmann variables for singly occupied f -states, and conduction electrons respectively ('tilde' means conjugation). τ is imaginary time axis. Thermodynamic properties of the system can be calculated from the partition function $\mathcal{Z} = \text{Tr}e^{-\mathcal{S}}$, where the trace is taken over all degrees of freedom of the system. We obtain an effective action \mathcal{S}_{eff} by integrating out the bosonic variables \tilde{e}, e as

$$\begin{aligned} \mathcal{Z} &= \int \mathcal{D}[\tilde{c}, c] \mathcal{D}[\tilde{f}, \bar{f}] \mathcal{D}[\tilde{e}, e] e^{-\mathcal{S}_c - \mathcal{S}_{\bar{f}} - \mathcal{S}_e - \mathcal{S}_v}, \\ &= \int \mathcal{D}[\tilde{c}, c] \mathcal{D}[\tilde{f}, \bar{f}] e^{-\mathcal{S}_c - \mathcal{S}_{\bar{f}}} \int \mathcal{D}[\tilde{e}, e] e^{-\mathcal{S}_e - \mathcal{S}_v}, \\ &= \int \mathcal{D}[\tilde{c}, c] \mathcal{D}[\tilde{f}, \bar{f}] e^{-\mathcal{S}_{\text{eff}}[\tilde{c}, c, \tilde{f}, \bar{f}]}, \end{aligned} \quad (2.2.7)$$

where

$$\mathcal{S}_{\text{eff}} = \mathcal{S}_c + \mathcal{S}_{\bar{f}} - \ln \int \mathcal{D}[\tilde{e}, e] e^{-\mathcal{S}_e - \mathcal{S}_v}. \quad (2.2.8)$$

It is easier to perform the τ integration in the Matsubara frequency space. The Fourier transformation to the Matsubara frequency domain of the $e(\tau)$ variable gives $e(\tau) = \frac{1}{\sqrt{\beta}} \sum_n e_n \exp(-i\omega_n \tau)$, where $i\omega_n$ is bosonic Matsubara frequency and $e_n = e(i\omega_n)$. In the Matsubara space, we get

$$\mathcal{S}_e = - \sum_n \tilde{e}_n (\mathcal{G}^e)^{-1}(i\omega_n) e_n, \quad (2.2.9)$$

where \mathcal{G}^e is the bare Green's function for the e_n -states: $(\mathcal{G}^e)^{-1} = i\omega_n - \omega_e$.

Next we define a bosonic hybridization field $\rho_{\mathbf{k}\sigma m}$ as

$$\rho_{\mathbf{k}\sigma m}(\tau) = \tilde{c}_{\mathbf{k}\sigma}(\tau)\bar{f}_m(\tau), \quad (2.2.10)$$

whose Fourier component is $\rho_{\mathbf{k}\sigma m}(\tau) = \frac{1}{\sqrt{\beta}} \sum_n \rho_{\mathbf{k}\sigma m, n} \exp(-i\omega_n \tau)$, where $\rho_{\mathbf{k}\sigma m, n} = \rho_{\mathbf{k}\sigma m}(i\omega_n)$ with $i\omega_n$ being the bosonic Matsubara frequency. Hence we can express the hybridization action as

$$\begin{aligned} \mathcal{S}_v &= \int_0^\beta d\tau \sum_{\mathbf{k}, \sigma, m} (v_{\mathbf{k}} \tilde{e}(\tau) \rho_{\mathbf{k}\sigma m}(\tau) + v_{\mathbf{k}}^* \tilde{\rho}_{\mathbf{k}\sigma m}(\tau) e(\tau)), \\ &= \sum_{\mathbf{k}, \sigma, m} \sum_n (v_{\mathbf{k}} \tilde{e}_n \rho_{\mathbf{k}\sigma m, n} + v_{\mathbf{k}}^* \tilde{\rho}_{\mathbf{k}\sigma m, n} e_n). \end{aligned} \quad (2.2.11)$$

Interestingly, now in Eqs. (2.2.9),(2.2.11) the integration over τ -variable is replaced with summation over discrete Matsubara frequencies n . Let us say at a given temperature we have N number of Matsubara frequencies. So we define a bosonic spinor $\mathbf{E} = (e_1, e_2, \dots, e_N)^T$, and $\tilde{\mathbf{E}} = (\tilde{e}_1, \tilde{e}_2, \dots, \tilde{e}_N)$. Similarly, we define a vector for the hybridization field as $\mathbf{V} = (\mathbf{v}_1, \mathbf{v}_2, \dots, \mathbf{v}_N)^T$, $\tilde{\mathbf{V}} = (\tilde{\mathbf{v}}_1, \tilde{\mathbf{v}}_2, \dots, \tilde{\mathbf{v}}_N)$ where $\mathbf{v}_n = \sum_{\mathbf{k}\sigma m} v_{\mathbf{k}} \rho_{\mathbf{k}\sigma m, n}$, and $\tilde{\mathbf{v}}_n = \sum_{\mathbf{k}\sigma m} v_{\mathbf{k}}^* \tilde{\rho}_{\mathbf{k}\sigma m, n}$. Finally, we define a diagonal matrix \mathbf{G}^{-1} for the inverse Green's function $(\mathcal{G}^e)^{-1}$ in Eq. (2.2.9), whose components are $\mathbf{G}_{nn}^{-1} = (\mathcal{G}_e)^{-1} = i\omega_n - \omega_e$. Hence we can express Eqs. (2.2.9),(2.2.11) respectively as

$$\mathcal{S}_e = - \tilde{\mathbf{E}} \cdot \mathbf{G}^{-1} \cdot \mathbf{E}, \quad (2.2.12)$$

$$\mathcal{S}_v = \tilde{\mathbf{E}} \cdot \mathbf{V} + \tilde{\mathbf{V}} \cdot \mathbf{E}. \quad (2.2.13)$$

Therefore, the last term of Eq. (2.2.8) can be evaluated as

$$\int \mathcal{D}[\tilde{\mathbf{E}}, \mathbf{E}] e^{-\mathcal{S}_e - \mathcal{S}_v} = \pi^N \det \mathbf{G}^{-1} e^{-[\tilde{\mathbf{V}} \cdot \mathbf{G}^{-1} \cdot \mathbf{V}]}. \quad (2.2.14)$$

(We ignored some irrelevant constant factors). The factor of the exponent on the right hand side of Eq. (2.2.14) can now be evaluated rigorously. In $T \rightarrow 0$ limit, the

Matsubara frequencies span from $n = -\infty$ to ∞ . Hence we obtain,

$$\begin{aligned}
 & \tilde{\mathbf{V}} \cdot \mathbf{G}^{-1} \cdot \mathbf{V} \\
 &= - \sum_{\substack{\mathbf{k}, \sigma, m \\ \mathbf{k}', \sigma', m'}} \sum_{n=-\infty}^{\infty} v_{\mathbf{k}}^* \tilde{\rho}_{\mathbf{k}\sigma m, n} \frac{1}{-i\omega_n + \omega_e} v_{\mathbf{k}'} \rho_{\mathbf{k}\sigma' m', n} \\
 &= \sum_{\substack{\mathbf{k}, \sigma, m \\ \mathbf{k}', \sigma', m'}} \sum_{n=0}^{\infty} v_{\mathbf{k}}^* v_{\mathbf{k}'} \frac{2\omega_e}{(i\omega_n)^2 - \omega_e^2} \tilde{\rho}_{\mathbf{k}\sigma m, n} \rho_{\mathbf{k}\sigma' m', n} \\
 &= \sum_{\substack{\mathbf{k}, \sigma, m \\ \mathbf{k}', \sigma', m'}} \sum_{n=0}^{\infty} V_{\mathbf{k}\mathbf{k}'} \tilde{f}_m(i\omega_n) c_{\mathbf{k}, \sigma}(i\omega_n) \tilde{c}_{\mathbf{k}', \sigma'}(i\omega_n) \bar{f}_{m'}(i\omega_n).
 \end{aligned} \tag{2.2.15}$$

In the last equation, we have substituted the hybridization field into fermionic field from Eq. (2.2.10). The effective potential is

$$V_{\mathbf{k}\mathbf{k}'} = v_{\mathbf{k}}^* v_{\mathbf{k}'} \frac{2\omega_e}{(i\omega_n)^2 - \omega_e^2}. \tag{2.2.16}$$

So we obtain effective interacting Hamiltonian as,

$$H_{\text{eff}} = \sum_{\mathbf{k}, \sigma} \xi_{\mathbf{k}} c_{\mathbf{k}\sigma}^\dagger c_{\mathbf{k}\sigma} + \bar{\xi}_f \sum_m \bar{f}_m^\dagger \bar{f}_m + \sum_{\mathbf{k}\mathbf{k}', \sigma\sigma', mm'} V_{\mathbf{k}\mathbf{k}'} c_{\mathbf{k}\sigma}^\dagger \bar{f}_m \bar{f}_{m'}^\dagger c_{\mathbf{k}'\sigma'}. \tag{2.2.17}$$

Usually, the chemical potential is used to fix the total number of particles of the entire system. In our theory, we assume a fixed number of electrons at every site. The number operator at every site commutes with the Hamiltonian. This, naturally gives a local chemical potential denoted by ω_e in our theory. The chemical potential acts as a local gauge field. We assume no spatial dependence of the gauge field. In the presence of a uniform gauge field, all holons condensate to the same frequency.

Spin conservation leads to $\sigma + m = \sigma' + m'$.

The most impressive aspect of the above result lies in the form of the effective

potential

$$V_{\mathbf{k}\mathbf{k}'}(i\omega_n) = v_{\mathbf{k}}v_{\mathbf{k}'}^\dagger \frac{2\omega_e}{(i\omega_n)^2 - \omega_e^2}, \quad (2.2.18)$$

where $i\omega_n$ is the bosonic Matsubara frequency. In what follows, in the low energy limit $i\omega_n < \omega_e$ and $\omega_e > 0$ (since holon's energy is generally positive), Eq. (2.2.18) produces an attractive potential. This is one of our principle results of this work. As in the case of the BCS theory,[6] we consider here the static limit $i\omega_n \rightarrow 0$ limit, yielding

$$V_{\mathbf{k}\mathbf{k}'} = -\frac{2v_{\mathbf{k}}v_{\mathbf{k}'}^\dagger}{\omega_e} < 0. \quad (2.2.19)$$

We interpret the origin of attractive potential as following. Each valence fluctuation process generates (or annihilates) a boson field e^\dagger (e), whose job is to prohibit double occupancy on the f -sites. However, the unoccupied states or holons can attract another conduction electron (and vice versa), i.e., they trigger another valence fluctuation process. The two valence fluctuations process can be tied together to generate an effective interaction potential, which turns out to be attractive at low-energy [see Fig. 2.2].

For a generic attractive potential, the pair correlation function has a logarithm divergence with temperature (see 2.4.1), and we have a SC ground state. Looking at Eq. (2.2.17), we find that the Cooper pairs form here between the conduction electron and singly occupied \bar{f}_m -site with the SC gap parameter defined as

$$\Delta_{\mathbf{k}} = \frac{2v_{\mathbf{k}}}{\omega_e} \sum_{\mathbf{k}'} v_{\mathbf{k}'}^\dagger \langle c_{\mathbf{k}'\sigma} \bar{f}_m \rangle. \quad (2.2.20)$$

Here we make few observations. (i) This is an inter-band pairing between the spin- $\frac{1}{2}$ conduction electron and single-site f -electron with m multiplet. (ii) The \mathbf{k} -dependence of the SC gap is solely determined by that of the hybridization term $v_{\mathbf{k}}$ in Eq. (2.2.19). (iii) This is a finite-momentum pairing, but unlike the Fulde-Ferrel-Larkin-Ovchinnikov state (FFLO) or the pair density wave state, here the Cooper pair solely absorbs the conduction electron's momentum. (For dispersive, narrow f -band, which is often the case in many HF systems, Cooper pairs can

have zero center-of-mass momentum.) (iv) The SC state, in general, does not have the particle-hole symmetry, unless at $\xi_{\mathbf{k}} = \bar{\xi}_f$. (v) Symmetry of the Cooper pairs is dictated by the values of m , σ , and the parity of $V_{\mathbf{k}\mathbf{k}'}$. In CeCu_2Si_2 , the hybridization occurs between the Ce- f and Ce- d orbitals of the same Ce-atom,[115] and thus the hybridization potential can be considered as onsite, i.e., $v_{\mathbf{k}} = v$. For onsite hybridization, one expects a spin-singlet pair for $m = \pm 1/2$ (or higher order antisymmetric spin component if $|m| > 1/2$). For an attractive potential, spin-singlet, onsite (s -wave) pairing state has the highest eigenvalue as obtained in the BCS case as well.[6]

2.3 Mean-field results and critical phenomena

So far, we have obtained all results exactly. We now invoke the mean-field theory for superconductivity. The effective mean-field Hamiltonian reads

$$H_{\text{MF}} = \sum_{\mathbf{k}\sigma} \xi_{\mathbf{k}} c_{\mathbf{k}\sigma}^\dagger c_{\mathbf{k}\sigma} + \bar{\xi}_f \sum_m \bar{f}_m^\dagger \bar{f}_m + \sum_{\mathbf{k}\sigma m} \Delta_{\mathbf{k}} \bar{f}_m^\dagger c_{\mathbf{k}\sigma}^\dagger + \text{h.c.} \quad (2.3.1)$$

We use the Nambu-Gorkov basis $\psi_{\mathbf{k}} = (c_{\mathbf{k}\sigma} \quad \bar{f}_m^\dagger)^T$, in which the mean-field Hamiltonian (Eq. (2.3.1)) reads

$$H_{\text{MF}}(\mathbf{k}) = \xi_{\mathbf{k}}^- I_{2 \times 2} + \xi_{\mathbf{k}}^+ \sigma_z - \Delta_{\mathbf{k}} \sigma_x, \quad (2.3.2)$$

where σ_i are the 2×2 Pauli matrices and $I_{2 \times 2}$ is a unit matrix. $\xi_{\mathbf{k}}^\pm = (\xi_{\mathbf{k}} \pm \bar{\xi}_f)/2$. The BdG eigenvalues are

$$E_{\mathbf{k}}^\pm = \xi_{\mathbf{k}}^- \pm E_{0\mathbf{k}}, \quad \text{with } E_{0\mathbf{k}} = \sqrt{(\xi_{\mathbf{k}}^+)^2 + |\Delta_{\mathbf{k}}|^2}. \quad (2.3.3)$$

The Bogoliubov operators for the two eigenvalues $E_{\mathbf{k}}^\pm$ are

$$\begin{pmatrix} \phi_{\mathbf{k}}^+ \\ (\phi_{\mathbf{k}}^-)^\dagger \end{pmatrix} = \begin{pmatrix} \alpha_{\mathbf{k}}^+ & -\alpha_{\mathbf{k}}^- \\ \alpha_{\mathbf{k}}^- & \alpha_{\mathbf{k}}^+ \end{pmatrix} \begin{pmatrix} c_{\mathbf{k}\sigma} \\ \bar{f}_m^\dagger \end{pmatrix}. \quad (2.3.4)$$

where

$$(\alpha_{\mathbf{k}}^{\mp})^2 = \frac{1}{2} \left(1 \mp \frac{\xi_{\mathbf{k}}^+}{E_{0\mathbf{k}}} \right), \quad (2.3.5)$$

Evaluating the self-consistent gap equation from Eq. (2.2.20), we get Eq. (2.3.6). The corresponding self-consistent gap equation is,

$$\Delta_{\mathbf{k}} = \frac{2v_{\mathbf{k}}}{\omega_e} \sum_{\mathbf{k}'} v_{\mathbf{k}'}^* \frac{\Delta_{\mathbf{k}'}}{4E_{0\mathbf{k}'}} \sum_{\nu=\pm} \nu \tanh \left(\frac{\beta E_{\mathbf{k}'\nu}}{2} \right). \quad (2.3.6)$$

$\nu = \pm$ are the two quasiparticle bands: $E_{\mathbf{k}}^{\pm} = \xi_{\mathbf{k}}^{\mp} \pm E_{0\mathbf{k}}$, where $E_{0\mathbf{k}} = \sqrt{(\xi_{\mathbf{k}}^+)^2 + |\Delta_{\mathbf{k}}|^2}$, and $\xi_{\mathbf{k}}^{\pm} = (\xi_{\mathbf{k}} \pm \bar{\xi}_f)/2$. $\beta = 1/k_B T$.

2.3.1 Transition temperature T_c

For the attractive potential, onsite pairing is more favorable. Hence we set $V_{\mathbf{k}\mathbf{k}'} = -2|v|^2/\omega_e$. In this case, superconducting transition temperature T_c can be obtained by taking the limits of $\Delta \rightarrow 0$, which renders $E_{\mathbf{k}}^+ \rightarrow \xi_{\mathbf{k}}$, $E_{\mathbf{k}}^- \rightarrow -\bar{\xi}_f$, $E_{0\mathbf{k}} \rightarrow \frac{|\xi_{\mathbf{k}} + \bar{\xi}_f|}{2}$. From Eq. (2.3.6) we obtain

$$1 = \lambda \int_{-D}^D \frac{d\xi}{2(\xi + \bar{\xi}_f)} \left[\tanh \left(\frac{\beta_c \xi}{2} \right) + \tanh \left(\frac{\beta_c \bar{\xi}_f}{2} \right) \right], \quad (2.3.7)$$

where we have substituted $\lambda = 2N|v|^2/\omega_e$. $\beta_c = 1/k_B T_c$. The first integral in Eq. (2.3.7) is a tricky one. In the limit of $D \gg \bar{\xi}_f$, we can approximately evaluate this integral. The first integral of Eq. (2.3.7) gives

$$I_1 \approx \lambda \ln \left[\frac{2D\gamma}{\sqrt{\bar{\xi}_f^2 + (2k_B T_c)^2}} \right], \quad (2.3.8)$$

where $D\gamma = 2D\gamma/\pi$ with $\gamma = 1.78$ being the Euler constant. The second integral is trivial to evaluate which gives

$$I_2 = \lambda \tanh \left(\frac{\beta_c \bar{\xi}_f}{2} \right) \ln \left| \frac{D + \bar{\xi}_f}{-D + \bar{\xi}_f} \right|. \quad (2.3.9)$$

In the limit of $D > \bar{\xi}_f$, $I_2 \rightarrow 0$. Therefore, we are left with $I_1 = 1$, which gives,

$$(k_B T_c)^2 = D_\gamma^2 e^{-2/\lambda} - \frac{\bar{\xi}_f^2}{4}, \quad (2.3.10)$$

~~Eq. (8) in the main text is obtained from the above equation.~~

2.3.2 SC gap amplitude

Next we take the $T \rightarrow 0$ limit in Eq. (2.3.6). In this limit, we get $\tanh(\frac{\beta E_{\mathbf{k}}^\pm}{2}) \rightarrow \pm 1$. Hence we are left with

$$\begin{aligned} 1 &= \lambda \int_{-D}^D \frac{d\xi}{\sqrt{(\xi + \bar{\xi}_f)^2 + 4\Delta^2}}, \\ &= \lambda \ln \left(\frac{\sqrt{(D + \bar{\xi}_f)^2 + 4\Delta^2} + D + \bar{\xi}_f}{\sqrt{(D - \bar{\xi}_f)^2 + 4\Delta^2} - D + \bar{\xi}_f} \right), \\ &\approx \lambda \ln \left(\frac{2(D + \bar{\xi}_f)}{\sqrt{(D - \bar{\xi}_f)^2 + 4\Delta^2} - D + \bar{\xi}_f} \right). \end{aligned} \quad (2.3.11)$$

In the last equation above, we assumed $D \gg \Delta$. Solving Eq.(2.3.11)

$$\Delta = \bar{D} e^{-\frac{1}{2\lambda}} \left[1 + r e^{-\frac{1}{\lambda}} \right]^{1/2}, \quad (2.3.12)$$

where $\bar{D} = \sqrt{D^2 - \bar{\xi}_f^2}$, and $r = (D + \bar{\xi}_f)/(D - \bar{\xi}_f)$. In the weak coupling limit $\lambda \rightarrow 0$, we get $\Delta \rightarrow \bar{D} e^{-\frac{1}{2\lambda}}$ (notice the factor of 2λ in the exponent) while in the strong coupling limit, we obtain the BCS-type formalism of $\Delta \rightarrow \sqrt{D^2 + \bar{\xi}_f^2} e^{-\frac{1}{\lambda}} \approx D e^{-\frac{1}{\lambda}}$.

2.3.3 Numerical solution of SC gap and transition temperature

In the case of onsite hybridization $v_{\mathbf{k}} = v$, the \mathbf{k} -dependence of the pairing potential is removed. This gives $V_{\mathbf{k}\mathbf{k}'} = -\frac{2|v|^2}{\omega_e}$ with $\omega_e > 0$, leading to a ‘conventional’ s -wave pairing symmetry $\Delta_{\mathbf{k}} = \Delta$. Taking advantage of the onsite attractive potential,

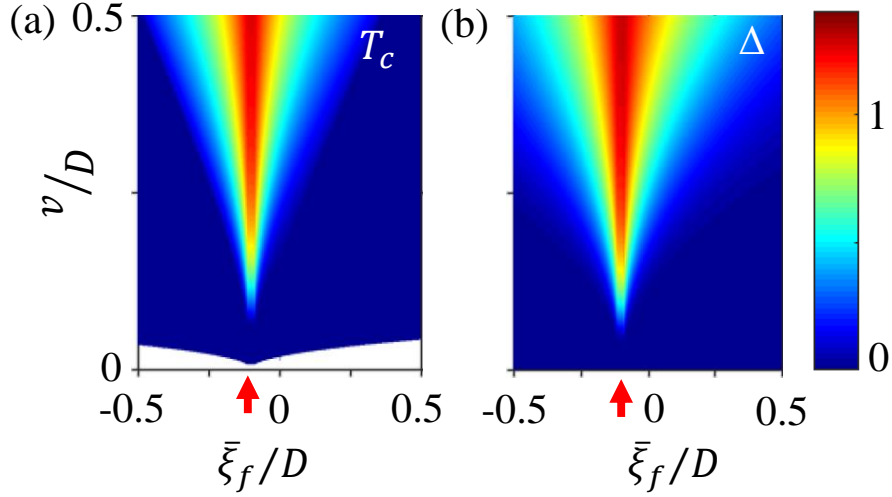


Figure 2.3: SC phase diagram with respect to valence fluctuation potential v and renormalized f -electron's energy $\bar{\xi}_f$. (a), The SC transition temperature T_c is plotted in the $v - \bar{\xi}_f$ space, scaled with respect to the conduction electron's bandwidth D . We set $\xi_f/D = -0.1$. The white region for small values of v gives the SC-forbidden region (Eq. (2.3.15)). (b), SC gap amplitude Δ (at $T = 0$) plotted in the same parameter space. Above the critical value of v , both T_c and Δ grows with v^2 as in Eq. (2.3.13). Interestingly, optimal superconductivity commences at a finite value of $\bar{\xi}_f$ where all the holon boson fields condense to $\omega_e \rightarrow 0$, and the pairing potential $V \rightarrow \infty$.

and s -wave pairing channel, we can solve Eq. (2.3.6) analytically. Solutions of Eq. (2.3.6) in the two asymptotic limits of $T \rightarrow 0$, and $\Delta \rightarrow 0$ yield the gap amplitude Δ and T_c as

$$\begin{aligned}\Delta &= \bar{D}e^{-\frac{1}{2\lambda}} \left[1 + re^{-\frac{1}{\lambda}}\right]^{1/2}, \\ k_B T_c &= D_\gamma e^{-\frac{1}{\lambda}} \left[1 - \left(\frac{\bar{\xi}_f}{2D_\gamma}\right)^2 e^{\frac{2}{\lambda}}\right]^{1/2},\end{aligned}\quad (2.3.13)$$

where $\bar{D} = \sqrt{D^2 - \bar{\xi}_f^2}$, $D_\gamma = 2D\gamma/\pi$ and $r = (D + \bar{\xi}_f)/(D - \bar{\xi}_f)$, with γ being the Euler constant, and $D = 1/2N$, and N are bandwidth and DOS of conduction electrons at the Fermi level. [We obtain above \$T_c\$ relation from Eq.\(2.3.10\).](#)

The SC coupling constant is defined as

$$\lambda = \frac{2N|v|^2}{\omega_e} = 2|\eta|^{-1}N J_K, \quad (2.3.14)$$

where $J_K = |v|^2/|\xi_f|$ is the Kondo coupling constant. η is defined below Eq. (2.2.1). The first terms before the parenthesis in both Δ and T_c are the usual BCS solutions, while the correction terms within the parenthesis have important consequences. The correction term in Eq. (2.3.13) suggests that superconductivity arises above a critical value of the coupling constant

$$\frac{1}{\lambda} < \ln\left(\frac{2D_\gamma}{|\bar{\xi}_f|}\right). \quad (2.3.15)$$

This implies that there exists a lower critical value of the hybridization v_c above which superconductivity is possible. Since v is related to the coherence temperature T_K , we show below that the above constraint translates into a lower limit for T_K to produce superconductivity. This result is in contrast to the BCS result where any infinitesimal electron-phonon coupling is sufficient for finite T_c . Interestingly, the BCS ratio $\Delta/k_B T_c$ is not a universal constant here, even in the weak coupling limit. In the limit of $D \gg \bar{\xi}_f$, we recover BCS-type behavior of $\Delta \rightarrow D e^{-1/2\lambda}$, and $k_B T_c \rightarrow D_\gamma e^{-1/\lambda}$, with $\Delta/k_B T_c \rightarrow 1.73 e^{1/2\lambda}$, suggesting a strong coupling limit of the superconductivity.

Plots of Δ and T_c as a function of v and $\bar{\xi}_f$ are shown in Fig. 2.3. Both phase

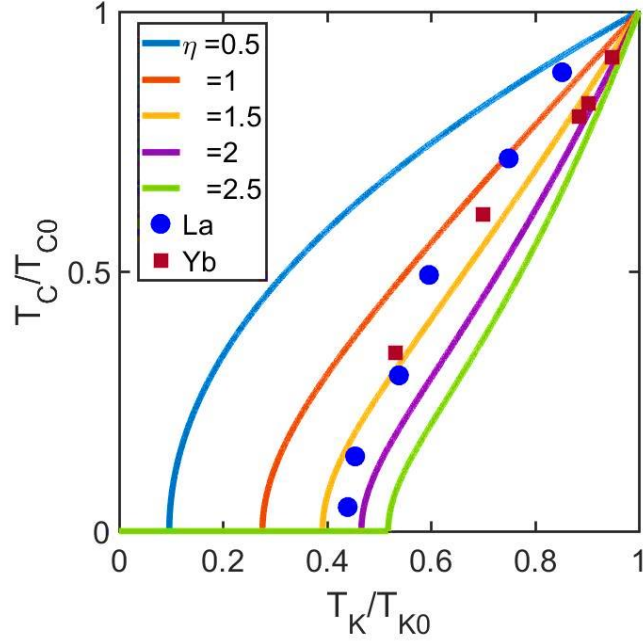


Figure 2.4: Relationship between T_c and T_K . We demonstrate the relationship between T_c and T_K for several values of the exponent η (from Eq. (2.3.17)). Interestingly, T_c vanishes below some critical value of T_K , where the cutoff value decreases with decreasing η . T_c , T_K are normalized to some highest values of T_{c0} , T_{K0} , respectively, for each values of η . For CeCoIn₅, Yb and La dopings[116] are known to modulate the valence fluctuation strength T_K , giving an intriguingly similar T_c versus T_K relationship, as predicted by our theory in Eq. (2.3.17). Experimental values agree well for $\eta \sim 1 - 1.5$ for $\xi_f = 0.7\text{eV}$.

diagrams exhibit funnel like behavior in the $v - \bar{\xi}_f$ space. We highlight here two key features. (i) In T_c plot we find a white region for small values v which marks the forbidden (non-SC) region dictated by the constraint $1/v^2 > (N/2\omega_e) \ln |2D_\gamma/\bar{\xi}_f|$ (Eq. (2.3.15)). In the rest of the regions where both Δ and T_c are finite, we obtain a second order phase transition with the critical exponent of $1/2$. (ii) Secondly, superconductivity is optimal at a characteristic value of $\bar{\xi}_f \neq 0$ (marked by arrows in Fig. 2.3). At this point $\omega_e \rightarrow 0$ ($\bar{\xi}_f = \xi_f$) and hence the pairing potential $V \rightarrow \infty$, stipulating maximum superconductivity. At the optimal T_c , f -electron's band renormalization $Z \rightarrow 1$.

2.3.4 Connection to coherence temperature T_K .

From Eq. (2.2.18), it is evident that ω_e is analogous to the Debye frequency of the electron-phonon mechanism. The essential dependence of T_c and λ on observable parameters such as coherence temperature T_K can be derived using the saddle point approximation [117, 118, 46]. For this case, Eq. (2.2.1) can be solved exactly,[45] yielding $k_B T_K = D e^{-1/N J_K}$. Therefore, from Eq. (2.3.14), we find that the SC coupling constant λ depends on T_K as

$$\frac{1}{\lambda} = \eta \ln \left(\frac{D}{k_B T_K} \right). \quad (2.3.16)$$

This result is consistent with the fact that the Kondo critical point prompts optimal superconductivity as obtained in CeCu₂Si₂,[112] as well as in many other HF superconductors.[85, 86, 2, 119, 120, 121] However, T_c is terminated below a critical T_K which can be obtained from Eq. (2.3.13) as

$$(k_B T_c)^2 = D_\gamma^2 \left(\frac{k_B T_K}{D} \right)^{2|\eta|} - \frac{\bar{\xi}_f^2}{4}, \quad (2.3.17)$$

where η is the same as before. Eq. (2.3.17) is another important result of our theory, which finds a surprisingly consistent agreement with experimental data (see Fig. 2.4). We plot T_c and T_K for several parameter values in Fig. 2.4. Both the critical behavior and the power-law dependence between T_c and T_K agree remarkably well with the experimental data of La, and Yb doped CeCoIn₅ samples.[116]

2.4 Signatures of pairing structure.

2.4.1 Pair susceptibility

To affirm that there exists a pairing instability in Eq. (2.2.17) in the main text, we compute the pair-pair correlation function. We consider the pair field

$$b_{\mathbf{k}}(\tau) = \sum_{\sigma, m} c_{\mathbf{k}\sigma}(\tau) \bar{f}_m(\tau), \quad (2.4.1)$$

where τ is the imaginary time. The pair susceptibility is defined as

$$\chi_p(\mathbf{q}, i\omega_n) = \int_0^\beta \sum_{\mathbf{k}} \left\langle \mathcal{T}_\tau b_{\mathbf{k}}(\tau) b_{\mathbf{k}+\mathbf{q}}^\dagger(\tau') \right\rangle e^{-i\omega_n(\tau-\tau')}, \quad (2.4.2)$$

Where \mathcal{T}_τ is the time ordered operator. Using Wick's decomposition, we evaluate the above average as

$$\left\langle \mathcal{T}_\tau b_{\mathbf{k}}(\tau) b_{\mathbf{k}+\mathbf{q}}^\dagger(\tau') \right\rangle = \sum_{\sigma, m} \mathcal{G}_m^f(\tau - \tau') \mathcal{G}_{\mathbf{k}, \sigma}^c(\tau - \tau') \delta_{\mathbf{q}, 0}, \quad (2.4.3)$$

where $\mathcal{G}_{\mathbf{k}, \sigma}^c(\tau - \tau') = \langle \mathcal{T}_\tau c_{\mathbf{k}\sigma}(\tau) c_{\mathbf{k}\sigma}^\dagger(\tau') \rangle$ is the conduction electron's Green's function, and $\mathcal{G}_m^f(\tau - \tau') = \langle \mathcal{T}_\tau \bar{f}_m(\tau) \bar{f}_m^\dagger(\tau') \rangle$ is the Green's function for the single site \bar{f}_m states. In the fermionic Matsubara frequency ip_n space these two Green's functions become $\mathcal{G}_{\mathbf{k}, \sigma}^c(ip_n) = (ip_n - \xi_{\mathbf{k}})^{-1}$, and $\mathcal{G}_m^f(ip_n) = (ip_n - \bar{\xi}_f)^{-1}$. Substituting the Green's functions in Eq. (2.4.2), and doing the Fourier transformation we get

$$\chi_p(i\omega_n) = \frac{1}{\beta} \sum_{\mathbf{k}, \sigma, m} \sum_{n'} \mathcal{G}_m^f(ip_{n'}) \mathcal{G}_{\mathbf{k}, \sigma}^c(i\omega_n - ip_{n'}). \quad (2.4.4)$$

Substituting the corresponding Green's functions and performing the standard Matsubara frequency summation on $ip_{n'}$, we arrive at

$$\chi_p(i\omega_n) = \sum_{\mathbf{k}} \frac{1 - f(\bar{\xi}_f) - f(\xi_{\mathbf{k}})}{\bar{\xi}_f + \xi_{\mathbf{k}} - i\omega_n}, \quad (2.4.5)$$

$f(\xi)$ is the Fermi distribution function. We are interested in the $\omega \rightarrow 0$, and $\mathbf{q} \rightarrow 0$ limits. Taking analytic continuation to the real frequency plane $i\omega_n \rightarrow \omega + i\delta$, the pair susceptibility becomes

$$\chi_p(\omega \approx 0) = \frac{N}{2} \int_{-D}^D d\xi \frac{\tanh(\frac{\beta \bar{\xi}_f}{2}) + \tanh(\frac{\beta \xi}{2})}{\bar{\xi}_f + \xi}. \quad (2.4.6)$$

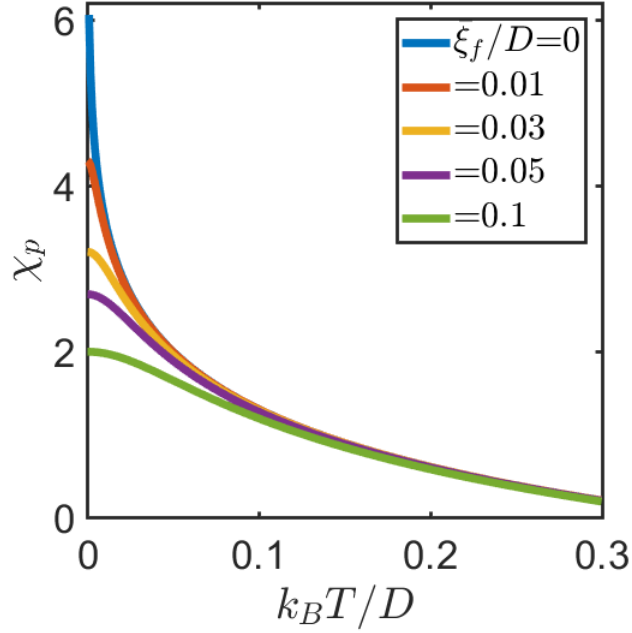


Figure 2.5: Static pair susceptibility at $\mathbf{q} = 0$ as a function of temperature for different values of $\bar{\xi}_f$. As expected from Eq. (2.4.7) the pair correlation function diverges at $T \rightarrow 0$ for $\bar{\xi}_f \rightarrow 0$.

This equation is nothing but the R.H.S. of Eq. (2.3.7), except the constant factor V . Again in the limit of $D \gg \bar{\xi}_f$ this integral gives the solution as in Eq. (2.3.8). Hence we get

$$\chi_p(T) = N \ln \left[\frac{2D\gamma}{\sqrt{\bar{\xi}_f^2 + (2k_B T)^2}} \right]. \quad (2.4.7)$$

Interestingly, unlike the typical BCS case, the pair correlation function does not have a logarithmic divergence as $T \rightarrow 0$ except in the limit of $\bar{\xi}_f \rightarrow 0$. This is the reason superconductivity is limited by a minimum limit of the coupling constant λ and T_K to overcome the onsite energy $\bar{\xi}_f$ as discussed in the main text.

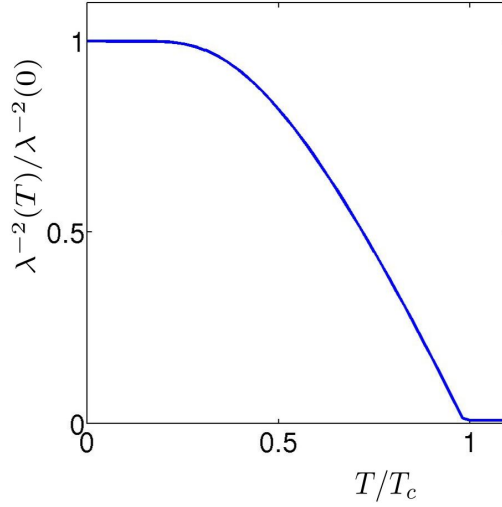


Figure 2.6: Computed superfluid density as a function of temperature. The temperature dependence shows a typical exponential behavior at low- T as seen in CeCu_2Si_2 .

2.4.2 Meissner effect

Unlike the typical Cooper pair of two conduction electrons with opposite momenta in other types of superconductors, here we have a pairing between conduction electron and correlated singly occupied f -electrons. The conduction electrons directly couple to the gauge field \mathbf{A} as $\mathbf{p}' = \hbar\mathbf{k} - \frac{e}{c}\mathbf{A}$. On the other hand, the f -states do not couple to the vector potential in its localized limit. Importantly, despite that the magnetic field couples only to the conduction electron, we find a complete exclusion of the magnetic field at $T \rightarrow 0$, a hallmark of superfluid state. Interestingly, however, in the strongly localized limit of the f -orbitals, the Meissner effect experiments will exhibit charge of the Cooper pair to be $-e$, instead of $-2e$ as in other Conventional Cooper pair between two itinerant electrons. Caution to be taken in realistic HF systems, where the band structure calculation[122] shows weak dispersion of the f -electrons, which couple to the external gauge field, and hence may contribute to the Cooper pair charge of $-2e$ or a value between $-e$ to $-2e$ on average.

How do these Cooper pairs couple to the applied magnetic field? It is easy to envisage that conduction electrons directly couple to the gauge field \mathbf{A} as $\mathbf{p}' = \hbar\mathbf{k} - \frac{e}{c}\mathbf{A}$.

On the other hand, the f -states do not couple to the vector potential in its localized limit. Therefore, important changes are expected here, in the Meissner effects, compared to typical BCS case.

Under the magnetic field the BdG states become chiral and thus the Bogolyubov states $\phi_{\pm\mathbf{k}}^{\pm}$ and the corresponding eigenvalues $E_{\pm\mathbf{k}}^{\pm}$ for $\pm\mathbf{k}$ are no longer the same. Hence we treat them explicitly as:

$$c_{\mathbf{k}\uparrow} = \alpha_{\mathbf{k}}\phi_{\mathbf{k}+} + \beta_{\mathbf{k}}\phi_{\mathbf{k}-}^{\dagger}, \quad (2.4.8)$$

$$c_{-\mathbf{k}\downarrow} = \alpha_{\mathbf{k}}\phi_{\mathbf{k}-} + \beta_{\mathbf{k}}\phi_{\mathbf{k}+}^{\dagger}, \quad (2.4.9)$$

$\alpha_{\mathbf{k}}$, and $\beta_{\mathbf{k}}$ are the coherence factors at zero magnetic field.

$$c_{\mathbf{k}\uparrow}^{\dagger}c_{\mathbf{k}\uparrow} = \alpha_{\mathbf{k}}^2\phi_{\mathbf{k}+}^{\dagger}\phi_{\mathbf{k}+} - \beta_{\mathbf{k}}^2\phi_{\mathbf{k}-}^{\dagger}\phi_{\mathbf{k}-} + \beta_{\mathbf{k}}^2 + \alpha_{\mathbf{k}}\beta_{\mathbf{k}}\left(\phi_{\mathbf{k}+}^{\dagger}\phi_{\mathbf{k}-}^{\dagger} - \phi_{\mathbf{k}+}\phi_{\mathbf{k}-}\right), \quad (2.4.10)$$

$$c_{-\mathbf{k}\downarrow}^{\dagger}c_{-\mathbf{k}\downarrow} = \alpha_{\mathbf{k}}^2\phi_{\mathbf{k}-}^{\dagger}\phi_{\mathbf{k}-} - \beta_{\mathbf{k}}^2\phi_{\mathbf{k}+}^{\dagger}\phi_{\mathbf{k}+} + \beta_{\mathbf{k}}^2 + \alpha_{\mathbf{k}}\beta_{\mathbf{k}}\left(-\phi_{\mathbf{k}+}^{\dagger}\phi_{\mathbf{k}-}^{\dagger} + \phi_{\mathbf{k}+}\phi_{\mathbf{k}-}\right). \quad (2.4.11)$$

Subtracting Eq. (2.4.10) and Eq.(2.4.11)

$$c_{\mathbf{k}\uparrow}^{\dagger}c_{\mathbf{k}\uparrow} - c_{-\mathbf{k}\downarrow}^{\dagger}c_{-\mathbf{k}\downarrow} = \phi_{\mathbf{k}+}^{\dagger}\phi_{\mathbf{k}+} - \phi_{\mathbf{k}-}^{\dagger}\phi_{\mathbf{k}-} + 2\alpha_{\mathbf{k}}\beta_{\mathbf{k}}\left(\phi_{\mathbf{k}+}^{\dagger}\phi_{\mathbf{k}-}^{\dagger} - \phi_{\mathbf{k}+}\phi_{\mathbf{k}-}\right).$$

Adding Eq. (2.4.10) and Eq.(2.4.11)

$$\begin{aligned} c_{\mathbf{k}\uparrow}^{\dagger}c_{\mathbf{k}\uparrow} + c_{-\mathbf{k}\downarrow}^{\dagger}c_{-\mathbf{k}\downarrow} &= \phi_{\mathbf{k}+}^{\dagger}\phi_{\mathbf{k}+}(\alpha_{\mathbf{k}}^2 - \beta_{\mathbf{k}}^2) + \phi_{\mathbf{k}-}^{\dagger}\phi_{\mathbf{k}-}(\alpha_{\mathbf{k}}^2 - \beta_{\mathbf{k}}^2) + 2\beta_{\mathbf{k}}^2, \\ &= (\alpha_{\mathbf{k}}^2 - \beta_{\mathbf{k}}^2)(\phi_{\mathbf{k}+}^{\dagger}\phi_{\mathbf{k}+} + \phi_{\mathbf{k}-}^{\dagger}\phi_{\mathbf{k}-}) + 2\beta_{\mathbf{k}}^2. \end{aligned} \quad (2.4.12)$$

We proceed with computation of the diamagnetic (\mathbf{J}_d) and paramagnetic (\mathbf{J}_p) current of the conduction electrons only. The two current operators are

$$\mathbf{J}_d(\mathbf{q}) = \frac{e^2}{c}\mathbf{a}(\mathbf{q})\sum_{\mathbf{k}\sigma}^{\prime}\frac{1}{m_{\mathbf{k}}}\left[c_{\mathbf{k}-\mathbf{q}\sigma}^{\dagger}c_{\mathbf{k}\sigma} + c_{-\mathbf{k}+\mathbf{q}\sigma}^{\dagger}c_{-\mathbf{k}\sigma}\right], \quad (2.4.13)$$

$$\mathbf{J}_p(\mathbf{q}) = e\sum_{\mathbf{k}\sigma}^{\prime}\mathbf{v}_{\mathbf{k}-\mathbf{q}}\left[c_{\mathbf{k}-\mathbf{q}\sigma}^{\dagger}c_{\mathbf{k}\sigma} - c_{-\mathbf{k}+\mathbf{q}\sigma}^{\dagger}c_{-\mathbf{k}\sigma}\right]. \quad (2.4.14)$$

$\mathbf{v}_{\mathbf{k}}$ and $m_{\mathbf{k}}$ are the velocity and effective mass, respectively, of the conduction electron, and \mathbf{a} is the Fourier component of the vector potential \mathbf{A} . In the above two equations we utilized the fact that $\mathbf{v}_{-\mathbf{k}} = -\mathbf{v}_{\mathbf{k}}$, and $m_{-\mathbf{k}} = m_{\mathbf{k}}$. The prime over the summation indicate that the summation is restricted to the first quadrant of the BZ. From Eq. (2.4.14) we get

$$\begin{aligned} \mathbf{J}_p(0) &= e \sum_{\mathbf{k}} \hbar \mathbf{k} (c_{\mathbf{k}\uparrow}^\dagger c_{\mathbf{k}\uparrow} - c_{-\mathbf{k}\downarrow}^\dagger c_{-\mathbf{k}\downarrow}), \\ &= e \sum_{\mathbf{k}} \hbar \mathbf{k} \left[\phi_{\mathbf{k}+}^\dagger \phi_{\mathbf{k}+} - \phi_{\mathbf{k}-}^\dagger \phi_{\mathbf{k}-} + 2\alpha_{\mathbf{k}}\beta_{\mathbf{k}} \left(\phi_{\mathbf{k}+}^\dagger \phi_{\mathbf{k}-}^\dagger - \phi_{\mathbf{k}+} \phi_{\mathbf{k}-} \right) \right]. \end{aligned} \quad (2.4.15)$$

Average paramagnetic current is

$$\langle \mathbf{J}_p(0) \rangle = e \sum_{\mathbf{k}} \hbar \mathbf{k} (f(E_{\mathbf{k}}^1) - f(E_{\mathbf{k}}^2)). \quad (2.4.16)$$

Similarly diamagnetic current we calculate from Eq. (2.4.13)

$$\begin{aligned} \mathbf{J}_d(0) &= -\frac{e^2}{mc} \mathbf{a}(0) \sum_{\mathbf{k}} (c_{\mathbf{k}\uparrow}^\dagger c_{\mathbf{k}\uparrow} + c_{-\mathbf{k}\downarrow}^\dagger c_{-\mathbf{k}\downarrow}), \\ &= -\frac{(e)^2}{mc} \mathbf{a}(0) \sum_{\mathbf{k}} \left((\alpha_{\mathbf{k}}^2 - \beta_{\mathbf{k}}^2) (\phi_{\mathbf{k}+}^\dagger \phi_{\mathbf{k}+} + \phi_{\mathbf{k}-}^\dagger \phi_{\mathbf{k}-}) + 2\beta_{\mathbf{k}}^2 \right). \end{aligned} \quad (2.4.17)$$

Average diamagnetic current is given as,

$$\langle \mathbf{J}_d(0) \rangle = -\frac{(e)^2}{mc} \mathbf{a}(0) \sum_{\mathbf{k}} \left((\alpha_{\mathbf{k}}^2 - \beta_{\mathbf{k}}^2) (f(E_{\mathbf{k}}^1) + f(E_{\mathbf{k}}^2)) + 2\beta_{\mathbf{k}}^2 \right). \quad (2.4.18)$$

The corresponding change in the eigenvalue are $E_{\pm\mathbf{k}}^\nu = E_{\mathbf{k}}^\nu \mp \frac{e}{c} \mathbf{a} \cdot \mathbf{v}_{\mathbf{k}}$, where $\nu = \pm$, and \mathbf{a} is the Fourier component of the vector potential in the momentum space. We discuss it below.

Effective Hamiltonian after BdG diagonalization is

$$H_{eff} = \sum_{\mathbf{k}} \left(E_{\mathbf{k}}^+ \phi_{\mathbf{k}+}^\dagger \phi_{\mathbf{k}+} + E_{\mathbf{k}}^- \phi_{\mathbf{k}-} \phi_{\mathbf{k}-}^\dagger \right). \quad (2.4.19)$$

We add external perturbation to Hamiltonian Eq. (2.4.19),

$$\begin{aligned} \tilde{H} &= -\frac{\hbar e}{c} \sum_{\mathbf{k}\sigma} \mathbf{a}(0) \cdot \mathbf{v}_{\mathbf{k}} c_{\mathbf{k}\sigma}^\dagger c_{\mathbf{k}\sigma}, \\ &= -\frac{\hbar e}{c} \sum_{\mathbf{k}} \mathbf{a}(0) \cdot \mathbf{v}_{\mathbf{k}} (\phi_{\mathbf{k}+}^\dagger \phi_{\mathbf{k}+} - \phi_{\mathbf{k}-}^\dagger \phi_{\mathbf{k}-}). \end{aligned} \quad (2.4.20)$$

Now BdG eigenvalues are,

$$\begin{aligned} E_{\mathbf{k}}^1 &= E_{\mathbf{k}}^+ - \frac{\hbar e}{c} \mathbf{a}(0) \cdot \mathbf{v}_{\mathbf{k}}, \\ E_{\mathbf{k}}^2 &= -E_{\mathbf{k}}^- + \frac{\hbar e}{c} \mathbf{a}(0) \cdot \mathbf{v}_{\mathbf{k}}, \end{aligned} \quad (2.4.21)$$

$\mathbf{v}_{\mathbf{k}} = \partial \xi_{\mathbf{k}} / (\hbar \partial \mathbf{k})$ is the conduction band velocity with $\mathbf{v}_{-\mathbf{k}} = -\mathbf{v}_{\mathbf{k}}$. $E_{\mathbf{k}}^\nu$ are the eigenvalues without the magnetic field, and hence $E_{-\mathbf{k}}^\nu = E_{\mathbf{k}}^\nu$.

In the weak magnetic field limit, this corresponds to the change in the Fermi-Dirac distribution functions as,

$$f(E_{\mathbf{k}}^1) = f(E_{\mathbf{k}}^+) - \left(\frac{\hbar e}{c} \mathbf{a}(0) \cdot \mathbf{v}_{\mathbf{k}} \right) \frac{\partial f(E_{\mathbf{k}}^+)}{\partial E_{\mathbf{k}}^+}, \quad (2.4.22)$$

$$f(E_{\mathbf{k}}^2) = f(-E_{\mathbf{k}}^-) - \left(\frac{\hbar e}{c} \mathbf{a}(0) \cdot \mathbf{v}_{\mathbf{k}} \right) \frac{\partial f(-E_{\mathbf{k}}^-)}{\partial E_{\mathbf{k}}^-}. \quad (2.4.23)$$

Adding Eq. (2.4.22) and Eq. (2.4.23) we obtain,

$$\begin{aligned} f(E_{\mathbf{k}}^1) + f(E_{\mathbf{k}}^2) &= f(E_{\mathbf{k}}^+) + f(-E_{\mathbf{k}}^-) - \left(\frac{\hbar e}{c} \mathbf{a}(0) \cdot \mathbf{v}_{\mathbf{k}} \right) \left[\frac{\partial f(E_{\mathbf{k}}^+)}{\partial E_{\mathbf{k}}^+} + \frac{\partial f(-E_{\mathbf{k}}^-)}{\partial E_{\mathbf{k}}^-} \right], \\ &= 1 - \frac{\left(\tanh\left(\frac{\beta E_{\mathbf{k}}^+}{2}\right) - \tanh\left(\frac{\beta E_{\mathbf{k}}^-}{2}\right) \right)}{2} \\ &\quad - \left(\frac{\hbar e}{c} \mathbf{a}(0) \cdot \mathbf{v}_{\mathbf{k}} \right) \left[-\operatorname{sech}^2\left(\frac{\beta E_{\mathbf{k}}^+}{2}\right) + \operatorname{sech}^2\left(\frac{\beta E_{\mathbf{k}}^-}{2}\right) \right]. \end{aligned} \quad (2.4.24)$$

Paramagnetic current is given by Eq. (2.4.15)

$$\langle \mathbf{J}_p(0) \rangle = \hbar e \sum_{\mathbf{k}} \mathbf{k} \left[-\frac{1}{2} \left(\tanh\left(\frac{\beta E_{\mathbf{k}}^+}{2}\right) + \tanh\left(\frac{\beta E_{\mathbf{k}}^-}{2}\right) \right) + \left(\frac{\hbar e \beta}{4c} \mathbf{a}(0) \cdot \mathbf{v}_{\mathbf{k}} \right) \left(\operatorname{sech}^2\left(\frac{\beta E_{\mathbf{k}}^+}{2}\right) + \operatorname{sech}^2\left(\frac{\beta E_{\mathbf{k}}^-}{2}\right) \right) \right]. \quad (2.4.25)$$

Similarly diamagnetic current is given by Eq. (2.4.18)

$$\langle \mathbf{J}_d(0) \rangle = -\frac{(e)^2}{mc} \mathbf{a}(0) \sum_{\mathbf{k}} \left[2\beta_{\mathbf{k}}^2 + (\alpha_{\mathbf{k}}^2 - \beta_{\mathbf{k}}^2) \left\{ 1 - \frac{\left(\tanh\left(\frac{\beta E_{\mathbf{k}}^+}{2}\right) - \tanh\left(\frac{\beta E_{\mathbf{k}}^-}{2}\right) \right)}{2} - \frac{\hbar e}{c} \mathbf{a}(0) \cdot \mathbf{v}_{\mathbf{k}} \left(-\operatorname{sech}^2\left(\frac{\beta E_{\mathbf{k}}^+}{2}\right) + \operatorname{sech}^2\left(\frac{\beta E_{\mathbf{k}}^-}{2}\right) \right) \right\} \right]. \quad (2.4.26)$$

Next we take the linear response theory and within the London's equations, we define the penetration depth $\lambda(T)$ as $\lambda_{ij}^{-2} = -\frac{4\pi}{c} \frac{J_i(0)}{a_j(0)}$, where $\mathbf{J} = \mathbf{J}_p + \mathbf{J}_d$ is the total current. i, j are the spatial coordinates. This gives the final result given in Eq. (2.4.27). This equation reduces to the typical BCS form in the case of $\xi_{\mathbf{k}} = -\bar{\xi}_f$.

Using the mean-field solution of the quasiparticle bands, the superfluid density (inversely proportional to the magnetic penetration depth) is obtained to be

$$\lambda_{ij}^{-2}(T) = \frac{4\pi e^2}{c^2} \sum_{\mathbf{k}}' \left[\frac{1}{m_{ij,\mathbf{k}}} \left(1 - \sum_{\nu} (\alpha_{\mathbf{k}}^{\nu})^2 \tanh\left(\frac{\beta E_{\mathbf{k}}^{\nu}}{2}\right) \right) - \frac{\beta}{2} v_{i\mathbf{k}} v_{j\mathbf{k}} \sum_{\nu} (\alpha_{\mathbf{k}}^{\nu})^2 \operatorname{sech}^2\left(\frac{\beta E_{\mathbf{k}}^{\nu}}{2}\right) \right]. \quad (2.4.27)$$

$\nu = \pm$ for two quasiparticle bands. [Prime symbol over the summation indicates that it is restricted within the first quadrant of the BZ, since both $+\mathbf{k}$ and $-\mathbf{k}$ fermions are included exclusively to obtain Eq. (2.4.18), (2.4.15).] $(\alpha_{\mathbf{k}}^{\mp})^2 = \frac{1}{2} \left(1 \mp \frac{\xi_{\mathbf{k}}^+}{E_{0\mathbf{k}}} \right)$ is the coherence factors of the mean-field solutions. The numerical evaluation

of Eq. 2.4.27 yields an exponential behavior of superfluid density as $T \rightarrow 0$, as shown in Fig. 2.6. This behavior is also observed experimentally in CeCu₂Si₂ [109, 110] as well as in Yb-doped CeCoIn₅[114].

2.4.3 Spin-resonance mode

For unconventional pairing symmetry, the sign-reversal of the SC gap leads to a spin-resonance mode at $\omega_{\text{res}} \leq 2\Delta$. [4] Such a mode is rather weak in intensity and may lie above 2Δ for conventional (fixed sign) pairing symmetry. [123] Experimentally, a resonance is observed in the SC state in CeCu₂Si₂ at $\mathbf{Q} \sim (0.215, 0.215, 1.458)$ in r.l.u. in the energy scale of ~ 0.2 meV which is roughly at $4k_B T_c$ ($T_c \sim 0.6$ K). [104]

The present pairing symmetry has few interesting collective spin modes which can explain the above experimental behavior. For the calculation of spin fluctuation to be tractable we consider that the f -electrons possess spin $m = \pm 1/2$.

Nambu spinor is given by $\psi = (c_{\mathbf{k}\uparrow}, \bar{f}_{\downarrow}^{\dagger}, c_{\mathbf{k}\downarrow}^{\dagger}, \bar{f}_{\uparrow})^T$. Hamiltonian in the basis can be written as

$$H_{4 \times 4}(\mathbf{k}) = \psi^{\dagger} \tilde{H}(\mathbf{k}) \psi, \quad (2.4.28)$$

where

$$\tilde{H}(\mathbf{k}) = \begin{pmatrix} H_{\text{MF}}(\mathbf{k}) & \tilde{0} \\ \tilde{0} & -H_{\text{MF}}(\mathbf{k}) \end{pmatrix}. \quad (2.4.29)$$

$H_{\text{MF}}(\mathbf{k})$ is defined in Eq. (2.3.1), $\tilde{0}$ is a 2×2 null matrix.

Superconducting Green's function is $\mathcal{G}(\mathbf{k}, \tau - \tau') = -\langle T_{\tau} \psi(\tau) \psi^{\dagger}(\tau') \rangle$,

$$\mathcal{G}(\mathbf{k}, \tau - \tau') = \begin{pmatrix} \mathcal{G}^{11}(\mathbf{k}, \tau - \tau') & \tilde{0} \\ \tilde{0} & \mathcal{G}^{22}(\mathbf{k}, \tau - \tau') \end{pmatrix}, \quad (2.4.30)$$

where,

$$\mathcal{G}^{11}(\mathbf{k}, \tau - \tau') = \begin{pmatrix} \mathcal{G}_{\uparrow}^c(\mathbf{k}, \tau - \tau') & \mathcal{F}^1(\mathbf{k}, \tau - \tau') \\ \mathcal{F}^{1\dagger}(\mathbf{k}, \tau - \tau') & \mathcal{G}_{\downarrow}^{f\dagger}(\mathbf{k}, \tau - \tau') \end{pmatrix}, \quad (2.4.31)$$

$$\mathcal{G}^{22}(\mathbf{k}, \tau - \tau') = \begin{pmatrix} \mathcal{G}_{\downarrow}^{c\dagger}(\mathbf{k}, \tau - \tau') & \mathcal{F}^{2\dagger}(\mathbf{k}, \tau - \tau') \\ \mathcal{F}^2(\mathbf{k}, \tau - \tau') & \mathcal{G}_{\uparrow}^f(\mathbf{k}, \tau - \tau') \end{pmatrix}. \quad (2.4.32)$$

Anomalous Green's function is given by,

$$\mathcal{F}^1(\mathbf{k}, \tau - \tau') = -\langle T_{\tau} c_{\mathbf{k}\uparrow}(\tau) \bar{f}_{\downarrow}(\tau') \rangle, \quad (2.4.33)$$

$$\mathcal{F}^2(\mathbf{k}, \tau - \tau') = -\langle T_{\tau} \bar{f}_{\uparrow}(\tau) c_{\mathbf{k}\downarrow}(\tau') \rangle. \quad (2.4.34)$$

Fourier transform of Eq. (2.4.30) is,

$$\begin{aligned} \mathcal{G}(\mathbf{k}, ik_n) &= \frac{1}{ik_n I - \tilde{H}(\mathbf{k})}, \\ &= \begin{pmatrix} \mathcal{G}^{11}(\mathbf{k}, ik_n) & \tilde{0} \\ \tilde{0} & \mathcal{G}^{22}(\mathbf{k}, ik_n) \end{pmatrix}. \end{aligned} \quad (2.4.35)$$

The matrix elements are,

$$\begin{aligned} \mathcal{G}^{11}(\mathbf{k}, ik_n) &= \frac{1}{(ik_n + \bar{\xi}_f)(ik_n - \xi_{\mathbf{k}}) - \Delta_{\mathbf{k}}^2} \begin{pmatrix} ik_n + \bar{\xi}_f & -\Delta_{\mathbf{k}} \\ -\Delta_{\mathbf{k}} & ik_n - \xi_{\mathbf{k}} \end{pmatrix}, \\ \mathcal{G}^{22}(\mathbf{k}, ik_n) &= \frac{1}{(ik_n - \bar{\xi}_f)(ik_n + \xi_{\mathbf{k}}) - \Delta_{\mathbf{k}}^2} \begin{pmatrix} ik_n - \bar{\xi}_f & \Delta_{\mathbf{k}} \\ \Delta_{\mathbf{k}} & ik_n + \xi_{\mathbf{k}} \end{pmatrix}. \end{aligned} \quad (2.4.36)$$

The matrix elements are related via,

$$\mathcal{G}^{22}(\mathbf{k}, ik_n) = -\mathcal{G}^{11}(\mathbf{k}, -ik_n), \quad \mathcal{G}^{22}(\mathbf{k}, \tau - \tau') = -\mathcal{G}^{11}(\mathbf{k}, \tau' - \tau). \quad (2.4.37)$$

The anomalous Green's functions are,

$$\begin{aligned}\mathcal{F}^1(\mathbf{k}, ik_n) &= -\frac{\Delta_{\mathbf{k}}}{(ik_n + \bar{\xi}_f)(ik_n - \xi_{\mathbf{k}}) - \Delta_{\mathbf{k}}^2}, \\ &= -\alpha_{\mathbf{k}}\beta_{\mathbf{k}}\left(\frac{1}{ik_n - E_{\mathbf{k}}^+} - \frac{1}{ik_n - E_{\mathbf{k}}^-}\right),\end{aligned}\quad (2.4.38)$$

$$\begin{aligned}\mathcal{F}^2(\mathbf{k}, ik_n) &= \frac{\Delta_{\mathbf{k}}}{(ik_n - \bar{\xi}_f)(ik_n + \xi_{\mathbf{k}}) - \Delta_{\mathbf{k}}^2}, \\ &= -\alpha_{\mathbf{k}}\beta_{\mathbf{k}}\left(\frac{1}{ik_n + E_{\mathbf{k}}^+} - \frac{1}{ik_n + E_{\mathbf{k}}^-}\right).\end{aligned}\quad (2.4.39)$$

From Hermiticity we have,

$$\mathcal{F}^{2\dagger}(\mathbf{k}, ik_n) = \mathcal{F}^2(\mathbf{k}, ik_n), \quad \mathcal{F}^{1\dagger}(\mathbf{k}, ik_n) = \mathcal{F}^1(\mathbf{k}, ik_n). \quad (2.4.40)$$

Finally, we obtain all Green's functions,

$$\begin{aligned}\mathcal{G}_{\uparrow}^c(\mathbf{k}, ik_n) &= \frac{ik_n + \bar{\xi}_f}{(ik_n + \bar{\xi}_f)(ik_n - \xi_{\mathbf{k}}) - \Delta_{\mathbf{k}}^2}, \\ &= \left(\frac{\alpha_{\mathbf{k}}^2}{ik_n - E_{\mathbf{k}}^+} + \frac{\beta_{\mathbf{k}}^2}{ik_n - E_{\mathbf{k}}^-}\right),\end{aligned}\quad (2.4.41)$$

$$\begin{aligned}\mathcal{G}_{\downarrow}^{c\dagger}(\mathbf{k}, ik_n) &= \frac{ik_n - \bar{\xi}_f}{(ik_n - \bar{\xi}_f)(ik_n + \xi_{\mathbf{k}}) - \Delta_{\mathbf{k}}^2}, \\ &= \left(\frac{\alpha_{\mathbf{k}}^2}{ik_n + E_{\mathbf{k}}^+} + \frac{\beta_{\mathbf{k}}^2}{ik_n + E_{\mathbf{k}}^-}\right),\end{aligned}\quad (2.4.42)$$

$$\begin{aligned}\mathcal{G}_{\uparrow}^f(ik_n) &= \sum_{\mathbf{k}} \frac{ik_n + \xi_{\mathbf{k}}}{(ik_n - \bar{\xi}_f)(ik_n + \xi_{\mathbf{k}}) - \Delta_{\mathbf{k}}^2}, \\ &= \sum_{\mathbf{k}} \left(\frac{\alpha_{\mathbf{k}}^2}{ik_n + E_{\mathbf{k}}^-} + \frac{\beta_{\mathbf{k}}^2}{ik_n + E_{\mathbf{k}}^+}\right),\end{aligned}\quad (2.4.43)$$

$$\begin{aligned}
\mathcal{G}_{\downarrow}^{f\dagger}(ik_n) &= \sum_{\mathbf{k}} \frac{ik_n - \xi_{\mathbf{k}}}{(ik_n + \bar{\xi}_f)(ik_n - \xi_{\mathbf{k}}) - \Delta_{\mathbf{k}}^2}, \\
&= \sum_{\mathbf{k}} \left(\frac{\alpha_{\mathbf{k}}^2}{ik_n - E_{\mathbf{k}}^-} + \frac{\beta_{\mathbf{k}}^2}{ik_n - E_{\mathbf{k}}^+} \right).
\end{aligned} \tag{2.4.44}$$

Transverse spin susceptibility:

In this case, the total spin operator can be defined as a summation over conduction spin and f -electrons spin:

$$\mathbf{S}_{\mathbf{q}} = \frac{1}{2} \left(\sum_{\mathbf{k}\alpha\beta} c_{\mathbf{k}\alpha}^{\dagger} \boldsymbol{\sigma}_{\alpha\beta} c_{\mathbf{k}+\mathbf{q}\beta} + \sum_{\alpha\beta} \bar{f}_{\alpha}^{\dagger} \boldsymbol{\sigma}_{\alpha\beta} \bar{f}_{\beta} \right). \tag{2.4.45}$$

$$\mathcal{S}^+(\mathbf{q}) = \sum_{\mathbf{k}} c_{\mathbf{k},\uparrow}^{\dagger} c_{\mathbf{k}+\mathbf{q},\downarrow} + \bar{f}_{\uparrow}^{\dagger} \bar{f}_{\downarrow}, \tag{2.4.46}$$

$$\mathcal{S}^-(\mathbf{q}) = \sum_{\mathbf{k}} c_{\mathbf{k},\downarrow}^{\dagger} c_{\mathbf{k}+\mathbf{q},\uparrow} + \bar{f}_{\downarrow}^{\dagger} \bar{f}_{\uparrow}, \tag{2.4.47}$$

where, α, β are spin indices. The transverse spin susceptibility is defined as $\chi(\mathbf{q}, \tau) = \langle T_{\tau} S^+(\mathbf{q}, \tau) S^-(\mathbf{q}, 0) \rangle$. Solving in the mean-field SC state, we obtain

$$\chi(\mathbf{q}, i\omega_n) = \sum_{\mathbf{k}} \sum_{\mu, \nu = \pm} A_{\mathbf{k}\mathbf{q}}^{\mu\nu} \frac{f(E_{\mathbf{k}+\mathbf{q}}^{\mu}) - f(E_{\mathbf{k}}^{\nu})}{i\omega_n + E_{\mathbf{k}}^{\nu} - E_{\mathbf{k}+\mathbf{q}}^{\mu}}, \tag{2.4.48}$$

where

$$A_{\mathbf{k}\mathbf{q}}^{\mu\nu} = \frac{1}{2} \left(1 \pm \frac{\xi_{\mathbf{k}}^+ \xi_{\mathbf{k}+\mathbf{q}}^+ + \Delta_{\mathbf{k}} \Delta_{\mathbf{k}+\mathbf{q}}}{E_{0\mathbf{k}+\mathbf{q}} E_{0\mathbf{k}}} \right), \tag{2.4.49}$$

$\mu, \nu = \pm$ are the band indices, and \pm in Eq. (2.4.49) corresponds to amplitude of the oscillators for $\mu = \nu$ (intra-) and $\mu \neq \nu$ (inter-) quasiparticle band transition. Eq. (2.4.48) can give various collective excitations, depending on the band structure details. We are here interested in the possible modes inside the SC gap. Indeed, we find the solution of a localized spin-excitation in the SC state at a wavevector which corresponds to the condition $\xi_{\mathbf{k}}^+ = -\xi_{\mathbf{k}+\mathbf{Q}}^+$. (Note that this is not the condition of the conduction electron's FS nesting). In this case, we have a resonance at an energy

Resonance condition:

If $E_{\mathbf{k}}^- < 0$ and $E_{\mathbf{k}+\mathbf{q}}^+ > 0$ so that $\chi^{+-}(\mathbf{k}, \mathbf{q}, \omega) \neq 0$. Susceptibility diverges at $\mathbf{q} = \mathbf{Q}$

$$\begin{aligned}\omega &= E_{\mathbf{k}+\mathbf{Q}}^+ - E_{\mathbf{k}}^-, \\ &= \frac{\xi_{\mathbf{k}+\mathbf{Q}} - \xi_{\mathbf{k}}}{2} + \sqrt{(\xi_{\mathbf{k}+\mathbf{Q}}^+)^2 + \Delta^2} + \sqrt{(\xi_{\mathbf{k}}^+)^2 + \Delta^2}.\end{aligned}\tag{2.4.50}$$

If at $\mathbf{q} = \mathbf{Q}$, $\xi_{\mathbf{k}}^+ = -\xi_{\mathbf{k}+\mathbf{Q}}^+$ then

$$\begin{aligned}\omega &= \omega_{\text{res}} = 2\sqrt{(\xi_{\mathbf{k}}^+)^2 + \Delta^2}, \\ &\approx \frac{2\Delta^2}{|\bar{\xi}_f|}.\end{aligned}\tag{2.4.51}$$

The coefficient is,

$$\begin{aligned}A_{k,Q}^{+-} &= \frac{1}{2}\left(1 - \frac{\Delta^2 - \xi_{\mathbf{k}}^+ \xi_{\mathbf{k}}^-}{\sqrt{((\xi_{\mathbf{k}}^-)^2 + \Delta^2)((\xi_{\mathbf{k}}^+)^2 + \Delta^2)}}\right), \\ &= \frac{1}{2}\left(1 - \frac{\Delta^2 - \frac{\xi_{\mathbf{k}}^2 - \xi_s^2}{4}}{\sqrt{((\frac{\xi_{\mathbf{k}} - \xi_s}{2})^2 + \Delta^2)((\frac{\xi_{\mathbf{k}} \xi_s}{2})^2 + \Delta^2)}}\right).\end{aligned}\tag{2.4.52}$$

The resonance frequency is given by,

$$\omega_{\text{res}} = E_{\mathbf{k}+\mathbf{Q}}^+ - E_{\mathbf{k}}^- \sim \frac{2\Delta^2}{|\bar{\xi}_f|},\tag{2.4.53}$$

we use the limit of $\Delta \gg \xi_{\mathbf{k}}^+$. The corresponding oscillator strength of the resonance mode is $A_{\mathbf{k}\mathbf{q}}^{\mu,\nu \neq \mu} = (\xi_{\mathbf{k}}^+)^2/E_{0\mathbf{k}}^2 > 0$. Since $\bar{\xi}_f > \Delta$, the resonance occurs inside the SC gap, as observed experimentally in CeCu₂Si₂[104].

2.4.4 Other measurements

The present theory of valence fluctuation mediated attractive pairing channel can be verified in multiple ways. For example, the present theory predicts a unique

Andreev reflection behavior. In a typical normal metal and superconductor interface, as an electron tunnels from the metal into the superconductor side, it reflects back a hole, and vice versa. In our present case, the conduction electron from the normal metal forms a Cooper pair with a f -state in the SC sample, and thus reflects a f -electron to the normal metal, which can be easily probed. The reflection probably is inversely proportional to the effective mass of the f -electron. This means in the limit of the localized f -electron case, the Andreev reflection can be strongly suppressed or absent. A suppression of Andreev reflection amplitude is observed in CeCoIn₅, [124] and CeCu₂Si₂ [105, 106].

As also mentioned in the above section, in the limit of fully localized f -orbitals when the coupling to the external gauge field is suppressed, one may find evidence of $-e$ charge of the Cooper pair in such experiments. However, the band structure effect of the f -orbitals can help coupling of the f -orbitals to the gauge field and hence the charge of the Cooper pair on average can be observed to be somewhere between $-e$ to $-2e$ in experiments.

2.5 Discussions and conclusions

Our theory demonstrates the existence of an attractive pairing potential mediated by the interplay between Coulomb interaction and valence fluctuations. The origin of the attractive potential is the emergent boson field (holon) associated with single-site f -states to restrict double occupancy due to strong Coulomb interaction. The effective interaction is a result of multiple valence fluctuations: The holon fields generated in a given valence fluctuation is absorbed in the second valence fluctuation, and the resulting process generates an effective interaction between the f and conduction electrons. The interaction is attractive at low-frequency and isotropic in the case of onsite valence fluctuation process. The onsite, attractive interaction naturally gives an isotropic, constant sign s -wave pairing channel between the single-site f -electrons, and conduction electrons.

Our result of fixed-sign, isotropic s -wave pairing channel is consistent with numerous experimental data discussed in the introduction. [105, 106, 107, 108, 109, 110, 111] The exponential temperature dependence of point-contact tunnel-

ing spectroscopy,[105, 106] specific heat,[107, 108, 109] thermal conductivity[109], and penetration depth[109, 110] are naturally explained within our model. Moreover, there have been several recent evidence of two-band superconductivity in CeCu_2Si_2 . [107, 108, 110]. The low-temperature specific heat [109] and tunnelling spectroscopy [105] measurement on one of the heavy fermion compounds CeCu_2Si_2 shows exponential temperature dependence at low-temperature, which is a signature of conventional, fully gapped, s -wave superconducting pairing symmetry. The temperature dependence of the specific heat data is well fitted with an inter-band SC gap as shown in Ref. [107]. We have also obtained an s -wave, fully gapped superconductivity with inter-band pairing. Within the generalized mean-field theory, this s -wave gap does produce an exponential temperature dependence in the specific heat and a fully gapped DOS as measured by tunnelling spectra. We claim our theoretical result is consistent with these two experiments based on these general behaviours.

It was shown that most of the above data, as well as the T^3 dependence of the NQR data[99, 100, 101] can be fitted well with a two-band model with a simple s -wave pairing symmetry. This is fully consistent with our theory which has a two-band (conduction and local) behavior with s -wave pairing. Furthermore, the proposed pairing (Eq. (2.2.20)) is a finite momentum pairing in the limit of fully localized f -electrons, and itinerant conduction electrons. Consistently, there have been recent evidence of finite momentum pairing state in CeCu_2Si_2 . [125] Finally, strong suppression of Andreev reflection amplitude in CeCoIn_5 , [124] and CeCu_2Si_2 [105, 106] are well known, suggesting the involvement of the localized f -orbitals in the Cooper pair as in the present case.

In addition, the present theory can also explain the other three experimental signatures which were taken earlier as evidence of unconventional, sign-reversal pairing symmetry. (i) The T^3 dependence of the NQR relaxation rate $1/T_1$ below T_c in CeCu_2Si_2 is often considered as evidence of line nodes in the SC gap structure.[99, 100, 101] As mentioned above, a two-band model with purely s -wave gap, as in the present case, is shown to reproduce the same power-law behavior of $1/T_1$ without invoking gap nodes.[107, 108] Therefore, we anticipate our theory is equally applicable here. (ii) The four-fold angular modulation of H_{c2} in

CeCu₂Si₂ [102] can be a signature of the SC gap anisotropy. However, it was shown in a realistic two-band model that a strong anisotropy in H_{c2} (as well as in other quantities) can well arise solely from the FS anisotropy even for a purely isotropic s -wave SC gap.[103] Indeed, the conduction electron's FS is known to be substantially anisotropic in CeCu₂Si₂. [122, 115]. (iii) Finally, it is known that a spin-resonance as measured by inelastic neutron scattering experiments can arise either from unconventional, sign-reversal pairing symmetry, or even for a fixed-sign s -wave pairing.[123] For sign-reversal pairing gap, the spin-resonance is typically very sharp and its energy $\omega_{\text{res}} < 2\Delta$, where Δ is the SC gap amplitude. On the other hand, for fixed-sign, conventional pairing, the resonance is usually very broad, and its energy lies at $\omega_{\text{res}} \geq 2\Delta$. The measured spin-resonance in CeCu₂Si₂ [104] is indeed quite broad, and the present data cannot discern if the resonance energy lies below or above 2Δ . This is because there is yet no direct measurement of the SC gap in this compound. Moreover, our theory also predicts a novel resonance mode at an energy (Eq. (2.4.53)) determined by $2\Delta^2/\bar{\xi}_f$.

We compare and contrast the concepts of the present theory with the prior theories of 'conventional' pairing solutions in CeCu₂Si₂. Valence fluctuation mediated or assisted pairing mechanism has been a steady theme of discussions in the HF community.[85, 88, 86, 89, 112, 91, 90, 113] Miyake and Onishi [88, 89] have proposed a phenomenological pairing vertex formula with the help of an empirical valence fluctuation susceptibility defined near its critical point. Unlike our case, the pairing vertex in Ref. [88] does not invoke electron-electron correlation, however, the pairing interaction is argued to be retarded when correlation is included. On the other hand, in our case, the pairing interaction is microscopically derived from the interplay between correlation and valence fluctuation and has a robust solution of attractive channel at the low-energy limit. Our pairing interaction can be considered as a generalized, dynamical Kondo interaction. If we express the interaction in Eq. (2.2.17) in terms of local spin and conduction spin interaction, then $V_{\mathbf{k}\mathbf{k}'}(\omega)$ can be casted as dynamical Kondo interaction $J_K(\omega)$ (similar result in the static limit can be obtained within the Schrieffer-Wolf transformation[20]). Starting from Kondo interaction with $J_K < 0$, a composite Cooper pair theory was proposed where conduction electron pairs up the (chargeless) fermionic represen-

tation of the local spin.[93, 95] Such composite pairing channel is also s -wave like in the limit local Kondo channel. A prior quantum Monte Carlo simulation of periodic Anderson model showed the existence of s -wave pairing interaction.[92] This gives a validation of the attractive pairing interaction we derived in Eq. (2.2.18). Finally, we propose that a future DMFT calculation will be valuable to further confirm the existence of the attractive pairing solution in such a model.

The effective interaction term in Eq. (2.2.16) is very generic and gives multiple order parameters. In the normal state, mean-field theory, we need to consider Hartree-Fock order parameters, $\Delta_h(\mathbf{k}') = \sum_{\mathbf{k}} V_{\mathbf{k}\mathbf{k}'} \langle c_{\mathbf{k}\sigma}^\dagger \bar{f}_\sigma \rangle$, $\Delta_c(\mathbf{k}, \mathbf{k}') = V_{\mathbf{k}\mathbf{k}'} \langle c_{\mathbf{k}\sigma}^\dagger c_{\mathbf{k}\sigma} \rangle$, $\Delta_f(\mathbf{k}, \mathbf{k}') = V_{\mathbf{k}\mathbf{k}'} \langle \bar{f}_\sigma^\dagger \bar{f}_\sigma \rangle$. For the Kondo insulating state, Δ_h opens up a hybridization gap in the electronic spectra.

Finally, we make few remarks about the future extension of the present theory. A full, self-consistent treatment of T_c , η , and T_K requires an Eliashberg-type formalism. Since T_c is significantly low in HF compounds, the present mean-field treatment is however a good approximation for the estimates of T_c . The theory also holds for dispersive f -electrons state as long as the corresponding bandwidth is much lower than U . For a dispersive f -state, one can obtain a zero center-of-mass momenta Cooper pair $\langle c_{\mathbf{k}\sigma}^\dagger \bar{f}_{-\mathbf{k}m}^\dagger \rangle$. Therefore, the present theory is applicable to the wider class of intermetallic and mixed valence superconductors where narrow-band and conduction band coexist, and possess finite interband tunneling (valence fluctuation) strength.[5] Our calculation does not include Coulomb interaction between the conduction and f -electrons (the Falicov-Kimball type interaction). However, it is obvious that such a Coulomb interaction term will lead to a pair breaking correction μ^* -term, in analogy with the Coulomb interaction correction to the electron-phonon coupling case (the so-called McMillan's formula)[126]. Finally, the vertex correction to the pairing potential can be envisaged, in analogy with the Migdal's theory, to scale as m/M , where m , and M are the mass of the conduction and f -electrons. Since $M \sim 10^3$ in these HF systems, we argue that the vertex correction can be negligible. The self-energy and vertex correction calculation required full diagrammatic many-body theory calculations. We need to do a self-consistent calculation like in the Eliashberg theory to make any precise prediction about the self-energy corrections. Our future work will address this issue.

Chapter 3

Prediction of f -wave pairing symmetry in $\text{YBa}_2\text{Cu}_3\text{O}_{6+x}$ cuprates

3.1 Introduction

In cuprate superconductors, d -wave pairing symmetry is well established in all member materials at most of the doping ranges.[8, 73, 127, 128] Supporting evidence to the d -wave pairing symmetry come from various complementary studies including junction experiments,[129] spectroscopies fingerprints of the nodal pairing states,[130, 131, 132] as well as power-law dependence in various thermodynamical and transport measurements.[8, 128, 136, 137, 138, 139, 140, 141] There have been few but robust contradictory evidence to the nodal SC gap in a limited doping region in several cupates. Notably, in electron-doped cuprates, in the deep underdoped region, various measurements exhibited the presence of nodeless SC gap, which was initially assumed to be a s -wave pairing symmetry.[142, 143, 144, 145, 146, 147, 148, 149, 150, 151] Later on, it was shown that the underlying pairing state has the d -wave symmetry, however owing to the loss of FS at the nodal region due to AFM order, the effective quasiparticle spectrum loses its gapless features.[152, 153] Furthermore, more recently, there have been convincing evidence of nodeless SC gap in the deep underdoped region of La-based,[154, 155]

Bi-based,[156, 157, 158] Cl-based,[159] and Yb-based hole-doped cuprates.[160] Theoretical explanation to this mechanism is still divided into whether an underlying d -wave state loses its nodal state due to correlation[161, 162] or disorder,[163] or a new pairing state arises here.[164, 165, 166, 167] However, so far there have not been any experimental indication or theoretical prediction for an f -wave pairing symmetry in cuprates. Oxygen doping introduces holes on the CuO_2 plane states, and YBCO_6 and YBCO_7 compounds represent undoped and overdoped samples, respectively, while superconductivity arises in between these two compositions.

Prior DFT calculations[168] showed that the chain state is absent from the Fermi level in the undoped (YBCO_6) compound, while it crosses the Fermi level for finite doping region. Photoemission measurement also exhibited the evidence of quasi-1D chain states on the Fermi level.[133, 134, 135] Various transport measurements consistently pointed out that the chain states are highly metallic.[169, 170] Moreover, at finite dopings, the chain state strongly hybridizes with the plane states near the magnetic zone boundary, establishing that the electron tunneling and/or charge transfer between the chain and plane states are strong enough to play important role on the low-energy properties of YBCO cuprates.[169, 170, 171, 172, 173, 174, 175, 176, 177, 178, 179] Recent experimental studies have achieved selectively doping only the chain state, while the plane state maintains a fixed doping level.[172, 176, 180].

This work is motivated by the above observations: does the chain states produce any significant changes of already established d -wave symmetry of cuprates, and whether the metallic chain state has any effect of superconducting T_c ? To understand this, we consider the doping variation of the chain state for various fixed doping concentrations on the plane state across its optimal doping regime. We find that for the natural doping ranges of the chain state, the pairing symmetry is $d_{x^2-y^2}$ -wave. But as the chain doping is tuned above some electron critical value, which is not naturally achieved in YBCO_{6+x} single crystals, the pairing symmetry on the plane states is changed to a f -wave pairing symmetry. The two pairing symmetry solutions we obtain have the \mathbf{k} -dependence form as

$$f\text{-wave} : \Delta_f = \sin k_x (\cos k_x - 3 \cos k_y - 2), \quad (3.1.1a)$$

$$d\text{-wave} : \Delta_d = \cos k_x - \cos k_y. \quad (3.1.1b)$$

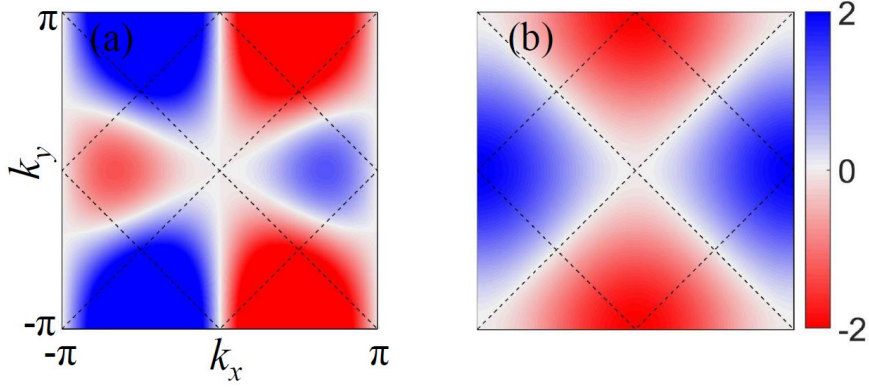


Figure 3.1: We visualize the \mathbf{k} -dependence of the SC pairing symmetries in (a) for f -wave (Eqs. (3.1.1a)), and in (b) for d -wave (Eq. (3.1.1b)). The colormap of red to blue gives negative and positive signs. We did not normalize the eigenfunctions in any of the results, since normalization gives a constant multiplication to the eigenfunctions. This plot is shown to ease the discussion of the pairing symmetry.

Where Δ^f and Δ^d are superconducting order parameters. In Fig. 3.1, we plot the pairing functions, Eqs. (3.1.1a), (3.1.1b), in the 2D BZ.

This pairing symmetry transition is linked to where the plane and chain states are hybridized in the BZ. This conclusion is found to be robust for a wide range of interaction strength as well as for various values of the hybridization strength between the two layers. While the f -wave pairing symmetry has not yet been reported for YBCO_{6+x} samples, but with the advent of layered dependent doping mechanism, such a pairing symmetry can be achieved in future experiments with electron doping on the chain states.

3.2 Tight binding model

The lattice structure of YBCO is shown in Fig. 3.2. We consider a three band model in which two CuO_2 layers are interacting with an uniaxial CuO chain state.[177, 178, 179] We work in the basis of $\Psi_\sigma(\mathbf{k})=(c_{p\sigma}(\mathbf{k}), c_{p'\sigma}(\mathbf{k}), c_{c\sigma}(\mathbf{k}))^T$, where $c_{\alpha\sigma}(\mathbf{k})$ annihilates an electron on the α^{th} layer with momentum \mathbf{k} , and spin $\sigma = \uparrow / \downarrow$, and the superscript $\alpha = p, p'$ refers to the two planes, and $\alpha = c$ stands

for the chain layer. In this spinor, the Hamiltonian reads as:

$$H = \begin{pmatrix} \xi_p & \xi_{pp'} & \xi_{cp} \\ \xi_{pp'}^* & \xi_{p'} & \xi_{cp'} \\ \xi_{cp}^* & \xi_{cp'}^* & \xi_c \end{pmatrix}. \quad (3.2.1)$$

(\mathbf{k} -dependence in all terms above are suppressed for simplicity). Here $\xi_{p/p'}$, and ξ_c are the intra-layer dispersions within the plane and chain states, respectively. $\xi_{pp'}$ and ξ_{cp} are the inter-layer hoppings between the two planes and between plane and chain states, respectively. The corresponding dispersion terms are obtained within the tight-binding model including nearest and various next-nearest neighbor hoppings as appropriate to describe the corresponding DFT band structure (see Refs. [177, 178]). Following the DFT result of weak k_z dispersion in this compound,[168] we neglect three-dimensional dispersion. The explicit forms of the dispersions are,

$$\xi_p = -2t(c_x + c_y) + 2t'c_xc_y + 2t''(c_{2x} + c_{2y}) - \mu_p, \quad (3.2.2a)$$

$$\xi_c = -2t_{cy}c_y - 2t_{cx}c_{2x} - \mu_c, \quad (3.2.2b)$$

$$\xi_{pp'} = -2t_{pp}(c_x - c_y)^2, \quad (3.2.2c)$$

$$\xi_{cp} = t_{cp}. \quad (3.2.2d)$$

$\mu_{p,c}$ are the onsite potentials for the plane and chain states. We use the brief notation of $c_{i\alpha} = \cos(i\alpha)$, where i dictates the inter-atomic distances in units of lattice vectors, and $\alpha = k_{x,y}$. We obtain the tight-binding parameters by fitting to the DFT band structure: $(t, t', t'', t_{cy}, t_{cx}, t_{pp}, t_{cp}, \mu_p, \mu_c) = (0.38, -0.18, 0.25, 0.66, 0.01, -0.01, 0.02, -0.37, -1.15)$ eV. We consider the anisotropy along the \mathbf{a} axis for the chain band by setting $t_{cx} \ll t_{cy}$, giving the chain band to be very much uniaxial along the \mathbf{b} axis.

Within our model, the particle-hole asymmetry of the tunnelling spectra can be explained as to arise from the particle-hole asymmetry in the non-interacting electronic structure. This arises from the next-nearest neighbour hopping t' . This gives a van-Hove singularity in the DOS right below the Fermi level and create the particle-hole asymmetry. Note that the tunnelling spectra obtained at tempera-

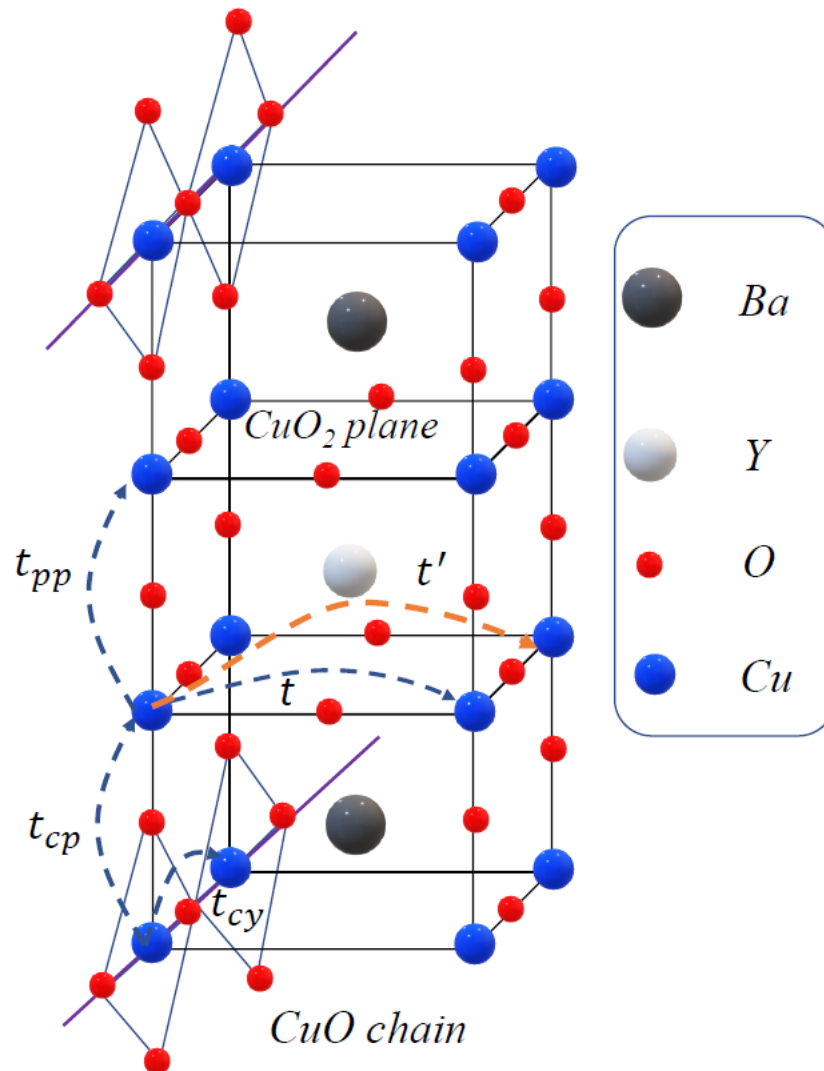


Figure 3.2: The lattice structure of YBCO is shown in the figure. The Unit cell consists of CuO_2 plane layers and unidirectional CuO chain layer. t and t' are the nearest neighbour and next-nearest neighbour hopping in the plane layer. Interlayer hopping between chain-plane and plane-plane are indicated by t_{cp} and t_{pp} respectively.

ture above the pseudogap region also shows the particle-hole asymmetry which is reproducible within our model.

We diagonalize the Hamiltonian in Eq. 3.2.1 and obtain three eigenvalues $E_\nu(\mathbf{k})$ and corresponding eigenvectors $\phi'_\alpha(\mathbf{k})$, where ν denotes band indices, and α stands for layer species. We assume the operator for annihilating a quasiparticle in the ν^{th} -band with spin σ is $\gamma_{\nu,\sigma}(\mathbf{k})$. Then the spinor in the eigenbasis is $\Phi_\sigma(\mathbf{k}) = (\gamma_{1\sigma}(\mathbf{k}), \gamma_{2\sigma}(\mathbf{k}), \gamma_{3\sigma}(\mathbf{k}))^T$.

The density operators for the i^{th} layer for the spin σ is, $n_{i\sigma}(\mathbf{q}) = \frac{1}{\Omega_{\text{BZ}}} \sum_{\mathbf{k}} c_{i\mathbf{k}\sigma}^\dagger c_{i\mathbf{k}+\mathbf{q},\sigma}$. We fix the charge density for plane and chain states separately by self-consistently evaluating the density operators at $\mathbf{q} \rightarrow 0$. The electron concentration on the plane state is taken as average over the two planes $n_p = 2\frac{1}{2}(\langle n_p \rangle + \langle n_{p'} \rangle)$, and that for the chain state is $n_c = 2\langle n_c \rangle$. Here the factor 2 originates from spin-degeneracy. The thermal average is taken over *all* eigenstates with $\langle \gamma_{\nu\sigma}(\mathbf{k}) \rangle = f(E_\nu(\mathbf{k}))$ is the Fermi-Dirac distribution function. Both carrier densities are computed self-consistently. We self-consistently fix the value of n_p and n_c by treating μ_p and μ_p as free parameters.

3.2.1 Multi-band RPA susceptibility

Next, to study the modulation of FS nesting profile and feed the corresponding information to the spin-fluctuation mediated pairing potential, we consider a multi-band Hubbard model:

$$H_{\text{int}} = \sum_{\alpha \in p, p', c} U_\alpha n_{\alpha\uparrow} n_{\alpha\downarrow} + \sum_{\substack{\alpha \neq \beta \in (p, p', c) \\ \sigma \sigma' \in (\uparrow, \downarrow)}} V_{\alpha\beta} n_{\alpha\sigma} n_{\beta\sigma'}. \quad (3.2.3)$$

$U_p = U_{p'}$ is the onsite Hubbard interaction between the two plane layers, while U_c is the same for intra-chain layer. V_p, V_c are the onsite Hubbard interaction between the two planes, and plane-chain layers. Hund's coupling between these layers (all with $d_{x^2-y^2}$ orbitals symmetry) is ignored. By expanding the interaction term to multiple-interaction channel, and collecting the terms which give a pairing interaction (both singlet and triplet channels are considered) we obtain the effective pairing potential $\Gamma_{\alpha\beta}^{\gamma\delta}(\mathbf{q})$ Eq. (1.6.25). [72, 73, 74, 71, 75, 76, 77]

The non-vanishing components of the onsite Hubbard interactions are, $(\tilde{U}_{s,c})_{\alpha\alpha}^{\alpha\alpha} =$

$U_{p/c}$ for intra-plane ($\alpha = p, p'$) and intra-chain ($\alpha = c$) layers. According to the definition in Eq. (3.2.3), the inter-plane Coulomb interaction enters into $(\tilde{U}_{s,c})_{pp'}^{p'p'} = V_p$, and plane-chain interaction is, $(\tilde{U}_{s,c})_{pp}^{cc} = (\tilde{U}_{s,c})_{p'p'}^{cc} = V_c$.

3.3 Results

3.3.1 Electronic structure

We start with the discussion of the electronic structure and FS topologies for various representative cases in Fig. 3.3. For most discussions in this section, we focus on near-optimal doping region of $n_p = 0.82$ ($x_p \approx 0.18$, $\mu_p = -0.35$ eV) for the plane state, and vary chain state filling factor $n_c = \{0.95, 0.53, 0.15\}$, corresponding chemical potential for chain states are ($\mu_c = -0.1, -0.9, -1.29$ eV) Figs. 3.3 [(d) - (f)] respectively. The topology of the chain band allows it to accommodate electron-like FS in all cases. For the deeply electron-doped region, it forms open-orbit FS as shown Figs. 3.3 [(d) - (e)]. When the chain band becomes nearly empty, see Figs. 3.3 [(c) - (f)], the corresponding FS forms nearly closed electron-like FS [due to finite second-nearest neighbor chain-chain hopping $t_{cx} \neq 0$ along the a -direction]. In the low filling factors ($n_c = 0.15$), the FS matches those of the DFT results[168] and ARPES data[133, 134, 135] in the single crystal of YBCO_{6+x} samples [e.g., Figs. 3.3 [(e)-(f)]]].

The previously unexplored region of large filling factor n_c in Figs. 3.3(d) is of our prime interests. Because here we obtain f -wave pairing solutions as shown below. The momentum point where the chain and plane states' FSs meet as 'hybridization hot-spot' (HHS), see Fig. 3.3(d)-(e). In this region, we find that the HHS lies above the BZ diagonal direction. In this case, we will show below that the FS nesting wavevector between the two chain FSs becomes comparable to that of the plane state and thus intervenes the overall FS nesting driven pairing potential, and hence the pairing symmetry is altered.

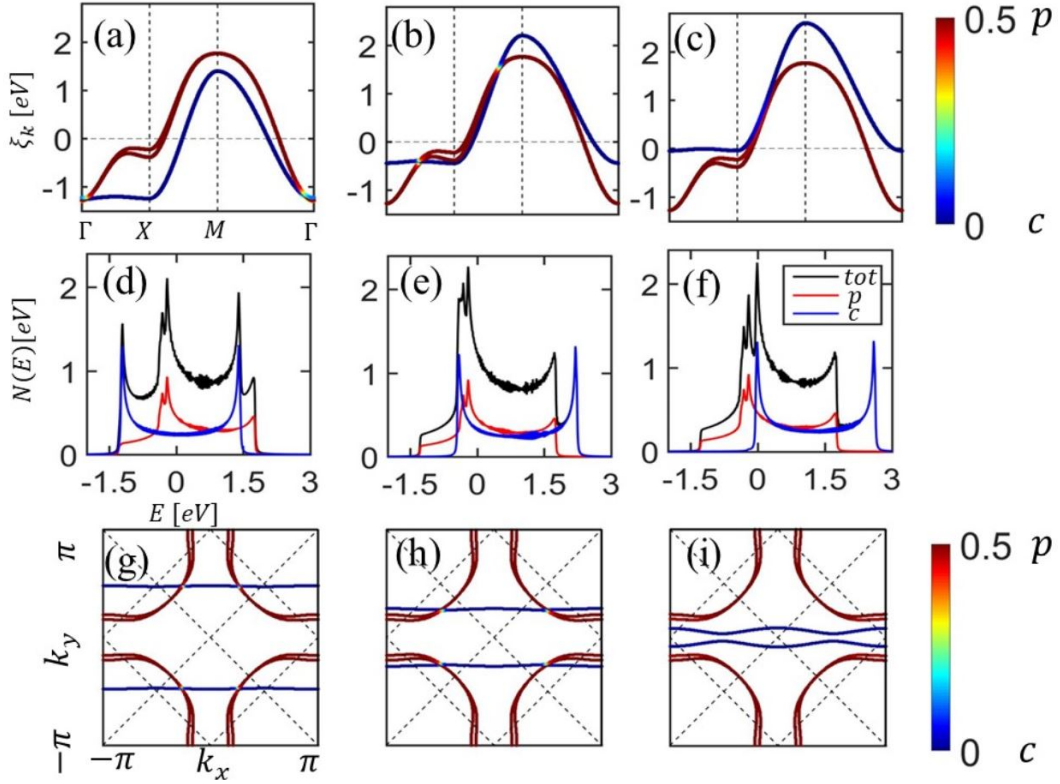


Figure 3.3: (a)-(c) Electronic structures of the three band non-interacting model, Eq. (3.2.1), for three doping values on the chain states, while the doping on the plane state is kept fixed. (d) -(f) Total DOS is denoted by black line, and corresponding orbital contributions are denoted by red (plane), blue (chain) lines. (g)-(i) Corresponding FSs are shown for the three cases presented in the upper panel. Red to blue color map in a given band at a \mathbf{k} -point gives the orbital contribution from the plane and chain states, respectively. (a) & (g) When chain state is highly electron-doped, the HHS lies above the diagonal direction of the BZ, where a f -wave pairing symmetry is obtained. (b) & (h) At the intermediate electron-doping on the chain state, which is realized in single crystal YBCO samples, the HHS moves below the BZ diagonal direction, and here we obtain d -wave pairing solution. (c) & (i) A characteristic doping where the bottom of the chain band just lies at the Fermi level, giving high-DOS at the Fermi level, and hence SC strength reaches its optimum value as a function of chain state doping for a fixed plane doping.

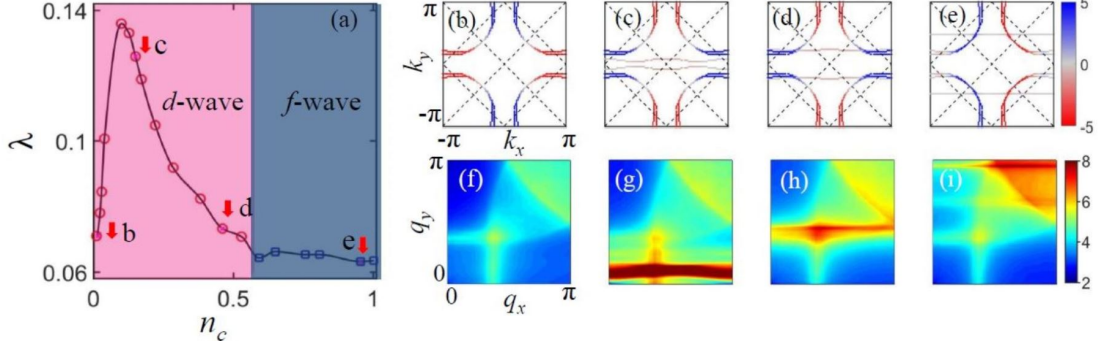


Figure 3.4: (a) We plot the leading SC eigenvalue (coupling constant) as a function of chain state **doping**. Blue square and red circles denote f - and d -wave symmetries, respectively, as the leading pairing instability. Light and dark shadings denote doping regions with d and f - wave pairing symmetries, respectively. (b-e) Computed pairing eigenfunction $\Delta_{\mathbf{k}}$ for the leading eigenvalue, plotted on the corresponding FSs, for four representative values of n_c . Here red to blue colormap denotes the negative to positive sign of $\Delta_{\mathbf{k}}$. (f-i) Corresponding RPA spin susceptibilities (traced over all orbitals) $[\text{Tr}(\tilde{\chi}_s)]$ for the same cases as shown in the corresponding upper panels. All plots are shown in the same color scale for easy comparison. Here we used $\mu_p = -0.35$ eV and the corresponding plane state doping is $x_p \approx 18\%$. $\mu_c^{\text{max}} = -1.31$ eV and corresponding $n_c^{\text{max}} = 0.1$.

3.3.2 Evolution of FS nesting with chain doping

Next, we discuss the FS nesting profile as a function of chain state filling n_c while keeping the plane doping fixed at $n_p \approx 0.82$, in Figs. 3.4(f-i). Here we mainly focus on the RPA spin susceptibility plotted as a function of (q_x, q_y) , since it contributes most to the pairing interaction. Throughout the calculation, we fix Coulomb interactions as intra-band $U_{p,c} = 0.7, 0.6$ eV, and inter-band $V_{p,c} = 0.5, 0.5$ eV (we also explore the U, V dependence of the results below in which the conclusions remain intact). It is easy to identify that the nearly horizontal part in the $\chi_s(\mathbf{q})$ plot stems from the intra-chain FS nesting, while the rest of the features are dominated by plane FS nestings. Of course, both nestings are affected by the each other. Especially, it is worthwhile mentioning that in the case of no chain FS in Fig. 3.4(b), the corresponding plane state nesting profile continues to break the C_4 rotational symmetry. This occurs due to plane-chain hopping t_{cp} as well as their interaction V_c .

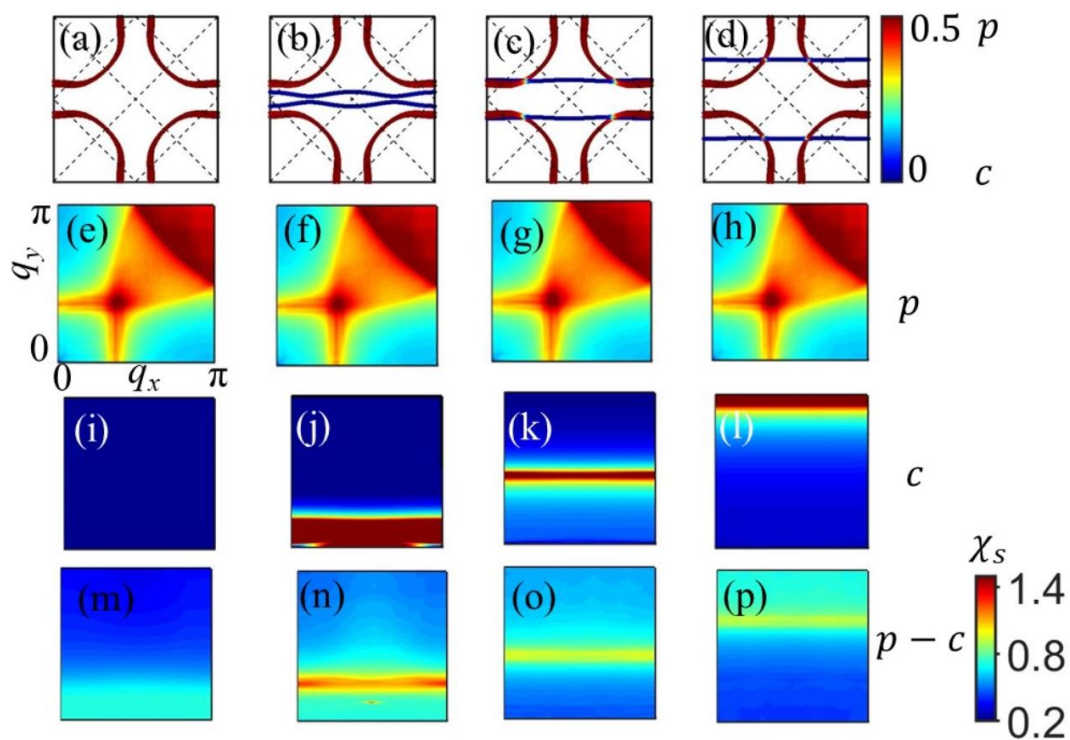


Figure 3.5: (a)-(d) FSs are shown for the four cases presented in the upper panel. Computed RPA spin susceptibility (Eq. (1.6.23)) is split for three channels: intra-plane in (e)-(h), intra-chain in (i)-(l) and plane-chain in (m)-(p). Filling factors are $n_p = 0.82$ and $n_c = 0.01, 0.15, 0.46, 0.94$. $U_{p/c} = 0.7, 0.6$ eV, and $V_{p/c} = 0.5, 0.5$ eV. All plots are done in the same colorbar.

In Fig. 3.5, we separately show the contributions of the intra-plane, intra-chain and plane-chain susceptibilities for the spin-channels only. We notice that the FS nesting in the plane channel is very similar to the ones obtained in other cuprates without a chain state. The intra-chain FS nesting is almost one dimensional with very weak anisotropy in the intensity. This is due to low k_x -dispersion at finite filling factor. The inter-layer plane-chain FS nesting is also quasi-1D with significantly low intensity.

Let us define the chain state FS nesting wavevector as $\mathbf{Q}_c \sim (\text{all } q_x, Q_{cy})$. For plane state, the FS nesting wavevector of present interest is the one near the (π, π) point, but it is incommensurate at finite dopings in all hole-doped cuprates. We denote it by $\mathbf{Q}_p^{(1)} \sim (\pi, Q_{py})$ and $\mathbf{Q}_p^{(2)} \sim (Q_{px}, \pi)$. For other C_4 invariant cuprates, $Q_{px} = Q_{py}$, but it is not the case in YBCO due to coupling with the chain state. We find that in the regions of high chain state filling factor (n_c) – when the chain FS is large and the HHS lies above the BZ diagonal – $Q_{cy} \sim Q_{py}$, see Fig. 3.4(i). This makes the total spin susceptibility to possess a dominant nesting strength at Q_{py} compared to that at Q_{px} . As a result of the effective C_4 symmetry breaking in the spin susceptibility, and hence in the pairing interaction, the pairing eigenfunction $\Delta(\mathbf{k})$ also acquires a symmetry which lacks this symmetry. This gives the f -wave symmetry.

With decrease of the chain state occupancy, the chain FS nesting wavevector becomes smaller than the plane state nesting, i.e., $Q_{cy} < Q_{py}$, and thus their contributions become decoupled. In such a case, we find that the pairing symmetry will be essentially dictated by the plane FS nesting, which gives a d -wave pairing. For a fixed plane layer filling factor n_p , the transition from the f -wave to d -wave solution occurs very much when the Q_{cy} becomes smaller than Q_{py} . On the other hand, for $Q_{cy} \geq Q_{py}$, we find that the f -wave solution always dominates the d -wave solution.

In the intermediate chain state occupancy when the chain FS and plane FS's van-Hove singularity merge, see Fig. 3.4(h), the wavevector Q_{cy} merges with the charge order wavevector of the plane state. This can promote a stronger and uniaxial charge ordering strength.[181] Here, we do not investigate further the charge order state, and returns back to the pairing solution at the spin-fluctuation wavevector henceforth.

The chain band bottom is almost flat in the Cu-O bond direction. So, when the chain band becomes nearly empty, and the flat band reaches the Fermi level, its high DOS have useful ramification, see Fig. 3.4(c). In this case, $Q_{cy} \rightarrow 0$, giving an almost massless, unidirectional paramagnon mode in the chain state, see Fig. 3.4(g). As the result, the overall carrier concentration at the Fermi level is drastically enhanced. This enhancement optimizes the SC pairing strength as a function of chain state doping, as also obtained in the numerical result (to be discussed below). However, such a massless paramagnon mode dose not directly contribute to the unconventional pairing mechanism outlined in Sec. 1.6.2. For the pairing solution, the antiferromagnetic wavevector in the plane state is important, and hence we obtain a d -wave solution, with only a strong enhancement of the pairing strength is added by large DOS of the chain state.

Finally, as the chain state becomes completely empty, the overall FS topology and the nesting profile is dictated by the plane state. However, due to finite coupling to empty chain bands, the susceptibility topology continues to exhibit a slight loss of four-fold rotational invariance as shown in Fig. 3.4(f).

3.3.3 Superconducting properties

We now turn to the main topic of superconductivity. We use the multi-band Hubbard model [see Sec. 1.6.2 Eq. (1.6.14)], where intra and inter orbital Hubbard interactions are given by $U\{U_p, U_c\}$ and $V\{V_p, V_c\}$. Then, using spin fluctuation theory, we study the pairing symmetry of YBCO. Using the spin fluctuation potential, we solve the self-consistent gap equation Eq.(1.6.29) and obtain pairing symmetry and pairing strength (λ) as a function of chain filling. For the same doping value where susceptibility results are discussed in the above section, we report the solutions of the largest eigenvalue and eigenfunction in Fig. 3.4(a) and Figs. 3.4(b-e). The eigenfunction is plotted on the corresponding FS in a colormap with blue to red colors denoting positive to negative sign of the pairing eigenfunction $\Delta(\mathbf{k})$.

Our nesting results reveal that when the chain nesting $Q_{cy} \geq Q_{py}$, the FS nesting at $\mathbf{Q}_p^{(1)} = (\pi, Q_{py})$ dominates over $\mathbf{Q}_p^{(2)} = (Q_{px}, \pi)$. Hence the pairing potential and pairing eigenfunction inherits this broken C_4 symmetry. Moreover,

the weak q_x dependence of the Q_{cy} nesting wavevector implies that more Fermi momenta k_x are nested by this fixed wavevector, due to weak k_x dispersion of the chain state as seen in Fig. 3.3. This in-plane anisotropic nesting promotes a pairing symmetry which favors the condition: $\text{sgn}[\Delta(k_x, k_y)] = -\text{sgn}[\Delta(k_x + \pi, k_y + Q_{py})]$ at all k_x - points. Owing to the FS topology of the plane state, such a condition is satisfied as $k_x \rightarrow -k_x$. As we reach the BZ boundary near $\mathbf{k} \sim (\pm\pi, 0)$, the condition is reversed in such a way that the pairing symmetry further changes sign, see Fig. 3.3(f). This is the reason, a purely p -wave solution (which flips signs for all $k_x \rightarrow -k_x$) is overturned by a higher-angular momentum solution with odd-parity. As a result, we have a f -wave pairing state in this doping region of the chain state.

In Fig. 3.4(a) we plot the largest eigenvalue with blue square and red circles for f -wave and d -wave solutions, respectively. As anticipated, for large electron occupancy in the chain state which gives $Q_{cy} \geq Q_{py}$, we obtain a f -wave pairing solution. Otherwise, the pairing symmetry is the typical d -wave type. In addition, we also find that the value of the largest eigenvalue (pairing strength) gradually increases with decreasing chain state filling factor n_c (keeping everything else fixed). This increment is related to the competition between the spin fluctuation magnitude (directly enhancing the pairing strength), as well as the total DOS on the Fermi level. We notice that with decreasing chain state occupancy, the flat band of the chain state approaches the Fermi level, and hence enhances the carrier concentration. As the chain state moves completely above the Fermi level, the pairing strength again starts to decrease. This gives a new tunability to enhance superconductivity in YBCO cuprates by selectively reducing the chain states occupancy. In the existing experimental reports, such a selective tunability of the chain state is not directly explored, and hence the confirmation of our prediction awaits a focused experiment along this direction.[180]

Next we investigate the evolution of the pairing symmetry and the corresponding pairing eigenvalue λ as a function of n_p and n_c in Fig. 3.6. Blue square and red circles distinguish between the f -wave and d -wave pairing eigenvalues, respectively, as the leading solution for a given case. We consistently find that above a critical chain filling factor n_c for a fixed n_p , the pairing symmetry remains d -wave. The d -wave eigenvalue λ reaches an optimum value when the chain state passes through the Fermi level. For higher value of n_c , when the chain nesting vector

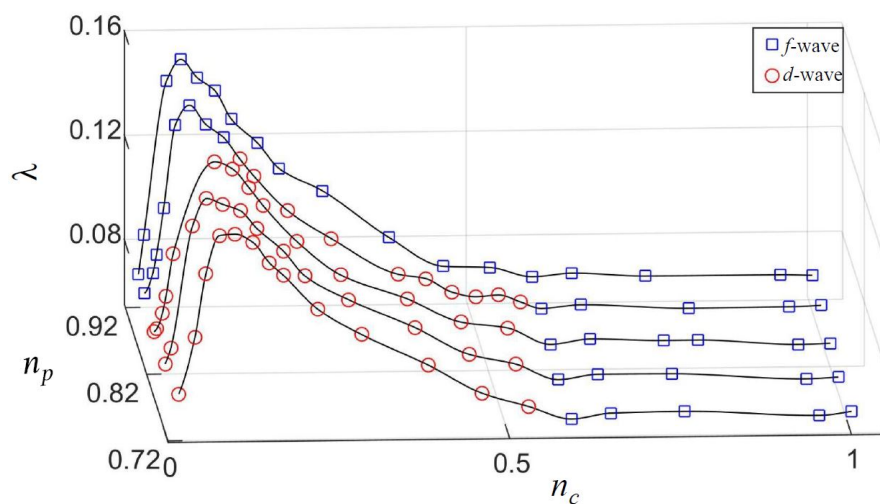


Figure 3.6: (a) We plot the leading pairing strength as a function of n_c for several fixed values of n_p . In all cases, we have fixed the interaction strength and all tight-binding parameters. Blue square and red circles distinguish the leading pairing strength for f -wave and d -wave cases, respectively, and the solid line is guide to the eye. There are prominent maxima of the pairing strength at an optimum chain doping, where the chain state's bottom crosses the Fermi level. The optimum chain doping varies only weakly on the plane state doping.

Q_{cy} becomes comparable to that of Q_{py} of the plane state, the pairing symmetry changes to a f -wave symmetry. This condition varies for different n_p values since the values of Q_{py} is also doping dependent.

Our results indicate a reentrant of the f -wave solution for lower hole doping on the plane state at higher values of n_c . In fact, with even lower hole doping, the entire n_c range shows a f -wave solution to be dominant over the d -wave solution (the difference between the two eigenvalues is however very small). This occurs because the FS nesting in the plane state becomes more commensurate, tending the FS instability toward other density wave orders (such as charge density wave, spin-density wave, etc). However, the chain state nesting continues to grow and dominate over the plane state nesting. Caution to be taken for the results in the underdoped region. Note that our ground state in the non-SC state is a paramagnet with full FSs. The FS becomes gapped out due to charge order, pseudogap etc in the underdoped region. In fact, in the underdoped region, experiments suggest a nodeless SC gap in YBCO and other cuprates,[160] which presumably arises due to competition with the normal state competing orders.[165, 166, 167]

Finally, we address the robustness of the conclusions with respect to the interaction strength U_p , V_c in Fig. 3.7, as well as as a function of plane-chain hopping strength (t_{cp}) in Fig. 3.8. We indeed find that both results are robust to the values of t_{cp} , U_p , and V_c . This confirms that the pairing symmetry is nearly indifferent to these parameters, and is mainly determined by the FS topology and nesting profile which are dictated by filling factors. Of course, the magnitude of the pairing potential, and hence the value of the pairing eigenvalue λ are sensitive to the energy scales of the problem which depends on t_{cp} , U , V .

3.4 Discussions and Conclusions

Much like increasing the SC transition temperature T_c , obtaining varieties of unconventional pairing symmetry is an important milestone in the field of superconductivity. Especially, the odd parity pairing symmetry holds special position in the field in pursuit of governing triplet pairing, chiral pairing, topological superconductivity, and Majorana edge modes, etc. f -wave pairing symmetry is odd under inversion, and hence is naturally arising in the spin-triplet channel to conform the

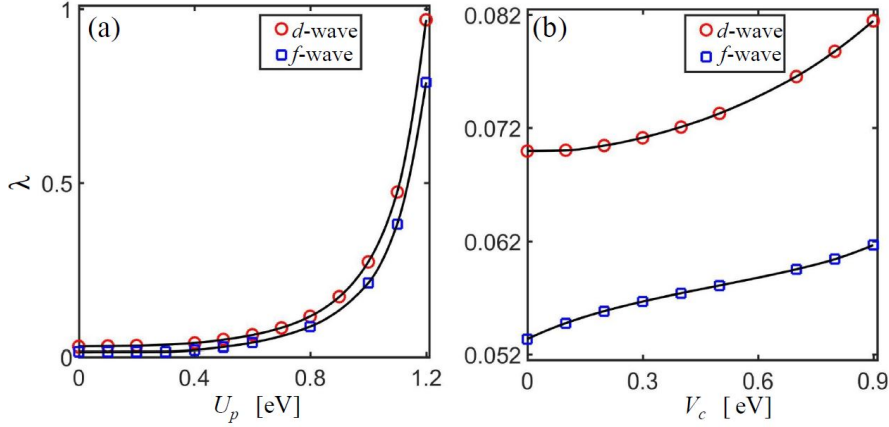


Figure 3.7: We plot the the two pairing eigenvalues for f -wave and d -wave channels as a function of U_p , and V_c , keeping all other parameters fixed. Here we choose $n_p = 0.82$, $n_c = 0.38$ ($\mu_p = -0.35$, $\mu_c = -1.1$ eV) for d -wave symmetry, and $n_p = 0.82$, $n_c = 0.84$ ($\mu_p = -0.35$, $\mu_c = -0.3$ eV) for f -wave symmetry for both (a), (b). The solid line is guide to the eye. The results reveals that for the doping region, where f -wave eigenvalue is larger than that of the d -wave, this conclusion remains unchanged as a function of U_c and V_c . For the other doping, where d -wave is dominant over f -wave, the conclusion is also invariant for the values of U , V .

antisymmetric wavefunction criterion. So far, there have been some discussions of time-reversal symmetry breaking pairing channels with $d + id$ or $s + id$ pairing channel in the spin singlet channel,[164] or p -wave solutions in the spin-triplet channels[165, 166, 167] in cuprates. However, the exploration of the chain state doping has not been pursued in the context of pairing symmetry in the literature.

Proposals of f -wave pairing have been put forward in HF UPt_3 ,[182] twisted bilayer gaphene,[183] monolayer MoS_2 ,[184], cold atom optical lattice,[185] p -doped semi-conductors,[186] honeycomb lattices,[187], and other superconductors [188]. However, apart from indirect hints of such pairing symmetry in UPt_3 ,[182] this state has not been directly realized in other families.

The f -wave pairing symmetry in YBCO samples results from the competition between the chain and plane states' nesting conditions. The plane state nesting along (π, π) gives the d -wave symmetry. However, as the uniaxial nesting of the chain state becomes comparable in the nesting wavevector, and nesting strength to the plane state one, it breaks the C_4 rotational symmetry in the pairing poten-

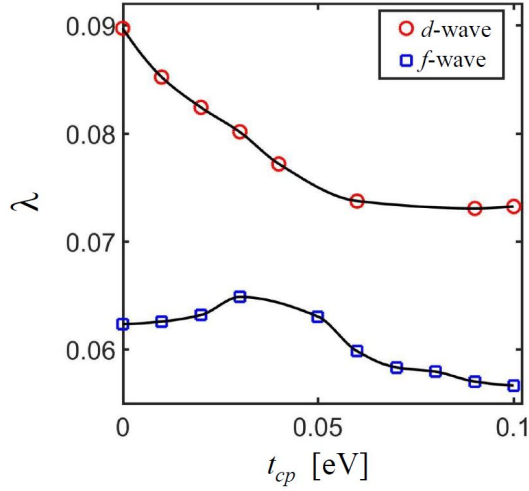


Figure 3.8: We plot λ as a function of the plane-chain tunneling amplitude t_{cp} on the pairing eigenvalues. Here we choose $n_p = 0.82$, $n_c = 0.38$ ($\mu_p = -0.35$, $\mu_c = -1.1$ eV) for d -wave symmetry, and $n_p = 0.82$, $n_c = 0.94$ ($\mu_p = -0.35$, $\mu_c = -0.1$ eV) for f -wave symmetry. $U_{p/c} = (0.7, 0.6)$, $V_{p/c} = (0.5, 0.5)$ in eV. We conclude that for the doping where d -wave is dominant over f -wave, it remains so for all values of t_{cp} , and vice versa.

tial. Hence the f -wave pairing symmetry arises. In this pairing state, the Fermi momenta change sign for all values of $k_x \rightarrow -k_x$, in addition to an additional sign reversal between $k_y \rightarrow -k_y$ near the BZ boundary only.

Within weak-coupling approximation, experimental evidence [134] supports the existence of coherent Fermi surface at most of the Brillouin zone and high incoherent spectral weight at high frequency. In the optimal doping region, the Coulomb interaction is screened, making it smaller than electronic bandwidth. There are more supports from numerical studies that optimal to overdoped limit weak-coupling theory is successful in describing the low energy spectra.

The half-filled state is not a Mott insulating phase, but rather an antiferromagnetic insulator phase, within the weak-coupling theory [1]. This issue can be addressed in momentum space. It is well known in cuprates that the next nearest neighbour and higher hopping parameters are quite significant, producing a non-interacting bandwidth which is ~ 2 -3 eV. This is an order of magnitude larger than the nearest neighbour hopping amplitude of ~ 0.25 eV. Hence, compared to

this bandwidth, the effective Hubbard $U \sim 0.5-0.7$ eV falls into a weak coupling region. Here the perturbation theory seems to work well, at least in describing the low-energy quasiparticle behaviours

As we mentioned before, the prediction of the f -wave pairing solution is obtained in the doping range where the carrier concentration of the chain state is substantially reduced to its intrinsic values in YBCO samples. Therefore, it is crucial to be able to dope the chain layer without altering doping concentration in the plane layers. Many organic superconductors also host quasi-one dimensional chain state with anisotropic nesting and transport properties.[189] Therefore, the search for a f -wave pairing can be easily extended to this family.

Chapter 4

Orbital-selective superconductivity of infinite-layer nickelates

4.1 Introduction

The first nickelate structure containing 2D NiO₂ planes that was synthesized is the infinite-layer LaNiO₂ (LNO) [60]. Subsequently, another member of the infinite-layer nickelate series, namely, NdNiO₂ (NNO) has been synthesized [190]. Very recently, NNO has been shown [59] to be SC upon hole doping with $T_c \approx 9$ -15 K with a number of studies devoted on this topic [62, 191, 192, 193, 194, 195, 196, 197]. The situation became further curious by the report of PrNiO₂ (PNO) [198] exhibiting superconductivity with $T_c \approx 7$ -12 K. Superconductivity in LNO is not yet reported, though NNO and LNO are isostructural.

Given this background, a natural question would be, can doped carriers give rise to superconductivity in such a two-band model description of NNO, PNO and LNO, and if so, is there any difference between NNO, PNO and LNO? This, to the best of our knowledge, has remained unexplored so far, though superconductivity in nickelates has been explored within the framework of one-band, and three-band model with onsite correlations [192], one-band Hubbard model [194], and multi-band Ni d - Nd d Hubbard model within fluctuation-exchange approximation [191],

as well as from strong coupling starting points [199, 200, 201].

In the present study, we consider a two-band model [202]. The main finding of the DFT calculations [202, 203] is that the Ni s basis forms an axial orbital, resulting from the hybridization of Nd/La $3d_{z^2}$, Nd/La d_{xy} , Ni $3d_{z^2}$ and Ni s . Moreover, while the downfolded Ni- $d_{x^2-y^2}$ orbital is very similar in the La and Nd compounds, the detailed nature of the axial orbital set these two materials apart, giving clue to its possible role on the materials dependent superconductivity.

We next solve the pairing eigenvalues and pairing eigenfunctions of the spin-fluctuation mediated pairing interaction, computed within the two-orbital Hubbard model. We find that (i) in the Nd compound, the SC coupling constant λ grows almost exponentially with the inter-orbital interaction V_{sd} , while the intra-orbital interactions alone is not conducive for superconductivity. In a crude analogy with the renormalization theory, we can say that intra-orbital interactions are ‘marginal’ – do not directly mediate superconductivity, while the inter-orbital interaction is a ‘relevant’ parameter for superconductivity. (ii) Secondly, in NNO and PNO, we find that the pairing eigenfunction turns out to be orbital selective: being a 2D $d_{x^2-y^2}$ type for the Ni d orbital, and a 3D d_{z^2} type symmetry for the axial orbital. The results are consistent with the corresponding orbital weight distributions on the 3D FS topology, and the corresponding FS features. The same study in LNO results in a single $d_{x^2-y^2}$ wave pairing symmetry, but with SC coupling constant significantly smaller than that of NNO and PNO. Our findings emphasize the importance of axial orbital and a two-band model in which orbital selective pairing symmetry is augmented by the inter-orbital interaction.

4.2 Two-band model

Fig. 4.1 shows crystal structure of nickelate compound with general formula $R\text{NiO}_2$ ($R = \text{Nd, La, Pr}$). The band structure of NNO, LNO, which is well studied in literature [62, 192, 204, 205], primarily consists of O $2p$ dominated bands ranging from about -8 eV to about -3 eV, Ni $3d$ dominated bands ranging from about -3 eV to 2 eV, and Nd/La $5d$ dominated bands ranging from about -1 eV to 8 eV.

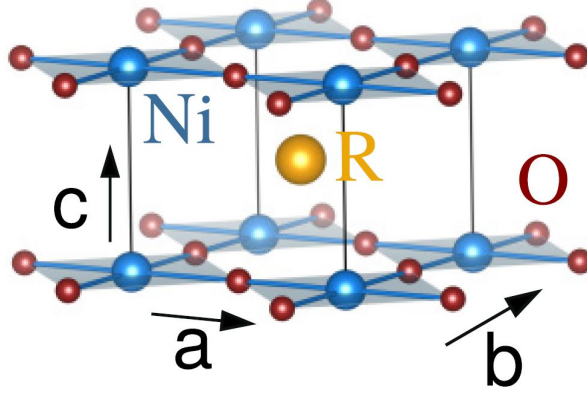


Figure 4.1: Crystal structure of infinite-layer RNiO₂ (R = Pr/Nd/La).

We discuss the electronic structure¹ of NNO, LNO, PNO in Fig. 4.2 [(a)-(c)]. We calculate the electronic structure at the optimal doping $x \sim 0.20$. The low-energy electronic structure has two-bands crossing the Fermi level: one canonical Ni $d_{x^2-y^2}$ band creating a hole pocket centered around M (A) point [see Fig. 4.2 [(g)-(i)]], bearing strong resemblance with cuprates, and the other one is derived out of Nd/La d mixed with Ni characters creating electron pockets at Γ and A points. While the generic features are found to be similar in the band structures of NNO, LNO and PNO, Fig. 4.2 [(a)-(c)], there are subtle differences.

Comparing the Ni $d_{x^2-y^2}$ bands in the three compounds, while it extends from -1.1 eV to 2 eV for NNO and PNO, it extends from -0.9 eV to about 2 eV for LNO, making the bandwidth of Ni $d_{x^2-y^2}$ in LNO band smaller by about 0.2 eV as compared to NNO, PNO. The corresponding k_z dispersion is also smaller for LNO compared to NNO. The saddle point at R is positioned about 0.2 eV higher compared to that at X in LNO, whereas R saddle point is about 0.5 eV higher compared to that at X for NNO. This k_z dispersion highlights the mixing with the axial orbital, making the Ni $d_{x^2-y^2}$ band deviating from its 2D nature, as emphasized by Lee and Pickett.[62] Comparing the second band, we find that firstly the Nd d -Ni derived electron pocket centered around Γ is about -0.4 eV

¹Band structure calculations are done by Subhadeep Bandyopadhyay [202, 203]

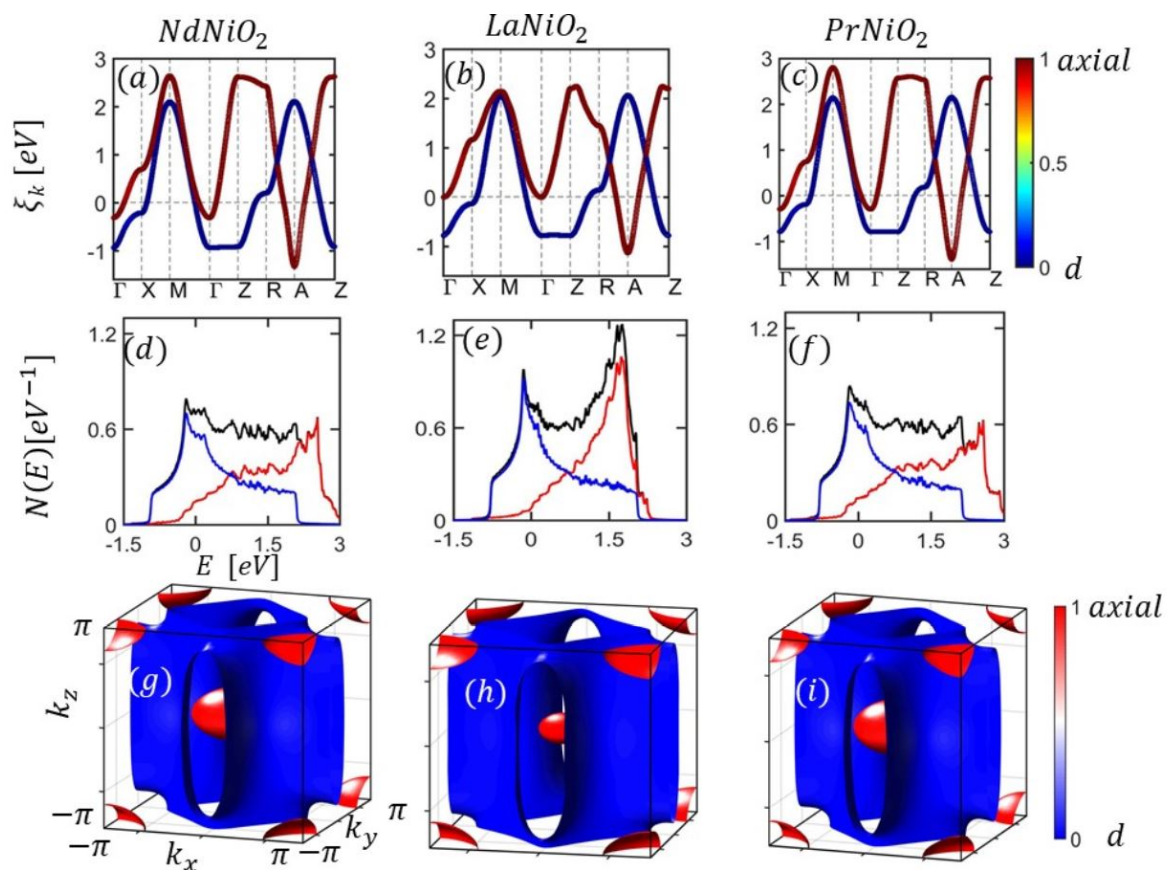


Figure 4.2: (a)-(c) The band structure for NNO, LNO and PNO, plotted along the high symmetry points of tetragonal unit cell, $\Gamma(0,0,0)$ -X($\pi/a,0,0$)-M($\pi/a,\pi/a,0$)- Γ -Z($0,0,\pi/c$)-R($\pi/a,0,\pi/c$)-A($\pi/a,\pi/a,\pi/c$)-Z. Blue ($d_{x^2-y^2}$) to red (axial d_{z^2}) colormap depicts the orbital contributions. (d)-(f) The total DOS (black) dashed line and corresponding orbital contributions are labelled by solid lines. (g)-(i) FS of the NNO, LNO, PNO respectively, with the orbital contributions are denoted in the colormap. Band structure calculations are done by Subhadeep Bandyopadhyay [202, 203].

lower in energy in NNO, PNO as compared to LNO, making the self-doping effect more pronounced in the Nd compound compared to the La compound. Secondly, the width of the second band is about 1 eV smaller in LNO compared to NNO.

The axial orbital is a hybrid between Ni s , Ni d_{z^2} , Nd/La d_{z^2} and Nd/La d_{xy} . Inspecting this orbital [202, 203], we find that starting from the central Ni atom, Ni d_{z^2} which bonds to Ni s , and antibonds to O p_x/p_y , bonds strongly with predominant feature of Nd/La d_{z^2} and d_{xy} , highlighting the hybridization between Ni and Nd/La d . We find that the Ni d_{z^2} /Ni s character is more in La compound compared to Nd compound, while Nd d_{z^2} /Nd d_{xy} character is less in La compound compared to Nd compound. This makes the axial orbital much more cylindrical in NNO, PNO and more spherical in LNO.

4.3 Results

4.3.1 Evolution of nesting in nickelates

We consider a two-band Hubbard model with interaction Hamiltonian given by,

$$H_{\text{int}} = \sum_{i,\sigma} U_i n_{i\sigma} n_{i\bar{\sigma}} + V_{sd} \sum_{i \neq j, \sigma \sigma'} n_{i\sigma} n_{j\sigma'}, \quad (4.3.1)$$

where $n_{i\sigma}$ is the number density of the i^{th} ($=1,2$) orbital, and spin $\sigma/\bar{\sigma}=\uparrow/\downarrow$. U_i are the intra-orbital interactions, and V_{sd} is the inter-orbital interaction. The non-vanishing components are $(\tilde{U}_{s,c})_{\alpha\alpha}^{\alpha\alpha} = U_{d/s}$ for intra-orbital $d_{x^2-y^2}$ and axial, and the inter-orbital component is $(\tilde{U}_{s,c})_{\alpha\alpha}^{\beta\beta} = V_{sd}$ ($\alpha \neq \beta$ are orbital indices).

The two-orbital model includes the Hund's physics. This is because the Hund's coupling gives the spin-spin interaction between different orbitals, whereas V_{sd} includes density-density interactions. Writing the total density operator $n = (n_{\uparrow} + n_{\downarrow})/2$ for up and down spins and expanding the second term in Eq.(4.3.1) term, we find that V_{sd} includes both spin-conserving and spin-flip interaction between the two orbitals. $\text{Tr } \tilde{\chi}_s$ in Fig. 4.3 and Fig. 4.4 includes both intra and inter-orbital contribution.

In Fig. 4.3 [(a)-(e)], we show the FS topology for NNO and LNO in Fig. 4.4 [(a)-(e)] at five k_z cuts, with the corresponding orbital weight indicated by red to

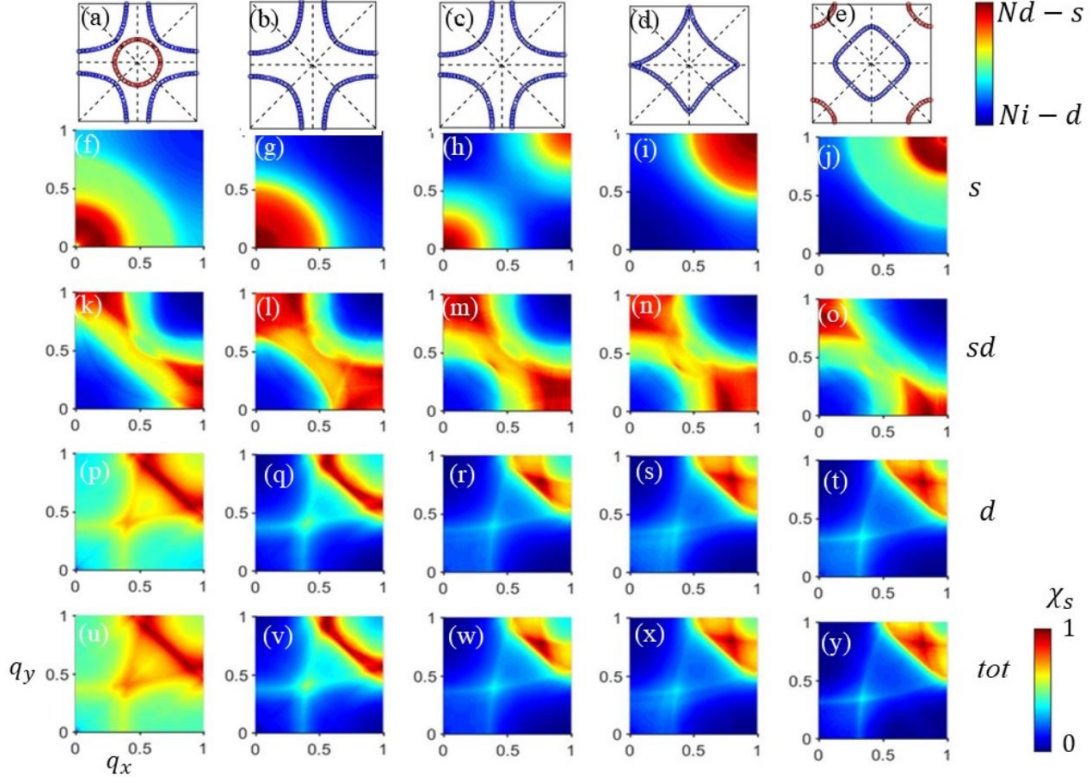


Figure 4.3: (a)-(e) FS topologies in NNO plotted as a function of $k_x - k_y$ [$-\pi \rightarrow \pi$ range] at $k_z = 0, \pi/4, \pi/2, 3\pi/4, \pi$. Blue (Ni $d_{x^2-y^2}$) to red (axial) colors depict the orbital contributions at each k_F . (f)-(j) Plots of static spin susceptibility for axial orbital. (k)-(o) Plots of static spin susceptibility for inter-orbital. (p)-(t) Plots of static spin susceptibility for d orbital. (u)-(y) Plots of static total [$\text{Tr } \tilde{\chi}_s$, summing over both intra- and inter-orbital contributions] channels. We calculate the spin susceptibility components at optimal (20 %) doping in NNO at $q_z = 0, \pi/4, \pi/2, 3\pi/4, \pi$ respectively, $q_x, q_y : 0 \rightarrow \pi$. All color bars are separately normalized for visualization.

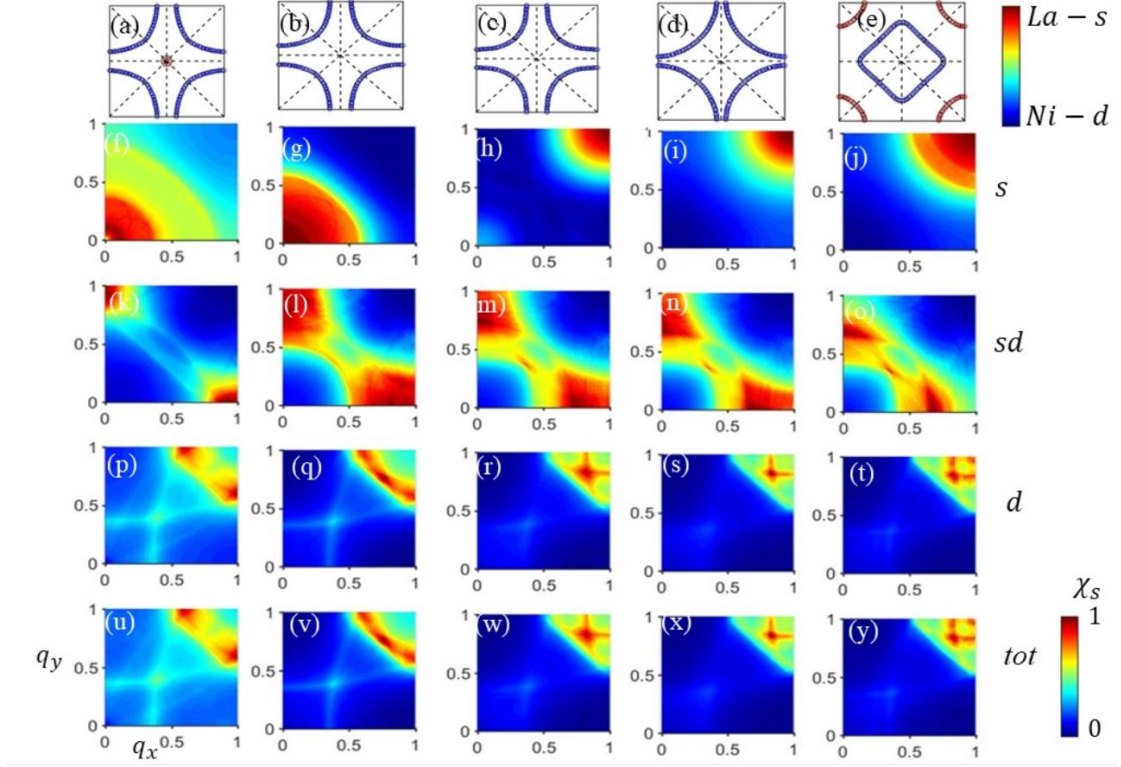


Figure 4.4: (a)-(e) FS topologies in LNO plotted as a function of $k_x - k_y$ [$-\pi \rightarrow \pi$ range] at $k_z = 0, \pi/4, \pi/2, 3\pi/4, \pi$. Blue (Ni $d_{x^2-y^2}$) to red (axial) colors depict the orbital contributions at each k_F . (f)-(j) Plots of static spin susceptibility for axial orbital. (k)-(o) Plots of static spin susceptibility for inter-orbital. (p)-(t) Plots of static spin susceptibility for d orbital. (u)-(y) Plots of static total [$\text{Tr } \tilde{\chi}_s$, summing over both intra- and inter-orbital contributions] channels. We calculate the spin susceptibility components at optimal (20 %) doping in LNO at $q_z = 0, \pi/4, \pi/2, 3\pi/4, \pi$ respectively, $q_x, q_y : 0 \rightarrow \pi$. All color bars are separately normalized for visualization.

blue color map. The FS-s are seen to be strongly 3D, which is typically detrimental for FS nesting strength. However, owing to the particular orbital weight distributions, there arise dominant nesting channels, which are highly orbital resolved. Interestingly, there is a complete orbital inversion among two FS sheets between $k_z = 0$ and π . While the large hole pocket centering the zone boundary, and electron pocket in zone center of NNO BZ is of Ni d ($d_{x^2-y^2}$) and axial character (s), respectively in $k_z = 0$, they reverse their roles in $k_z = \pi$.

The Ni d orbital enjoys a FS topology similar to the cuprates case in the low k_z region, giving a nearly 2D FS nesting feature around $\mathbf{Q} = (\pi, \pi, 0)$ and hence a $d_{x^2-y^2}$ -pairing symmetry. On the other hand, the axial orbital acquires a FS nesting, considerably weaker in strength compared to the Ni d orbital case, at $\mathbf{Q} = (\pi, \pi, \pi)$, which is responsible for the d_{z^2} type pairing symmetry. The FS for LNO, shown in Fig. 4.4 [(a)-(e)] is topologically similar to NNO, except it almost loses its FS pocket at the Γ -point. Since this heavily weakened FS pocket is dominated by axial orbital in NNO, the multi-band picture is less prominent in LNO. This is also reflected in the far weaker contribution of the inter-orbital susceptibility to be discussed in the following.

The orbital resolved spin susceptibility for NNO is shown in Fig. 4.3 [(f)-(y)] and LNO in Fig. 4.4 [(f)-(y)], at five q_z cuts, which highlights the importance of inter-orbital contribution. The relative contributions from axial orbital (s) and inter-orbital ($s-d$), compared to Ni d are found to be 1/10-th and 1/5-th, respectively. In comparison, in LNO, they are 1/100-th and 1/20-th, respectively. This makes the total susceptibility dominated almost entirely by the d -orbital contribution for LNO, while the significant inter-orbital orbital contribution makes the total susceptibility in NNO appreciably different from the d -orbital contribution (cf. Fig. 4.3[(p)-(t)] and Fig. 4.4 [(p)-(t)]).

4.3.2 Calculation of SC properties

In analogy with cuprates, [73] pnictides, [74] and HFSCs, [71] we assume superconductivity in the present compound is spin-fluctuation mediated. The estimated electron-phonon interaction turns out to be too small to support observed T_c . [204] Based on a two-band Hubbard model, we obtain the pairing potential by consid-

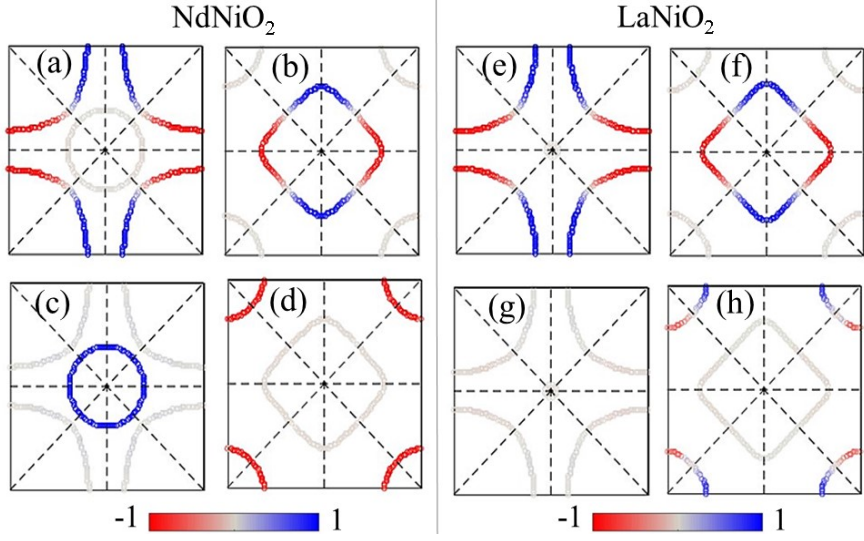


Figure 4.5: (Color online) Computed values of orbital resolved pairing eigenfunction $\Delta_\alpha(\mathbf{k})$ plotted on the FS at two representative cuts $k_z = 0$ [(a)-(c)], π [(b)-(d)] for NNO. [(a),(b)] and [(c),(d)] give orbital contributions for Ni $d_{x^2-y^2}$ and axial orbital, respectively. (e)-(h) Same as (a)-(d), but plotted for LNO.

ering the bubble and ladder diagrams, Eq. (1.6.24a) [73, 74, 71, 72]. The details of the formalism is given in Sec. 1.6.2. Application of a weak coupling theory may be justified by the fact that exchange-scale in nickelates are smaller than cuprates.

In Fig. 4.5 we plot the pairing eigenfunction $\Delta(\mathbf{k})$ for the highest eigenvalue λ , but projected onto the different orbital channels as $\Delta_{\alpha\beta} = \sum_\nu \Delta_\nu \phi_\nu^{\alpha*} \phi_\nu^\beta$ (\mathbf{k} dependence is suppressed for simplicity), where α, β are orbital indices, and ν is the band index. ϕ_ν^α is the eigenvector of the two-band Hamiltonian. In NNO, we clearly observe that the pairing symmetry of the Ni d orbital onto the FS is a pure $d_{x^2-y^2} = \cos k_x - \cos k_y$ type, with very little or no three dimensional component. On the other hand, the projected pairing symmetry on the axial orbital can be described by a simple k_z dispersion as $\cos k_z$, with no signature of the basal plane anisotropy. In contrast, in LNO compound, the axial orbital's contribution on the FS is drastically reduced, and hence the calculated pairing symmetry changes to a simple $d_{x^2-y^2}$. This result implies that the axial orbital, although seemingly has reduced weight on the FS, can play important role to determine the pairing symmetry.

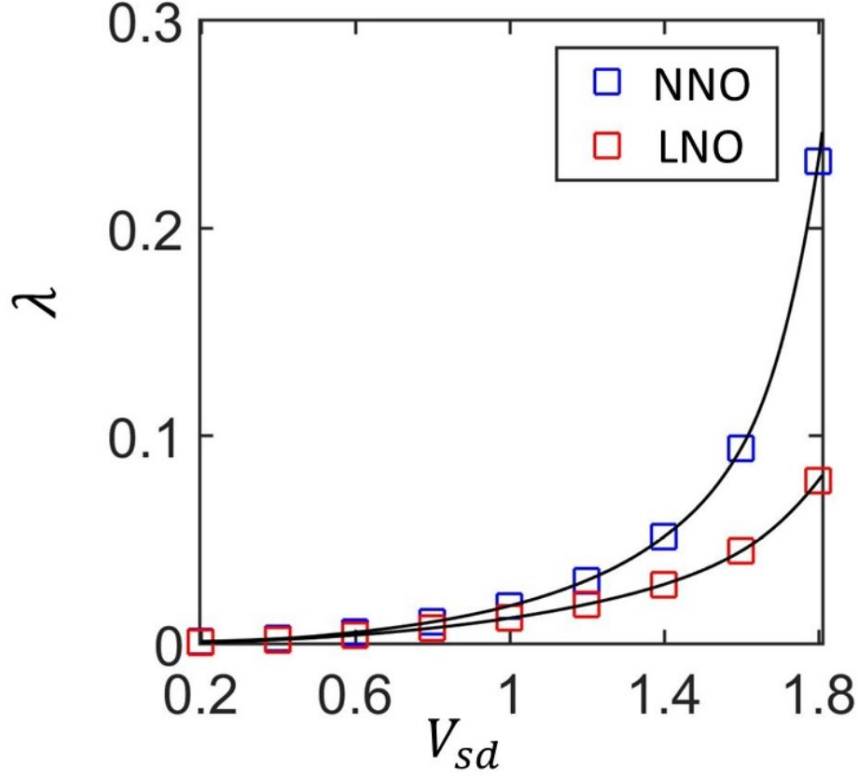


Figure 4.6: Evolution of SC coupling constant λ as a function of inter-orbital Hubbard interaction V_{sd} for choice of $U_d = 0.9$ eV and 0.6 eV for NNO and LNO. [206]

We study how the pairing strength λ depends on the choice of Hubbard interaction parameters, U_s , U_d and V_{sd} , which unravels as interesting scenario. Firstly, focusing on NNO, we find that λ increases almost exponentially with V_{sd} (cf. Fig. 4.6), while neither U_d or U_s is effective in enhancing λ [see Fig. 4.7] [206]. Thus, an appreciable λ is obtained only when V_{sd} becomes appreciable. Secondly, relative to NNO, the pairing strength grows much more slowly with V_{sd} in LNO. Thus even for appreciable value of V_{sd} , the pairing strength in LNO is much smaller than NNO. This in turn highlights the important role of the inter-orbital interaction V_{sd} for superconductivity in nickelate compounds under discussion, and their material dependence. The importance of inter-orbital interaction is supported by the spectroscopic data [63] as well as found in a recent DFT+DMFT study [207] on $\text{Nd}_{1-x}\text{Sr}_x\text{NiO}_2$.

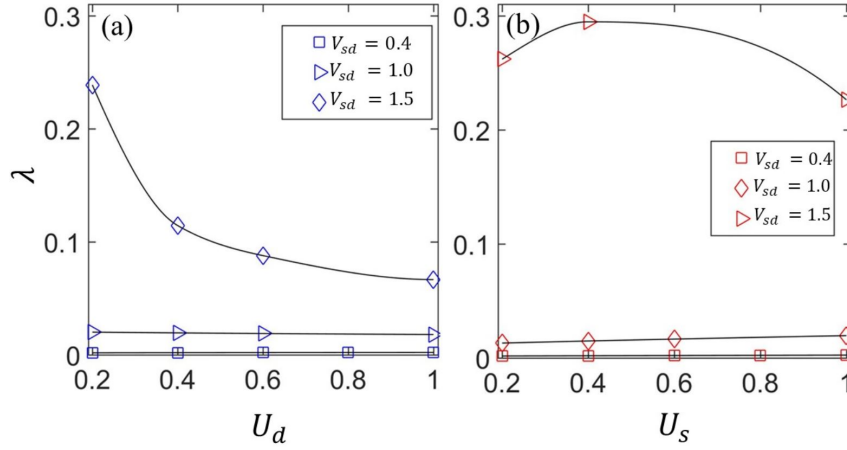


Figure 4.7: (a) SC coupling constant λ as a function of intra-orbital Hubbard interaction U_d (blue) for choice of $U_s = 0.6$ eV (square), 0.8 eV (triangle) and 0.8 eV (diamond) for NNO. (b) shows the variation of λ as a function of intra-orbital interactions U_s (red) for NNO for choice of $U_d = 1$ eV (square), 0.95 eV (diamond) and 0.95 eV (triangle). [206]

4.3.3 Spectral function

We consider the Nambu spinor basis, $\psi_{\mathbf{k}} = \left(c_{1\mathbf{k}\uparrow}, c_{2\mathbf{k}\uparrow}, c_{1-\mathbf{k}\downarrow}^\dagger, c_{2-\mathbf{k}\downarrow}^\dagger \right)^T$, to calculate the spectral function and DOS. The SC gap functions are,

$$\Delta_s = \langle c_{1-\mathbf{k}\downarrow} c_{1\mathbf{k}\uparrow} \rangle = \Delta_s^0 \cos(k_z), \quad \Delta_d = \langle c_{2-\mathbf{k}\downarrow} c_{2\mathbf{k}\uparrow} \rangle = \Delta_d^0 (\cos(k_x) - \cos(k_y)), \quad (4.3.2)$$

where, Δ_s and Δ_d are SC gap for axial orbital and $d_{x^2-y^2}$ orbital respectively. The scanning tunnelling measurement (STM) performed on NNO gives two type of SC gap with maximum values, 2.35 meV for Δ_s^0 and 3.9 meV for Δ_d^0 [208].

The Hamiltonian in the mean-field theory is given as,

$$H = \begin{pmatrix} \xi_s(\mathbf{k}) & 0 & \Delta_s(\mathbf{k}) & 0 \\ 0 & \xi_d(\mathbf{k}) & 0 & \Delta_d(\mathbf{k}) \\ \Delta_s^*(\mathbf{k}) & 0 & -\xi_s(-\mathbf{k}) & 0 \\ 0 & \Delta_d^*(\mathbf{k}) & 0 & -\xi_d(-\mathbf{k}) \end{pmatrix}. \quad (4.3.3)$$

The Green's function is given in Eq. (1.6.21). We analytically continue to real

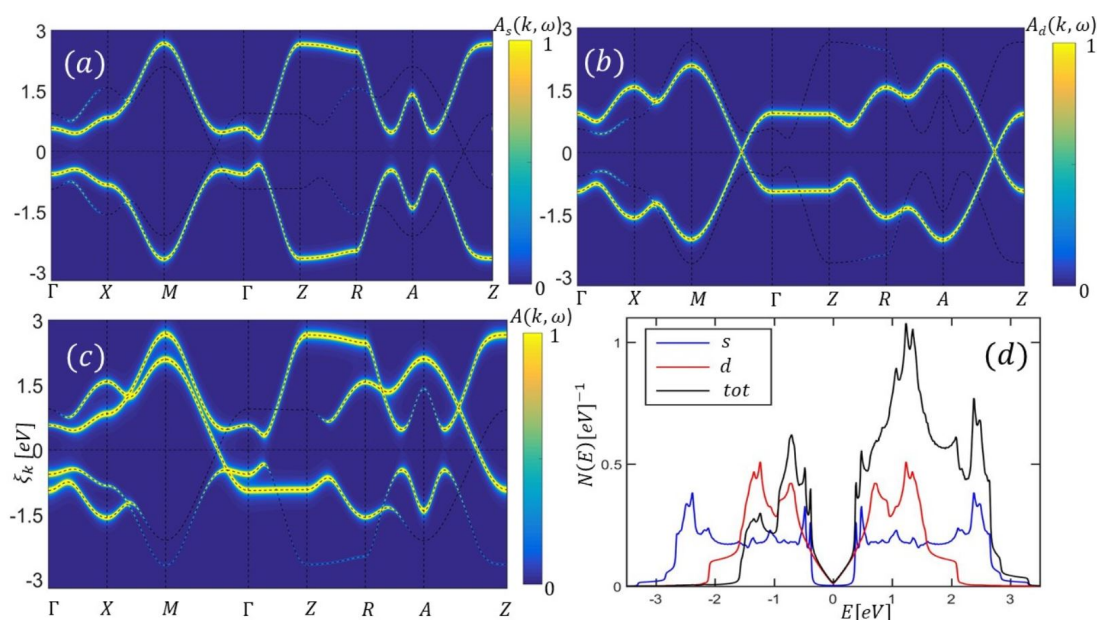


Figure 4.8: Calculation of \mathbf{k} -resolved spectral function along the high-symmetry points in the BZ. (a) is the spectral function for Nd s -orbital, (b) is the spectral function for Ni $d_{x^2-y^2}$ -orbital, (c) is the total spectral function. (d) Orbital resolved DOS for Δ_d (red) and Δ_s (blue) gap function. Total DOS is denoted by black line.

frequency (ω) axis, $ik_n \rightarrow \omega + i\delta$; δ is a small number. The spectral functions is given by the imaginary part of the Green's function,

$$A(\mathbf{k}, \omega) = -\frac{1}{\pi} \text{Im} \left[\frac{1}{(\omega + i\delta)I - H} \right], \quad (4.3.4)$$

where, I is the 4×4 identity matrix. Total DOS is given by, $N(\omega) = \sum_{\mathbf{k}} A(\mathbf{k}, \omega)$. The orbital-resolved DOS for axial orbital is, $N_s(\omega) = \frac{1}{2} \left(N_{11}(\omega) + N_{33}(\omega) \right)$, and for Ni d orbital, $N_d(\omega) = \frac{1}{2} \left(N_{22}(\omega) + N_{44}(\omega) \right)$.

In Fig. 4.8 [(a)-(c)] we calculate the spectral function along the high symmetry points of the BZ for NNO at the optimal doping. The DOS is shown in Fig. 4.8 (d).

Experimental signature: The STM performed on NNO by Gu *et. al.* [208] reporting a two-gap scenario as proposed in this work. The two-gap behaviour, with one nodeless and another nodal gap as observed in different regions of the sample, is fully consistent with our proposal of a d_{z^2} (nodeless due to corresponding FS topology) and $d_{x^2-y^2}$ (nodal) in axial with dominant portion of weight on Nd, and Ni- d orbitals, respectively, which are individually observed when the tunnelling tip appears on top of corresponding atoms.

4.4 Doping dependence

The origin of possible differential behavior of LNO and NNO intriguing. The natural question is how does this materials specific electronic structure influence the SC state in this family? The ionic radius [209] of La^{3+} is 104 pm \approx 4% larger than the ionic radius of Nd^{3+} (100 pm), resulting in an expanded lattice of volume \approx 5% in LNO compared to NNO.[190, 60] Such structural differences may influence the electronic behavior, though this has not been investigated. On the other hand, it has been suggested[210] that direct hybridization with the Nd $4f$ states may become important for the description of electronic structure of NNO near the chemical potential. It is to be noted that the spin disorder broadening induced by such direct hybridization is expected to play a detrimental role in superconductivity rather than helping it. Very similar values of T_c for NNO and

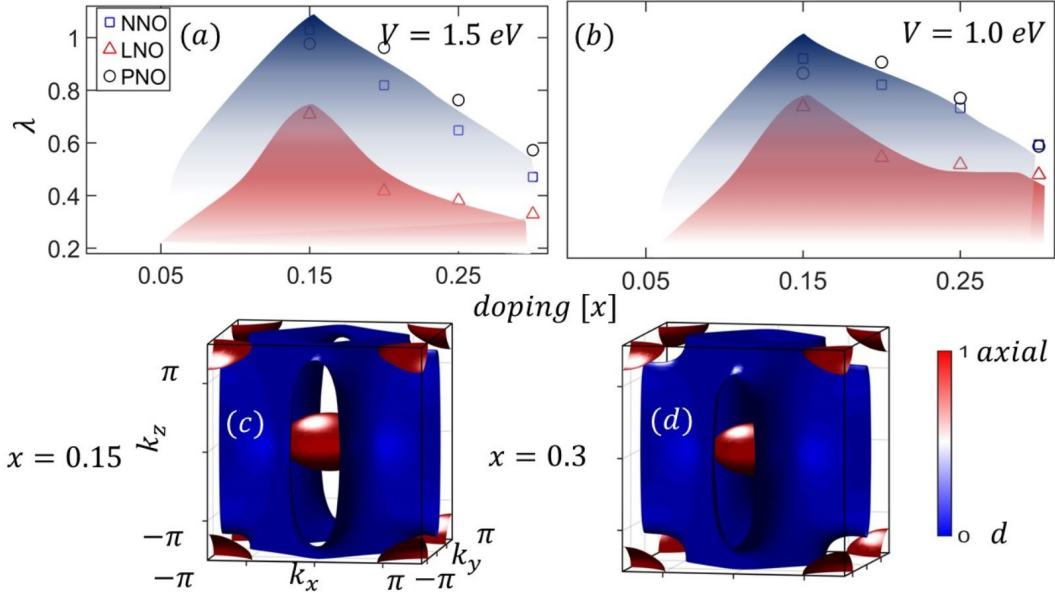


Figure 4.9: (a)-(b) Doping dependent SC coupling constant λ (scaled by the strength of maximum λ for NNO) for three different materials for choice of $V = 1.5$ eV (a) and $V = 1.0$ eV (b). The shaded regions are the guide to the eyes. Due to the limitations of weak coupling theory, the shaded area for $x < 0.15$ are only schematic construction. (c)-(d) FS for NNO at two dopings, (c) at $x = 0.15$ and (d) at $x = 0.3$. The orbital contributions are denoted in the colormap.

PNO, despite Nd^{3+} having a f -electron count of 3 and Pr^{3+} having a f -electron count of 2, raises questions on the active role of f -electrons on the electronic behaviour and consequent SC properties of NNO and PNO. This leaves the role of $4f$ electrons an open issue. On the other hand, it is interesting to note that while the ground state for the quasi-2D reduced trilayer nickelate $\text{La}_4\text{Ni}_3\text{O}_8$ is a charge density-wave insulator,[211] that of $\text{Pr}_4\text{Ni}_3\text{O}_8$ [212] is metallic, implying the difference between the La and Pr systems manifests not only in case of infinite-layer 2D compounds, but also for quasi-2D compounds.

Calculation of doping dependence of pairing eigenvalue

The highest pairing eigenvalue of Eq. (1.6.29) gives a two-dimensional $d_{x^2-y^2}$ symmetry gap in the Ni d orbital channel. The $d_{x^2-y^2}$ -wave state results from the

antiferromagnetic $\mathbf{Q} = (\pi, \pi)$ nesting between the two hot-spots across the BZ for the hole pocket (near the $k_z = 0$ plane). The observed three-dimensionality of the hole-pocket clearly weakens the nesting strength and brings in doping dependence. All three compounds have similar hole pocket [see Fig. 4.2 (g)-(i)] and hence gives a $d_{x^2-y^2}$ - wave solution. For NNO and PNO, there exists large area FS electron pockets α (centered around the Γ -point) which opens up another nesting channel between the α and γ (centered around the A -point) electron pockets, contributed by axial orbital, and offers an additional pairing channel which is of d_{z^2} -wave symmetry. This is nearly absent in LNO due to diminishing presence of electron pocket at Γ . Thus superconductivity in NNO and PNO is of two gap nature, while a single gap superconductivity is found in LNO. Furthermore, having a second pairing channel with a symmetry that is consistent with the corresponding FS nesting, enhances the SC coupling constant λ in NNO and PNO, compared to LNO.

In Fig. 4.9 [(a)-(b)], we plot the calculated values of λ contributed by all channels, as a function of doping for the three compounds. The solution of gap equation shows that the pairing symmetry for NNO and PNO remains of two gap nature throughout the doping range, while that of LNO remains predominantly a single d -wave gap SC. The added contribution of two channels of pairing in NNO and PNO, as opposed to a nearly single channel SC in LNO, makes the pairing strength in about twice larger in NNO/PNO compared to LNO in almost the entire doping range.

Further, as seen in Fig. 4.9 [(a)-(b)], λ decreases monotonically with doping for all three compounds. Doping dependent calculations are carried out for two choices of $V = 1.5$ eV and 1.0 eV with $U=1, 0.5$ eV for the Ni d and axial orbitals, respectively. We find that the qualitative features remain unchanged upon change of V_{sd} value. Thus, the doping dependence arises purely due to changes in electronic structure, and guided by how the FS volume, FS nesting and the associated orbital weight evolve with doping.

The origin of decreasing strength of SC with doping can be traced back to the FS area and nesting strength. As seen from the orbital resolved DOS in Fig. 4.2 [(d)-(f)]; with hole doping, the DOS of the Ni $d_{x^2-y^2}$ orbital increases, while that of the axial orbital decreases. There is a van-Hove singularity (VHS) of the $d_{x^2-y^2}$ which lies below the Fermi level, as in cuprates, however, this VHS cannot be doped

within the experimentally feasible range. In a simple BCS like picture, one would thus expect the SC strength to increase with hole doping due to the increment of DOS. However, contrary to this, superconductivity is found to decrease with doping.

To find out the reason behind this, we probe the 3D FS topology and the orbital weight distributions for the representative case of NNO in Fig. 4.9 [(c)-(d)] at two characteristic dopings ($x = 0.15$ and $x = 0.3$). The FS evolution between these two dopings is monotonic, and there is no significant change in the FS topology across this doping range. The large FS, which is dominated by the Ni d orbital (blue color) has an interesting transition from the hole-like FS (as in underdoped cuprates) near $k_z = 0$ to an electron-like FS (as in overdoped cuprates) near $k_z = \pi$ plane. The transition occurs close to the $k_z = \pi$ plane and this transition point moves towards the $k_z = 0$ planes with increasing hole doping. In other words, the hole-pocket become more three-dimensional with increasing doping and this makes a difference in the FS nesting at $\mathbf{Q} = (\pi, \pi)$. As the area of the hole-like FS topology reduces with doping, the FS nesting strength at \mathbf{Q} also gradually reduces. Thus, the SC strength decreases monotonically. On the other hand, for NNO/PNO the electron-pocket size decreases with hole doping and hence both its nesting strength and the contributions to λ from its DOS decreases. In essence, the SC coupling constant for the d_{z^2} also decreases with doping.

Our theory reproduces the right-hand side of the SC dome, as observed in NNO as well as in PNO, [64, 58] The decrease of λ at lower doping is not obtained in our model, since our theory does not include the renormalization effects on the quasiparticle spectrum due to many-body interaction. It is known experimentally that the low-doping region is a correlated metal or weak insulator [64, 58] and hence indicating the important role of correlation which quenches the SC coupling constant. [80, 3]

4.5 Discussions and Conclusions

Motivated by the recent discovery of superconductivity in NNO [59] and in PNO [198] with very similar transition temperatures, we investigate the role of non-zero f -ness of Nd and Pr compounds, as superconductivity has not yet been observed

in another infinite-layer nickelate LNO, containing f^0 La. While the active role of f electrons is debated, we discuss the role of f electrons in influencing the positions of $5d$ levels of rare-earth elements, thereby dictating the nature of axial orbitals contributing to the second band that crosses the Fermi level. This provides subtle differences between the FS topology of the Pr and Nd compounds, and that of La compounds, driving the two-gap superconductivity in Pr and Nd compounds as opposed to a single gap in La compound. Interestingly the doping-dependent superconductivity shows a factor of two suppression in the strength of superconductivity in La compound, as compared to that of Nd and Pr compounds.

Note, our calculation and analysis does not include the effect of magnetism of $4f$ electrons. However, the fact that the difference and similarity of the three compounds have been brought out correctly, suggests the role of the f electrons, as identified in the present study, to be the dominant one.

In summary, motivated by the two-band scenario,[63, 199, 213] proposed for $R\text{NiO}_2$ ($R = \text{La, Nd}$), we use a two-band Hamiltonian from the DFT calculations [202, 203]. DFT correctly captures the low energy features of electronic structure. The DMFT study [214] on $\text{Nd}_{1-x}\text{Sr}_x\text{NiO}_2$ found that at low energy the quasi-particle spectra is well defined. So weak coupling approximation in the spin fluctuation theory is applicable in the infinite-layer nickelates. The axial orbital from a combination of Nd/La d , Ni $3d_{z^2}$ and Ni s , and encodes the materials dependence. We did full 3D calculations in obtaining the pairing symmetry of infinite-layer nickelates. But for the ease of presentation, we only show pairing eigenfunctions at particular k_z cuts. Calculation of FS properties in such a two-orbital picture, shows an orbital selective pairing for the Nd compound, while it is found to be only of $d_{x^2-y^2}$ symmetry in La compound. Most importantly, we find while the SC pairing grows almost in an exponential fashion with inter-orbital Hubbard interaction for the Nd compound, it is not helped by the choice of intra-orbital Hubbard interactions. We note that V_{sd} effectively also includes the Hund's coupling. We believe due to the combined effects of Hund's physics and charge screenings enhanced by V_{sd} ,[206] the effect of intra-orbital Coulomb repulsions U_i 's are superseded by the inter-orbital interaction V_{sd} in these compounds. Though the same holds good for La compound, the growth of pair interaction with the strength of inter-orbital

Hubbard interaction is much weaker than in Nd compound, presumably justifying the fact that superconductivity has been so far observed only for the Nd compound.[59, 213]

Chapter 5

Conclusions

In conclusion, I have used analytical and numerical methods to study the superconducting mechanism and properties in HF, transition-metal oxides YBCO, $R\text{NiO}_2$ ($R = \text{Nd, Pr, La}$). For the HF system, I proposed a new mechanism of SC starting from the impurity electron (f) and conduction electron (c). Here, in the strong correlation limit, by removing the doubly occupation f -electron, I obtained an effective, attractive interaction between f and c -electrons. This leads to a fully gapped, constant sign s -wave pairing in the HF systems. The new pairing is an inter-orbital pairing and the Cooper pair's center-of-mass momenta can have all possible values, instead of zero (BCS) or fixed value (FFLO).

Experimentally the overwhelming evidence of conventional SC in HF is consistent with this pairing mechanism. The T^3 dependence of $1/T_1$ relaxation rate in NQR and the four-fold modulation of H_{c2} can be explained within this two-orbital model. Observed spin resonance gap at energy scale $2\Delta^2/\bar{\xi}_f$ also validates our theory. Following that, we obtain a relation between Kondo temperature and SC T_c , under the assumption of isotropic $v_{\mathbf{k}}$. However, for the non-isotropic case, this theory can be generalised by replacing $v_{\mathbf{k}}$ by its value at the Fermi level, $\langle v_{\mathbf{k}} \rangle_{FS}$.

In transition-metal oxide superconductors, using a spin-fluctuation mediated pairing mechanism, I obtained a new pairing symmetry in the YBCO system and an orbital selective superconductivity in $R\text{NiO}_2$. In contrast with HF system, here

the pairing symmetry governed by spin and charge fluctuations channel, and this will lead to a unconventional superconductivity. For YBCO, I found an unusual f -wave pairing at low doping of chain states. This doping regime usually not accessible to normal experimental conditions. However, d -wave pairing can be found by changing the chain doping while keeping the plane state at optimal doping. Both pairing symmetries give nodal quasi-particles spectrum in the DOS, however, the gap nodes are aligned along with the BZ boundary directions for the f -wave case, while it is aligned to the diagonal direction in the d -wave case. The f -wave pairing symmetry can also be detected by the field-angle dependence of the transport and thermodynamical quantities.[103] Moreover, the anisotropy in the upper critical field in the vortex phase have unique signatures for the f -wave pairing as discussed in the context of UPt₃ superconductors.[182].

In RNiO₂, I explored superconductivity in NNO, PNO, LNO employing a first-principles derived low-energy model Hamiltonian, consisting of two orbitals: Ni $d_{x^2-y^2}$, and an axial orbital. The axial orbital is constructed out of Nd/La d , Ni $3d_{z^2}$ and Ni s characters. Calculation of the superconducting pairing symmetry and pairing eigenvalue of the spin-fluctuation mediated pairing interaction underlines the crucial role of inter-orbital Hubbard interaction in superconductivity, which turns out to be orbital-selective. The axial orbital brings in materials dependence in the problem, making NNO, PNO different from LNO, thereby controlling the inter-orbital Hubbard interaction assisted superconductivity.

The $d_{x^2-y^2}$ -wave gap gives a nodal quasi-particle DOS while the d_{z^2} -wave gap symmetry becomes node-less as it originates from the axial orbital, which primarily contributes in the α and γ FS pockets, and has no contribution in $k_z = \pi/2$. This finding corroborates the recent STM data on NNO.[132]

Appendix A

S-matrix expansion of the Kondo model

Dyson equation

The Kondo Hamiltonian is given by,

$$\begin{aligned} H_K &= \sum_{\mathbf{k}\sigma} \xi_{\mathbf{k}} c_{\mathbf{k}\sigma}^\dagger c_{\mathbf{k}\sigma} + \sum_{\mathbf{k}, \mathbf{k}'} J_K(\mathbf{k}, \mathbf{k}') \vec{S}_f \cdot \vec{S}_c(\mathbf{k}, \mathbf{k}'), \\ &= H_0 + V, \end{aligned} \quad (\text{A.0.1})$$

where the Kondo coupling J_K is 1.3.8 ,

$$J_K(\mathbf{k}, \mathbf{k}') = v_{\mathbf{k}} v_{\mathbf{k}'} \left[\frac{1}{\xi_f + U - \xi_{\mathbf{k}}} + \frac{1}{\xi_{\mathbf{k}} - \xi_f} + \frac{1}{\xi_f + U - \xi_{\mathbf{k}'}} + \frac{1}{\xi_{\mathbf{k}'} - \xi_f} \right]. \quad (\text{A.0.2})$$

H_0 is non interacting Hamiltonian, which includes the kinetic energy of the conduction electron of energy $\xi_{\mathbf{k}}$, $c_{\mathbf{k},\sigma}$, $c_{\mathbf{k},\sigma}^\dagger$ is the anihilation and creation operator respectively.

V is the perturbation which includes the interaction between spin of the conduction electron \vec{S}_c and spin of the impurity \vec{S}_f .

$\vec{S}_f = \sum_{m,m'=-J}^{+J} f_m^\dagger \vec{\Gamma}_{m,m'} f_{m'}$ (J is the multiplets of impurity electrons) and $\vec{S}_c(\mathbf{k}, \mathbf{k}') = \sum_{\alpha\beta=\uparrow\downarrow} c_{\mathbf{k}\alpha}^\dagger \vec{\sigma}_{\alpha\beta} c_{\mathbf{k}'\beta}$ are the spin of impurity electron and conduction electron level. $\vec{\Gamma}, \vec{\sigma}$ are the spin matrices.

For simplicity we assume that the spin of the impurity electron is, $J = \frac{1}{2}$ and Kondo coupling is momentum independent, $J_K(\mathbf{k}, \mathbf{k}') = J_K$.

$\vec{\Gamma}$, and $\vec{\sigma}$ are Pauli matrices. Many body Green's function of the conduction electron is,

$$\begin{aligned} \mathcal{G}_c(\mathbf{k}, \mathbf{k}', \sigma, \sigma', \tau, \tau') &= -\left\langle T_\tau \left[c_{\mathbf{k}, \sigma}(\tau) c_{\mathbf{k}', \sigma'}^\dagger(\tau') \right] \right\rangle, \\ &= -\sum_{n=0}^{\infty} (-1)^n \int_0^\beta d\tau_1 \dots \int_0^\beta d\tau_n \left\langle T_\tau c_{\mathbf{k}, \sigma}(\tau) V(\tau_1) \dots V(\tau_n) c_{\mathbf{k}', \sigma'}^\dagger(\tau') \right\rangle. \end{aligned} \quad (\text{A.0.3})$$

We only consider the connected diagrams in the expectation value, $\langle \dots \rangle$, [30, 21].

Since the free Hamiltonian is isotropic in spin, $\langle S_c \rangle = 0$. Hence first non trivial term is second order term.

$$\begin{aligned} \mathcal{G}_c^{(2)}(\mathbf{k}, \mathbf{k}', \sigma, \sigma', \tau, \tau') &= -\sum_{\substack{\mathbf{k}_1, \mathbf{k}_2 \\ \mathbf{k}'_1, \mathbf{k}'_2}} J_K^2 \int_0^\beta d\tau_1 d\tau_2 \left\langle c_{\mathbf{k}, \sigma}(\tau) \vec{S}_c^i(\mathbf{k}_1, \mathbf{k}'_1)(\tau_1) \right. \\ &\quad \left. \vec{S}_c^j(\mathbf{k}_2, \mathbf{k}'_2)(\tau_2) c_{\mathbf{k}', \sigma'}^\dagger(\tau') \right\rangle \left\langle \vec{S}_f^i(\tau_1) \vec{S}_f^j(\tau_2) \right\rangle, \end{aligned} \quad (\text{A.0.4})$$

i, j are the spin level at time τ_1, τ_2 respectively. We use following properties of the Pauli matrices,

$$\text{Tr}(\sigma_a) = 0, \quad (\text{A.0.5})$$

$$\text{Tr}(\sigma_a \sigma_b) = 2\delta_{ab}, \quad (\text{A.0.6})$$

$$\text{Tr}(\sigma_a \sigma_b \sigma_c) = 2i\epsilon_{abc}, \quad (\text{A.0.7})$$

where a, b, c can take any value of (x, y, z). $\langle \vec{S}_f^i(\tau_1) \vec{S}_f^j(\tau_2) \rangle = \frac{\delta_{ij}}{2}$. We use the form of spin operator into Eq. (A.0.4),

$$\begin{aligned}
\mathcal{G}_c^{(2)}(\mathbf{k}, \mathbf{k}', \sigma, \sigma', \tau, \tau') &= - \sum_{\substack{\mathbf{k}_1, \mathbf{k}_2 \\ \mathbf{k}'_1, \mathbf{k}'_2}} J_K^2 \sum_{\substack{\alpha_1 \beta_1 \\ \alpha_2 \beta_2}} \int_0^\beta d\tau_1 d\tau_2 \langle c_{\mathbf{k}, \sigma}(\tau) c_{\mathbf{k}_1 \alpha_1}^\dagger(\tau_1) \vec{\sigma}_{\alpha_1 \beta_1}^i c_{\mathbf{k}'_1 \beta_1}(\tau_1) \\ &\quad c_{\mathbf{k}_2 \alpha_2}^\dagger(\tau_2) \vec{\sigma}_{\alpha_2 \beta_2}^j c_{\mathbf{k}'_2 \beta_2}(\tau_2) c_{\mathbf{k}', \sigma'}^\dagger(\tau') \rangle \langle \vec{S}_f^i(\tau_1) \vec{S}_f^j(\tau_2) \rangle, \\
&= \sum_{\mathbf{k}_1} J_K^2 \sum_{\alpha_1 \beta_1} \int_0^\beta d\tau_1 d\tau_2 \mathcal{G}_c^0(\mathbf{k}, \sigma, \tau - \tau_1) \mathcal{G}_c^0(\mathbf{k}_1, \alpha_1, \tau_1 - \tau_2) \\
&\quad \mathcal{G}_c^0(\mathbf{k}', \sigma', \tau_2 - \tau') \langle \vec{\sigma}_{\sigma \beta_1}^i \vec{\sigma}_{\beta_1 \sigma'}^j \rangle \frac{\delta_{ij}}{2}, \\
&= \frac{3J_K^2}{4} \sum_{\mathbf{k}_1, \sigma_1} \int_0^\beta d\tau_1 d\tau_2 \mathcal{G}_c^0(\mathbf{k}, \sigma, \tau - \tau_1) \mathcal{G}_c^0(\mathbf{k}_1, \sigma_1, \tau_1 - \tau_2) \\
&\quad \mathcal{G}_c^0(\mathbf{k}', \sigma', \tau_2 - \tau'),
\end{aligned} \tag{A.0.8}$$

where, in the last line of Eq. (A.0.8) we replace α_1 by σ_1 , and use Eq. (A.0.6). Dyson equation for self energy is given by,

$$\begin{aligned}
\mathcal{G}_c(\mathbf{k}, \mathbf{k}', \sigma, \sigma', \tau, \tau') &= \mathcal{G}_c^0(\mathbf{k}, \sigma, \tau - \tau') \delta_{\mathbf{k}, \mathbf{k}'} \delta_{\sigma, \sigma'} + \int_0^\beta d\tau_1 d\tau_2 \left[\mathcal{G}_c^0(\mathbf{k}, \sigma, \tau - \tau_1) \right. \\
&\quad \left. \Sigma_c(\mathbf{k}, \mathbf{k}', \sigma, \sigma', \tau_1, \tau_2) \mathcal{G}_c^0(\mathbf{k}', \sigma', \tau_2 - \tau') \right].
\end{aligned} \tag{A.0.9}$$

The second order self-energy is given by

$$\Sigma_c^{(2)}(\mathbf{k}, \mathbf{k}', \sigma, \sigma', \tau_1, \tau_2) = \frac{3J_K^2}{4} \sum_{\mathbf{k}_1, \sigma_1} \mathcal{G}_c^0(\mathbf{k}_1, \sigma_1, \tau_1 - \tau_2) + O(J_K^3) \tag{A.0.10}$$

We will now consider third order of S-matrix ,

$$\begin{aligned}
\mathcal{G}_c^{(3)}(\mathbf{k}, \mathbf{k}', \sigma, \sigma', \tau, \tau') &= \sum_{\substack{\mathbf{k}_1, \mathbf{k}_2, \mathbf{k}_3 \\ \mathbf{k}'_1, \mathbf{k}'_2, \mathbf{k}'_3}} J_K^3 \int_0^\beta d\tau_1 d\tau_2 d\tau_3 \langle c_{\mathbf{k}, \sigma}(\tau) \vec{S}_c^i(\mathbf{k}_1, \mathbf{k}'_1)(\tau_1) \vec{S}_c^j(\mathbf{k}_2, \mathbf{k}'_2)(\tau_2) \\ &\quad \vec{S}_c^k(\mathbf{k}_3, \mathbf{k}'_3)(\tau_3) c_{\mathbf{k}', \sigma'}^\dagger(\tau') \rangle \langle \vec{S}_f^i(\tau_1) \vec{S}_f^j(\tau_2) \vec{S}_f^k(\tau_3) \rangle.
\end{aligned} \tag{A.0.11}$$

The self-energy depends upon time difference as we found in second order term

Substituting Eq. (A.0.12) in Eq. (A.0.13)

$$\begin{aligned}
\mathcal{G}_c^{(3)}(\mathbf{k}, \mathbf{k}', \sigma, \sigma', \tau, \tau') &= \sum_{\substack{\mathbf{k}_1, \mathbf{k}_2, \mathbf{k}_3 \\ \mathbf{k}'_1, \mathbf{k}'_2, \mathbf{k}'_3}} J_K^3 \sum_{\substack{\alpha_1 \alpha_2 \alpha_3 \\ \beta_1 \beta_2 \beta_3}} \int_0^\beta d\tau_1 d\tau_2 \left\langle c_{\mathbf{k}, \sigma}(\tau) c_{\mathbf{k}_1 \alpha_1}^\dagger(\tau_1) c_{\mathbf{k}'_1 \beta_1}(\tau_1) \right. \\
&\quad \left. c_{\mathbf{k}_2 \alpha_2}^\dagger(\tau_2) c_{\mathbf{k}'_2 \beta_2}(\tau_2) c_{\mathbf{k}_3 \alpha_3}^\dagger c_{\mathbf{k}'_3 \beta_3} c_{\mathbf{k}', \sigma'}^\dagger(\tau') \right\rangle \\
&\quad \left\langle \vec{\sigma}_{\alpha_1 \beta_1}^i \vec{\sigma}_{\alpha_2 \beta_2}^j \vec{\sigma}_{\alpha_3 \beta_3}^k \right\rangle \frac{2i\epsilon_{ijk}}{8} \text{sgn}(\tau_1 - \tau_2), \\
&= - \sum_{\mathbf{k}_2, \mathbf{k}_3} \sum_{\alpha_2, \alpha_3} \frac{3J_K^3}{8} \int_0^\beta d\tau_1 d\tau_2 \mathcal{G}_c^0(\mathbf{k}, \sigma, \tau - \tau_1) \mathcal{G}_c^0(\mathbf{k}_2, \alpha_2, \tau_1 - \tau_2) \\
&\quad \mathcal{G}_c^0(\mathbf{k}_3, \alpha_3, \tau_2) \mathcal{G}_c^0(\mathbf{k}', \sigma', -\tau') \text{sgn}(\tau_1 - \tau_2).
\end{aligned} \tag{A.0.14}$$

Comparing with Eq. (A.0.9) we obtain we the third order self energy,

$$\Sigma_c^{(3)}(\mathbf{k}, \mathbf{k}', \sigma, \sigma', \tau_1) = -\frac{3J_K^3}{8} \sum_{\mathbf{k}_1, \mathbf{k}_2} \sum_{\sigma_1, \sigma_2} \int_0^\beta d\tau_2 \mathcal{G}_c^0(\mathbf{k}_1, \sigma_1, \tau_1 - \tau_2) \mathcal{G}_c^0(\mathbf{k}_2, \sigma_2, \tau_2) \text{sgn}(\tau_1 - \tau_2). \tag{A.0.15}$$

Using Fourier transform in Matsubara frequency space we obtain,

$$\Sigma_c^{(3)}(\mathbf{k}, \mathbf{k}', \sigma, \sigma', ik_n) = \int_0^\beta d\tau_1 \Sigma_c^{(3)}(\mathbf{k}, \mathbf{k}', \sigma, \sigma', \tau_1) e^{ik_n \tau_1}. \tag{A.0.16}$$

The sgn function is defined as, $\text{sgn}(\tau_1 - \tau_2) = \Theta(\tau_1 - \tau_2) - \Theta(\tau_2 - \tau_1)$. Therefore,

third order term of the self-energy is, Eq. (A.0.15),

$$\begin{aligned}
\Sigma_c^{(3)}(\mathbf{k}, \mathbf{k}', \sigma, \sigma', ik_n) &= -\frac{3J_K^3}{8} \sum_{\mathbf{k}_1, \mathbf{k}_2} \sum_{\sigma_1, \sigma_2} \int_0^\beta d\tau_1 d\tau_2 \mathcal{G}_c^0(\mathbf{k}_1, \sigma_1, \tau_1 - \tau_2) \mathcal{G}_c^0(\mathbf{k}_2, \sigma_2, \tau_2) \\
&\quad \left[\Theta(\tau_1 - \tau_2) - \Theta(\tau_2 - \tau_1) \right] e^{ik_n \tau_1}, \\
&= -\frac{3J_K^3}{8} \sum_{\mathbf{k}_1, \mathbf{k}_2} \sum_{\sigma_1, \sigma_2} \int_0^\beta d\tau_1 d\tau_2 \left[\frac{1}{\beta} \sum_{p_n} e^{-ip_n(\tau_1 - \tau_2)} \mathcal{G}_c^0(\mathbf{k}_1, \sigma_1, ip_n) \right] \\
&\quad \left[\frac{1}{\beta} \sum_{q_n} e^{-iq_n(\tau_2)} \mathcal{G}_c^0(\mathbf{k}_2, \sigma_2, iq_n) \right] \left[\frac{1}{\beta} \sum_{r_n} \mathcal{G}_c^0(\mathbf{k}_2, ir_n) e^{-ir_n(\tau_2 - \tau_1)} \right] e^{ik_n \tau_1} \\
&\quad - \left[\tau_2 \rightarrow \tau_1 \right], \\
&= -\frac{3J_K^3}{8\beta^3} \sum_{\mathbf{k}_1, \mathbf{k}_2} \sum_{\sigma_1, \sigma_2} \sum_{p_n} \mathcal{G}_c^0(\mathbf{k}_1, ip_n) \mathcal{G}_c^0(\mathbf{k}_2, ik_n) \mathcal{G}_c^0(\mathbf{k}_2, ip_n - ik_n).
\end{aligned} \tag{A.0.17}$$

After doing Matsubara summation on the p_n frequencies we obtain,[21, 30, 32]

$$\Sigma^{(3)}(\mathbf{k}, \mathbf{k}', i\omega_n) = \frac{3J_K^3}{16} \sum_{\mathbf{k}_1, \mathbf{k}_2} \frac{1 - 2n_F(\xi_{\mathbf{k}_2})}{\xi_{\mathbf{k}_1} - \xi_{\mathbf{k}_2}} \frac{1}{i\omega_n - \xi_{\mathbf{k}_1}}. \tag{A.0.18}$$

Appendix B

RPA spin and charge fluctuations from the Hubbard model

Derivation of spin-fluctuation potential

One band Hubbard model is given by,

$$\begin{aligned}\mathcal{H} &= \sum_{\mathbf{k},\sigma} \xi_{\mathbf{k}} c_{\mathbf{k},\sigma}^\dagger c_{\mathbf{k},\sigma} + \sum_{\mathbf{k},\mathbf{k}',\mathbf{q}} U c_{\mathbf{k}+\mathbf{q},\uparrow}^\dagger c_{\mathbf{k}'-\mathbf{q},\downarrow}^\dagger c_{\mathbf{k}',\downarrow} c_{\mathbf{k},\uparrow}, \\ &= \mathcal{H}_0 + \mathcal{H}_I.\end{aligned}\tag{B.0.1}$$

The action in the path integral formalism is,

$$S = S_0 + S_I,\tag{B.0.2}$$

$$S_0 = \int_0^\beta d\tau \sum_{\mathbf{k},\sigma} \tilde{c}_{\mathbf{k}\sigma}(\tau) (\partial_\tau + \xi_{\mathbf{k}}) c_{\mathbf{k}\sigma}(\tau),\tag{B.0.3}$$

$$S_I = \int_0^\beta d\tau \sum_{\mathbf{k},\mathbf{k}',\mathbf{q}} \tilde{c}_{\mathbf{k}+\mathbf{q}\uparrow}(\tau) \tilde{c}_{\mathbf{k}'-\mathbf{q}\downarrow}(\tau) c_{\mathbf{k}'\downarrow}(\tau) c_{\mathbf{k}\uparrow}(\tau).\tag{B.0.4}$$

The partion function is given by,

$$\mathcal{Z}_0 = \int \mathcal{D}[\tilde{c}, c] e^{-S_0}, \quad (\text{B.0.5})$$

$$\begin{aligned} \mathcal{Z} &= \int \mathcal{D}[\tilde{c}, c] e^{-S}, \\ &= \mathcal{Z}_0 \langle e^{-S_I} \rangle_0. \end{aligned} \quad (\text{B.0.6})$$

Where the thermal average is defined as,

$$\langle \mathcal{F}[\tilde{c}_{\mathbf{k}\sigma}, c_{\mathbf{k}\sigma}] \rangle = \frac{\int \mathcal{D}[\tilde{c}, c] e^{-S} \mathcal{F}[\tilde{c}_{\mathbf{k}\sigma}, c_{\mathbf{k}\sigma}]}{\int \mathcal{D}[\tilde{c}, c] e^{-S}}, \quad (\text{B.0.7})$$

$$\langle \mathcal{F}[\tilde{c}_{\mathbf{k}\sigma}, c_{\mathbf{k}\sigma}] \rangle_0 = \frac{\int \mathcal{D}[\tilde{c}, c] e^{-S_0} \mathcal{F}[\tilde{c}_{\mathbf{k}\sigma}, c_{\mathbf{k}\sigma}]}{\int \mathcal{D}[\tilde{c}, c] e^{-S_0}}. \quad (\text{B.0.8})$$

Here, we use $\langle \dots \rangle_0$, to denote average is taken w.r.t \mathcal{H}_0 and $\beta = 1/k_B T$ is inverse temperature. We then expand Eq. (B.0.5) in series,

$$\begin{aligned} \frac{\mathcal{Z}}{\mathcal{Z}_0} &= \sum_{n=0}^{\infty} \frac{(-1)^n}{n!} \int_0^\beta d\tau_1 \dots d\tau_n \langle \mathcal{T}_\tau \mathcal{H}_I(\tau_1) \dots \mathcal{H}_I(\tau_n) \rangle_0, \\ &= 1 - \int d\tau \langle \mathcal{H}_I(\tau) \rangle_0 + \frac{1}{2} \int d\tau_1 d\tau_2 \langle \mathcal{T}_\tau \mathcal{H}_I(\tau_1) \mathcal{H}_I(\tau_2) \rangle_0 \\ &\quad - \frac{1}{3!} \int d\tau_1 d\tau_2 d\tau_3 \langle \mathcal{T}_\tau \mathcal{H}_I(\tau_1) \mathcal{H}_I(\tau_2) \mathcal{H}_I(\tau_3) \rangle_0 + \dots \end{aligned} \quad (\text{B.0.9})$$

The second-order term of the Eq.(B.0.9) is,

$$\begin{aligned} \left. \frac{\mathcal{Z}}{\mathcal{Z}_0} \right|_{n=2} &= \int d\tau_1 d\tau_2 \sum_{\substack{\mathbf{k}_1, \mathbf{k}'_1, \mathbf{q}_1 \\ \mathbf{k}_2, \mathbf{k}'_2, \mathbf{q}_2}} \left[\Gamma_2^p(\tau_1 - \tau_2) \langle \mathcal{T}_\tau \tilde{c}_{\mathbf{k}_1 + \mathbf{q}_1 \uparrow}(\tau_1) \tilde{c}_{\mathbf{k}'_1 - \mathbf{q}_1 \downarrow}(\tau_1) c_{\mathbf{k}'_2 \downarrow}(\tau_2) c_{\mathbf{k}_2 \uparrow}(\tau_2) \rangle_0 \right. \\ &\quad + \Gamma_2^T(\tau_1 - \tau_2) \langle \mathcal{T}_\tau \tilde{c}_{\mathbf{k}_1 + \mathbf{q}_1 \uparrow}(\tau_1) \tilde{c}_{\mathbf{k}'_2 - \mathbf{q}_2 \downarrow}(\tau_2) c_{\mathbf{k}'_1 \downarrow}(\tau_1) c_{\mathbf{k}_2 \uparrow}(\tau_2) \rangle_0 \\ &\quad \left. + \Gamma_2^{\uparrow\uparrow}(\tau_1 - \tau_2) n_{\mathbf{q}_1 \downarrow}(\tau_1) n_{\mathbf{q}_2 \downarrow}(\tau_2) + \Gamma_2^{\downarrow\downarrow}(\tau_1 - \tau_2) n_{\mathbf{q}_1 \uparrow}(\tau_1) n_{\mathbf{q}_2 \uparrow}(\tau_2) \right] \quad (\text{B.0.10}) \end{aligned}$$

We multiply by factor 2, ($\frac{1}{2} \times 2$), because entire second order vertex function is invariant under (1 \rightarrow 2) i.e., by relabelling all momentum and time label of the

graph.

$$\Gamma_2^p(\tau_1 - \tau_2) = U^2 \mathcal{G}_{\mathbf{k}_2 + \mathbf{q}_2, \uparrow}(\tau_1 - \tau_2) \mathcal{G}_{\mathbf{k}'_2 - \mathbf{q}_2, \downarrow}(\tau_1 - \tau_2) \delta_{\mathbf{k}'_2 - \mathbf{q}_2, \mathbf{k}'_1} \delta_{\mathbf{k}_1, \mathbf{k}_2 + \mathbf{q}_2}, \quad (\text{B.0.11})$$

$$\Gamma_2^T(\tau_1 - \tau_2) = U^2 \mathcal{G}_{\mathbf{k}_2 + \mathbf{q}_2, \uparrow}(\tau_1 - \tau_2) \mathcal{G}_{\mathbf{k}'_1 - \mathbf{q}_1, \downarrow}(\tau_2 - \tau_1) \delta_{\mathbf{k}'_2, \mathbf{k}'_1 - \mathbf{q}_1} \delta_{\mathbf{k}_1, \mathbf{k}_2 + \mathbf{q}_2}, \quad (\text{B.0.12})$$

Γ_2^p and Γ_2^T are particle-particle, particle-hole interaction vertex function. $\Gamma_2^{\uparrow\uparrow}/\Gamma_2^{\downarrow\downarrow}$ is the interaction vertex giving the second-order ladder diagram.

$$\begin{aligned} \Gamma_2^{\uparrow\uparrow}(\tau_1 - \tau_2) &= -U^2 \mathcal{G}_{\mathbf{k}_2 + \mathbf{q}_2, \uparrow}(\tau_1 - \tau_2) \mathcal{G}_{\mathbf{k}_1 + \mathbf{q}_1, \uparrow}(\tau_2 - \tau_1) \delta_{\mathbf{k}_1 + \mathbf{q}_1, \mathbf{k}_2} \delta_{\mathbf{k}_1, \mathbf{k}_2 + \mathbf{q}_2} \delta_{\mathbf{q}_1, -\mathbf{q}_2}, \\ \Gamma_2^{\downarrow\downarrow}(\tau_1 - \tau_2) &= -U^2 \mathcal{G}_{\mathbf{k}'_2 - \mathbf{q}_2, \downarrow}(\tau_1 - \tau_2) \mathcal{G}_{\mathbf{k}'_1 - \mathbf{q}_1, \uparrow}(\tau_2 - \tau_1) \delta_{\mathbf{k}'_1, \mathbf{k}'_2 - \mathbf{q}_2} \delta_{\mathbf{k}'_2, \mathbf{k}'_1 - \mathbf{q}_1} \delta_{\mathbf{q}_1, -\mathbf{q}_2}. \end{aligned} \quad (\text{B.0.13})$$

We define density operator,

$$n_{\mathbf{q}, \sigma} = \sum_{\mathbf{k}} \tilde{c}_{\mathbf{k} - \mathbf{q}, \sigma} c_{\mathbf{k}, \sigma}. \quad (\text{B.0.14})$$

Transverse and longitudinal Susceptibilities.

We define spin operator as,

$$\mathcal{S}^+(\mathbf{q}) = \sum_{\mathbf{k}} c_{\mathbf{k}, \uparrow}^\dagger c_{\mathbf{k} + \mathbf{q}, \downarrow}, \quad \mathcal{S}^-(\mathbf{q}) = \sum_{\mathbf{k}} c_{\mathbf{k}, \downarrow}^\dagger c_{\mathbf{k} + \mathbf{q}, \uparrow}, \quad \mathcal{S}^z(\mathbf{q}) = \sum_{\mathbf{k}} [c_{\mathbf{k}, \uparrow}^\dagger c_{\mathbf{k} + \mathbf{q}, \uparrow} - c_{\mathbf{k}, \downarrow}^\dagger c_{\mathbf{k} + \mathbf{q}, \downarrow}]. \quad (\text{B.0.15})$$

Transverse and longitudinal susceptibilities are defined as (unit $\hbar = 1$),

$$\chi^{+-}(\mathbf{q}, \tau - \tau') = \left\langle T_\tau \mathcal{S}^+(\mathbf{q}, \tau) \mathcal{S}^-(\mathbf{q}, \tau') \right\rangle, \quad \chi^{zz}(\mathbf{q}, \tau - \tau') = \left\langle T_\tau \mathcal{S}^z(\mathbf{q}, \tau) \mathcal{S}^z(-\mathbf{q}, \tau') \right\rangle. \quad (\text{B.0.16})$$

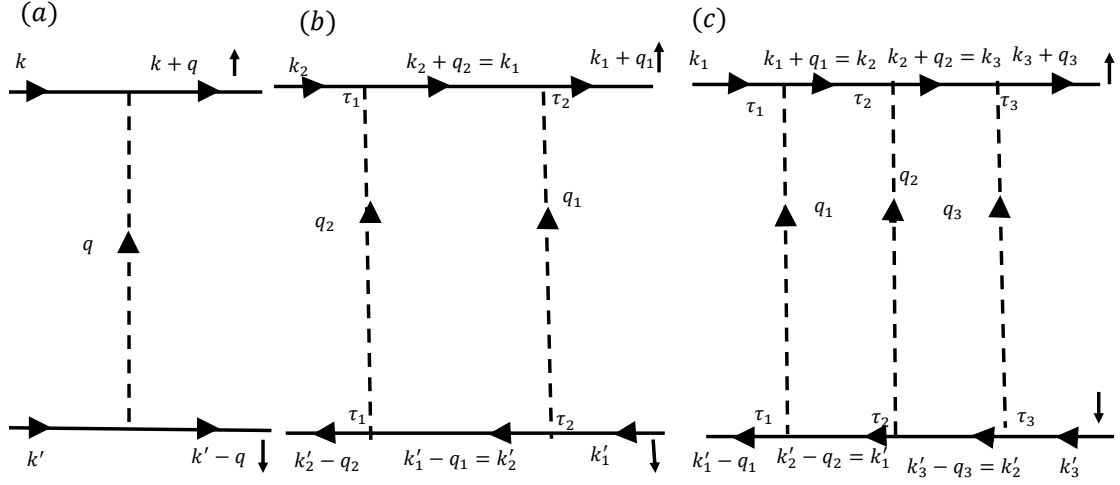


Figure B.1: (a), (b), (c) represents first, second, and third-order Feynman diagram.

$$\begin{aligned}
\chi^{+-}(\mathbf{q}, \tau - \tau') &= - \sum_{\mathbf{k}, \mathbf{k}'} \mathcal{G}_{\mathbf{k}+\mathbf{q}, \downarrow}(\tau - \tau') \mathcal{G}_{\mathbf{k}'-\mathbf{q}, \uparrow}(\tau' - \tau) \delta_{\mathbf{k}+\mathbf{q}, \mathbf{k}'}, \\
&= - \sum_{\mathbf{k}} \mathcal{G}_{\mathbf{k}+\mathbf{q}, \downarrow}(\tau - \tau') \mathcal{G}_{\mathbf{k}, \uparrow}(\tau' - \tau), \\
&= - \sum_{\mathbf{k}} \mathcal{G}_{\mathbf{k}-\mathbf{q}, \uparrow}(\tau' - \tau) \mathcal{G}_{\mathbf{k}, \downarrow}(\tau - \tau'). \tag{B.0.17}
\end{aligned}$$

$$\begin{aligned}
\chi^{zz}(\mathbf{q}, \tau - \tau') &= - \sum_{\mathbf{k}, \mathbf{k}'} \mathcal{G}_{\mathbf{k}+\mathbf{q}, \uparrow}(\tau - \tau') \mathcal{G}_{\mathbf{k}'-\mathbf{q}, \uparrow}(\tau' - \tau), \\
&= - \sum_{\mathbf{k}, \mathbf{k}'} \mathcal{G}_{\mathbf{k}+\mathbf{q}, \downarrow}(\tau - \tau') \mathcal{G}_{\mathbf{k}'-\mathbf{q}, \downarrow}(\tau' - \tau), \\
&= - \sum_{\mathbf{k}} \mathcal{G}_{\mathbf{k}+\mathbf{q}, \sigma}(\tau - \tau') \mathcal{G}_{\mathbf{k}, \sigma}(\tau' - \tau), \\
&= - \sum_{\mathbf{k}} \mathcal{G}_{\mathbf{k}-\mathbf{q}, \sigma}(\tau' - \tau) \mathcal{G}_{\mathbf{k}, \sigma}(\tau - \tau'). \tag{B.0.18}
\end{aligned}$$

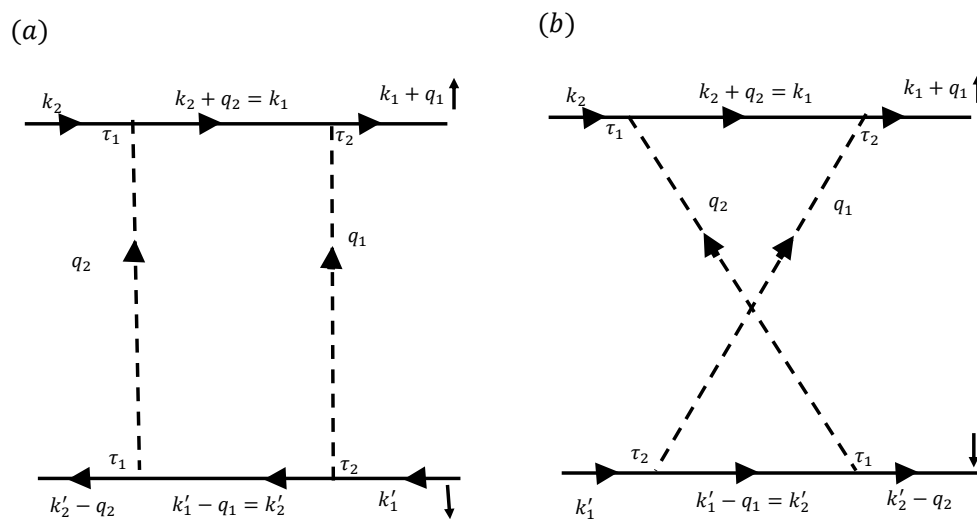


Figure B.2: (a), (b), represents second-order ladder diagram.

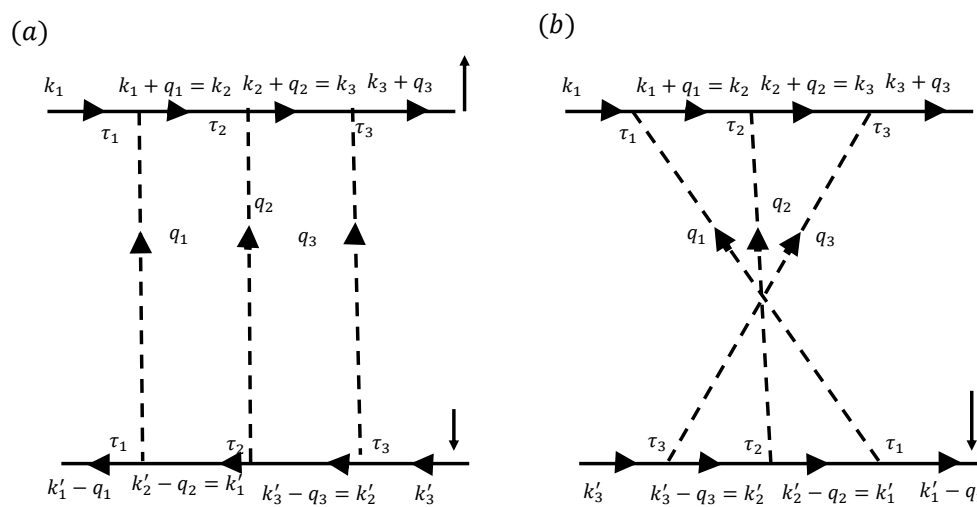


Figure B.3: (a) Feynmann diagram correspond to Eq. (B.0.23), (B.0.24). (b) Time direction has been reversed in the spin down channel.

Ladder diagrams

Second order

From Eq. (B.0.12)

$$\left. \frac{\mathcal{Z}}{\mathcal{Z}_0} \right|_{n=2}^{\text{2nd term}} = U^2 \int d\tau_1 d\tau_2 \sum_{\substack{\mathbf{k}_1, \mathbf{k}'_1, \mathbf{q}_1 \\ \mathbf{k}_2, \mathbf{k}'_2, \mathbf{q}_2}} \mathcal{G}_{\mathbf{k}_2 + \mathbf{q}_2, \uparrow}(\tau_1 - \tau_2) \mathcal{G}_{\mathbf{k}'_1 - \mathbf{q}_1, \downarrow}(\tau_2 - \tau_1) \delta_{\mathbf{k}'_2, \mathbf{k}'_1 - \mathbf{q}_1} \delta_{\mathbf{k}_1, \mathbf{k}_2 + \mathbf{q}_2},$$

$$\langle \mathcal{T}_\tau \tilde{c}_{\mathbf{k}_1 + \mathbf{q}_1 \uparrow}(\tau_1) \tilde{c}_{\mathbf{k}'_2 - \mathbf{q}_2 \downarrow}(\tau_2) c_{\mathbf{k}'_1 \downarrow}(\tau_1) c_{\mathbf{k}_2 \uparrow}(\tau_2) \rangle_0, \quad (\text{B.0.19})$$

The δ -function gives, (a) $\mathbf{k}_1 = \mathbf{k}_2 + \mathbf{q}_2$, (b) $\mathbf{k}'_2 = \mathbf{k}'_1 - \mathbf{q}_1$. This momentum conservation leads to four free momentum summation. We remove \mathbf{k}_1 and \mathbf{k}'_2 from Eq. (B.0.19), assuming $\mathbf{Q} = \mathbf{q}_1 + \mathbf{q}_2$

$$\left. \frac{\mathcal{Z}}{\mathcal{Z}_0} \right|_{n=2}^{\text{2nd term}} = U^2 \int d\tau_1 d\tau_2 \sum_{\substack{\mathbf{k}'_1, \mathbf{q}_1 \\ \mathbf{k}_2, \mathbf{Q}}} \mathcal{G}_{\mathbf{k}_2 + \mathbf{Q} - \mathbf{q}_1, \uparrow}(\tau_1 - \tau_2) \mathcal{G}_{\mathbf{k}'_1 - \mathbf{q}_1, \downarrow}(\tau_2 - \tau_1)$$

$$\langle \mathcal{T}_\tau \tilde{c}_{\mathbf{k}_2 + \mathbf{Q} \uparrow}(\tau_1) \tilde{c}_{\mathbf{k}'_1 - \mathbf{Q} \downarrow}(\tau_2) c_{\mathbf{k}'_1 \downarrow}(\tau_1) c_{\mathbf{k}_2 \uparrow}(\tau_2) \rangle_0, \quad (\text{B.0.20})$$

Using transverse susceptibility definition from Eq. (B.0.17),

$$\begin{aligned} \sum_{\mathbf{q}_1} \mathcal{G}_{\mathbf{k}_2 + \mathbf{Q} - \mathbf{q}_1, \uparrow}(\tau_1 - \tau_2) \mathcal{G}_{\mathbf{k}'_1 - \mathbf{q}_1, \downarrow}(\tau_2 - \tau_1) &= \sum_{\mathbf{q}_1} \mathcal{G}_{\mathbf{k}_2 + \mathbf{Q} + \mathbf{q}_1, \uparrow}(\tau_1 - \tau_2) \mathcal{G}_{\mathbf{k}'_1 + \mathbf{q}_1, \downarrow}(\tau_2 - \tau_1), \\ &= \sum_{\mathbf{q}_1} \mathcal{G}_{\mathbf{k}_2 + \mathbf{Q} + \mathbf{q}_1 - \mathbf{k}'_1, \uparrow}(\tau_1 - \tau_2) \mathcal{G}_{\mathbf{q}_1, \downarrow}(\tau_2 - \tau_1), \\ &= -\chi^{+-}(\mathbf{k}'_1 - \mathbf{k}_2 - \mathbf{Q}, \tau_2 - \tau_1). \end{aligned} \quad (\text{B.0.21})$$

Finally from Eq. (B.0.20)

$$\begin{aligned}
\frac{\mathcal{Z}}{\mathcal{Z}_0} \Big|_{n=2}^{\text{2nd term}} &= -U^2 \sum_{\mathbf{k}'_1, \mathbf{k}_2, \mathbf{Q}} \int d\tau_1 d\tau_2 \chi^{+-}(\mathbf{k}'_1 - \mathbf{k}_2 - \mathbf{Q}, \tau_2 - \tau_1) \langle \mathcal{T}_\tau \tilde{c}_{\mathbf{k}_2 + \mathbf{Q}\uparrow}(\tau_1) \\
&\quad \tilde{c}_{\mathbf{k}'_1 - \mathbf{Q}\downarrow}(\tau_2) c_{\mathbf{k}'_1\downarrow}(\tau_1) c_{\mathbf{k}_2\uparrow}(\tau_2) \rangle_0, \\
&= -U^2 \sum_{\mathbf{k}'_1, \mathbf{k}_2, \mathbf{Q}} \int d\tau_1 d\tau_2 \left(\chi^{+-}(\mathbf{k}'_1 + \mathbf{k}_2, \tau_2 - \tau_1) \right) \langle \mathcal{T}_\tau \tilde{c}_{-\mathbf{k}_2\uparrow}(\tau_1) \tilde{c}_{\mathbf{k}'_1 + \mathbf{Q}\downarrow}(\tau_2) \\
&\quad c_{\mathbf{k}'_1\downarrow}(\tau_1) c_{-\mathbf{k}_2 + \mathbf{Q}\uparrow}(\tau_2) \rangle_0, \\
&= -U^2 \sum_{\mathbf{k}, \mathbf{k}', \mathbf{q}} \int d\tau' d\tau \chi^{+-}(\mathbf{k}' + \mathbf{k}, \tau - \tau') \langle \mathcal{T}_\tau \tilde{c}_{-\mathbf{k}\uparrow}(\tau') \tilde{c}_{\mathbf{k}' + \mathbf{q}\downarrow}(\tau) \\
&\quad c_{\mathbf{k}'\downarrow}(\tau') c_{-\mathbf{k} + \mathbf{q}\uparrow}(\tau) \rangle_0.
\end{aligned} \tag{B.0.22}$$

Third order

From Eq.(B.0.9) third order term is given by,

$$\begin{aligned}
\frac{\mathcal{Z}}{\mathcal{Z}_0} \Big|_{n=3} &= \frac{1}{3!} \int d\tau_1 d\tau_2 d\tau_3 \langle \mathcal{T}_\tau \mathcal{H}_I(\tau_1) \mathcal{H}_I(\tau_2) \mathcal{H}_I(\tau_3) \rangle_0 \\
&= \int d\tau_1 d\tau_2 d\tau_3 \sum_{\substack{\mathbf{k}_1, \mathbf{k}'_1, \mathbf{q}_1 \\ \mathbf{k}_2, \mathbf{k}'_2, \mathbf{q}_2 \\ \mathbf{k}_3, \mathbf{k}'_3, \mathbf{q}_3}} \left[\Gamma_3^T(\tau_1, \tau_2, \tau_3) \langle -\mathcal{T}_\tau \tilde{c}_{\mathbf{k}_3 + \mathbf{q}_3\uparrow}(\tau_3) \tilde{c}_{\mathbf{k}'_1 - \mathbf{q}_1\downarrow}(\tau_1) c_{\mathbf{k}'_3\downarrow}(\tau_3) \right. \\
&\quad \left. c_{\mathbf{k}_1\uparrow}(\tau_1) \rangle_0 + \Gamma_3^L(\tau_1, \tau_2, \tau_3) \langle \mathcal{T}_\tau \tilde{c}_{\mathbf{k}_1 + \mathbf{q}_1\uparrow}(\tau_1) \tilde{c}_{\mathbf{k}'_3 - \mathbf{q}_3\downarrow}(\tau_3) c_{\mathbf{k}'_2\downarrow}(\tau_2) c_{\mathbf{k}_1\uparrow}(\tau_1) \rangle_0 \right],
\end{aligned} \tag{B.0.23}$$

where, the vertex function is,

$$\begin{aligned}
\Gamma_3^T(\tau_1, \tau_2, \tau_3) &= -U^3 \mathcal{G}_{\mathbf{k}'_2 - \mathbf{q}_2, \downarrow}(\tau_1 - \tau_2) \mathcal{G}_{\mathbf{k}_1 + \mathbf{q}_1, \uparrow}(\tau_2 - \tau_1) \mathcal{G}_{\mathbf{k}_2 + \mathbf{q}_2, \uparrow}(\tau_3 - \tau_2) \\
&\quad \mathcal{G}_{\mathbf{k}'_3 - \mathbf{q}_3, \downarrow}(\tau_2 - \tau_3) \delta_{\mathbf{k}'_2 - \mathbf{q}_2, \mathbf{k}'_1} \delta_{\mathbf{k}_1 + \mathbf{q}_1, \mathbf{k}_2} \delta_{\mathbf{k}_2 + \mathbf{q}_2, \mathbf{k}_3} \delta_{\mathbf{k}'_3 - \mathbf{q}_3, \mathbf{k}'_2},
\end{aligned} \tag{B.0.24}$$

The δ -function gives, (a) $\mathbf{k}'_1 = \mathbf{k}'_2 - \mathbf{q}_2$, (b) $\mathbf{k}_2 = \mathbf{k}_1 + \mathbf{q}_1$, (c) $\mathbf{k}_3 = \mathbf{k}_2 + \mathbf{q}_2$, (d) $\mathbf{k}'_2 = \mathbf{k}'_3 - \mathbf{q}_3$. We introduce new momentum (f) $\mathbf{Q} = \mathbf{q}_1 + \mathbf{q}_2 + \mathbf{q}_3$. This

term is shown in Fig.B.3. It is clear from the figure that for **irreducible diagrams** three time (τ_1, τ_2, τ_3) can be combined $3!$ ways, which cancel $3!$ in the denominator. From Eq. (B.0.23) we get,

$$\begin{aligned} \frac{\mathcal{Z}}{\mathcal{Z}_0} \Big|_{n=3}^{\text{1st term}} &= \sum_{\mathbf{k}'_3, \mathbf{k}_1, \mathbf{Q}} \int d\tau_1 d\tau_3 U^3 \left(\int d\tau_2 \chi^{+-}(\mathbf{k}'_3 - \mathbf{k}_1 - \mathbf{Q}, \tau_2 - \tau_3) \right. \\ &\quad \left. \chi^{+-}(\mathbf{k}'_3 - \mathbf{k}_1 - \mathbf{Q}, \tau_1 - \tau_2) \right) \langle \mathcal{T}_\tau \tilde{c}_{\mathbf{k}_3 + \mathbf{q}_3 \uparrow}(\tau_3) \tilde{c}_{\mathbf{k}'_1 - \mathbf{q}_1 \downarrow}(\tau_1) c_{\mathbf{k}'_3 \downarrow}(\tau_3) c_{\mathbf{k}_1 \uparrow}(\tau_1) \rangle_0, \end{aligned} \quad (\text{B.0.25})$$

where, we have used,

$$\begin{aligned} \sum_{\mathbf{q}_3} \mathcal{G}_{\mathbf{k}_2 + \mathbf{q}_2 \uparrow}(\tau_3 - \tau_2) \mathcal{G}_{\mathbf{k}'_3 - \mathbf{q}_3 \uparrow}(\tau_2 - \tau_3) &= \sum_{\mathbf{q}_3} \mathcal{G}_{\mathbf{k}_1 + \mathbf{Q} - \mathbf{q}_3 \uparrow}(\tau_3 - \tau_2) \mathcal{G}_{\mathbf{k}'_3 - \mathbf{q}_3 \uparrow}(\tau_2 - \tau_3), \\ &= \sum_{\mathbf{q}_3} \mathcal{G}_{\mathbf{k}_1 + \mathbf{Q} + \mathbf{q}_3 \uparrow}(\tau_3 - \tau_2) \mathcal{G}_{\mathbf{k}'_3 + \mathbf{q}_3 \uparrow}(\tau_2 - \tau_3), \\ &= \sum_{\mathbf{q}_3} \mathcal{G}_{\mathbf{k}_1 + \mathbf{Q} - \mathbf{k}'_3 + \mathbf{q}_3 \uparrow}(\tau_3 - \tau_2) \mathcal{G}_{\mathbf{q}_3 \uparrow}(\tau_2 - \tau_3), \\ &= -\chi^{+-}(\mathbf{k}'_3 - \mathbf{k}_1 - \mathbf{Q}, \tau_2 - \tau_3). \end{aligned} \quad (\text{B.0.26})$$

$$\begin{aligned} \sum_{\mathbf{q}_1} \mathcal{G}_{\mathbf{k}'_2 - \mathbf{q}_2 \downarrow}(\tau_1 - \tau_2) \mathcal{G}_{\mathbf{k}_1 + \mathbf{q}_1 \uparrow}(\tau_2 - \tau_1) &= \sum_{\mathbf{q}_1} \mathcal{G}_{\mathbf{k}'_3 - \mathbf{Q} + \mathbf{q}_1 \downarrow}(\tau_1 - \tau_2) \mathcal{G}_{\mathbf{k}_1 + \mathbf{q}_1 \uparrow}(\tau_2 - \tau_1), \\ &= \sum_{\mathbf{q}_1} \mathcal{G}_{\mathbf{k}'_3 - \mathbf{Q} + \mathbf{q}_1 - \mathbf{k}_1 \downarrow}(\tau_1 - \tau_2) \mathcal{G}_{\mathbf{q}_1 \uparrow}(\tau_2 - \tau_1), \\ &= -\chi^{+-}(\mathbf{k}'_3 - \mathbf{k}_1 - \mathbf{Q}, \tau_1 - \tau_2). \end{aligned} \quad (\text{B.0.27})$$

$$\begin{aligned}
\left. \frac{\mathcal{Z}}{\mathcal{Z}_0} \right|_{n=3}^{\text{1st term}} &= \sum_{\mathbf{k}'_3, \mathbf{k}_1, \mathbf{Q}} \int d\tau_1 d\tau_3 U^3 \left(\int d\tau_2 \chi^{+-}(\mathbf{k}'_3 - \mathbf{k}_1 - \mathbf{Q}, \tau_2 - \tau_3) \chi^{+-}(\mathbf{k}'_3 - \mathbf{k}_1 - \mathbf{Q}, \tau_1 - \tau_2) \right) \\
&\quad \langle \mathcal{T}_\tau \tilde{c}_{\mathbf{k}_1 + \mathbf{Q}\uparrow}(\tau_3) \tilde{c}_{\mathbf{k}'_3 - \mathbf{Q}\downarrow}(\tau_1) c_{\mathbf{k}'_3\downarrow}(\tau_3) c_{\mathbf{k}_1\uparrow}(\tau_1) \rangle_0, \\
&= \sum_{\mathbf{k}'_3, \mathbf{k}_1, \mathbf{Q}} \int d\tau_1 d\tau_3 U^3 \left(\int d\tau_2 \chi^{+-}(\mathbf{k}'_3 + \mathbf{k}_1, \tau_2 - \tau_3) \chi^{+-}(\mathbf{k}'_3 + \mathbf{k}_1, \tau_1 - \tau_2) \right) \\
&\quad \langle \mathcal{T}_\tau \tilde{c}_{-\mathbf{k}_1\uparrow}(\tau_3) \tilde{c}_{\mathbf{k}'_3 + \mathbf{Q}\downarrow}(\tau_1) c_{\mathbf{k}'_3\downarrow}(\tau_3) c_{-\mathbf{k}_1 + \mathbf{q}_1\uparrow}(\tau_1) \rangle_0, \\
&= \sum_{\mathbf{k}', \mathbf{k}, \mathbf{q}} \int d\tau d\tau' U^3 \left(\int d\tau'' \chi^{+-}(\mathbf{k}' + \mathbf{k}, \tau'' - \tau') \chi^{+-}(\mathbf{k}' + \mathbf{k}, \tau - \tau'') \right) \\
&\quad \langle \mathcal{T}_\tau \tilde{c}_{-\mathbf{k}\uparrow}(\tau') \tilde{c}_{\mathbf{k}' + \mathbf{q}\downarrow}(\tau) c_{\mathbf{k}'\downarrow}(\tau') c_{-\mathbf{k} + \mathbf{q}\uparrow}(\tau) \rangle_0. \tag{B.0.28}
\end{aligned}$$

We now add all ladder diagram upto infinite order ,

$$\begin{aligned}
&-U^2 \chi^{+-}(\mathbf{k}' + \mathbf{k}) - U^3 (\chi^{+-}(\mathbf{k}' + \mathbf{k})^2 - U^4 (\chi^{+-}(\mathbf{k}' + \mathbf{k}))^3 - \dots), \\
&= -U^2 \chi^{+-}(\mathbf{k}' + \mathbf{k}) \left(1 + U \chi^{+-}(\mathbf{k}' + \mathbf{k}) + \dots \right), \\
&= \frac{-U^2 \chi^{+-}(\mathbf{k}' + \mathbf{k})}{1 + U \chi^{+-}(\mathbf{k}' + \mathbf{k})}, \\
&= -\Gamma_{Ladder}^{RPA}(\mathbf{k}' + \mathbf{k}). \tag{B.0.29}
\end{aligned}$$

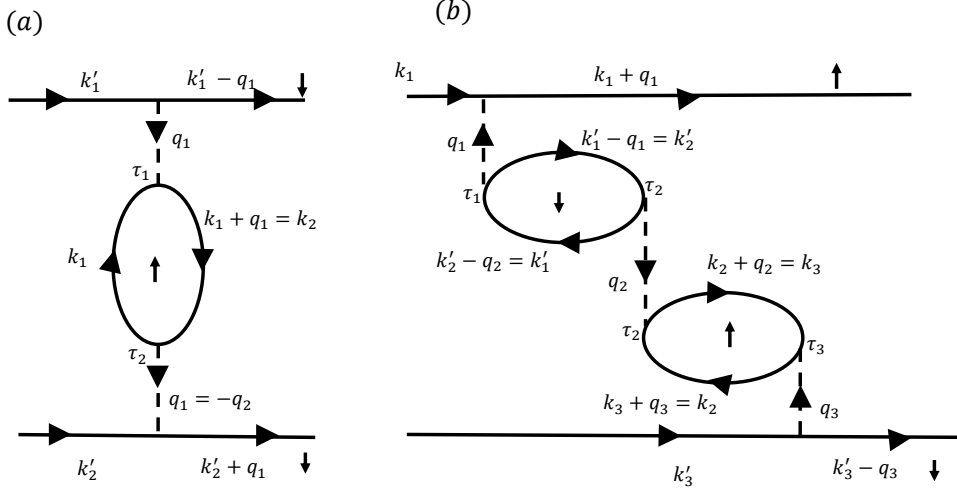


Figure B.4: (a) Feynman diagram correspond to Eq. (B.0.30).

Bubble diagrams

Bubble diagram calculated from Eq. (B.0.13)

$$\begin{aligned}
\frac{\mathcal{Z}}{\mathcal{Z}_0} \Big|_{n=2}^{\text{3rd term}} &= U^2 \int d\tau_1 d\tau_2 \sum_{\substack{\mathbf{k}_1, \mathbf{q}_1 \\ \mathbf{k}_2, \mathbf{q}_2}} \Gamma_2^{\uparrow\uparrow}(\tau_1 - \tau_2) \langle n_{\mathbf{q}_1\downarrow}(\tau_1) n_{\mathbf{q}_2\downarrow}(\tau_2) \rangle_0, \\
&= -U^2 \int d\tau_1 d\tau_2 \sum_{\substack{\mathbf{k}_1, \mathbf{q}_1 \\ \mathbf{k}_2, \mathbf{q}_2}} \mathcal{G}_{\mathbf{k}_2+\mathbf{q}_2, \uparrow}(\tau_1 - \tau_2) \mathcal{G}_{\mathbf{k}_1+\mathbf{q}_1, \uparrow}(\tau_2 - \tau_1) \delta_{\mathbf{k}_1, \mathbf{k}_2+\mathbf{q}_2} \delta_{\mathbf{q}_1, -\mathbf{q}_2} \\
&\quad \langle n_{\mathbf{q}_1\downarrow}(\tau_1) n_{-\mathbf{q}_1\downarrow}(\tau_2) \rangle_0, \\
&= -U^2 \int d\tau_1 d\tau_2 \sum_{\mathbf{k}_1, \mathbf{q}_1} \mathcal{G}_{\mathbf{k}_1, \uparrow}(\tau_1 - \tau_2) \mathcal{G}_{\mathbf{k}_1+\mathbf{q}_1, \uparrow}(\tau_2 - \tau_1) \langle n_{\mathbf{q}_1\downarrow}(\tau_1) n_{-\mathbf{q}_1\downarrow}(\tau_2) \rangle_0, \\
&= U^2 \int d\tau_1 d\tau_2 \sum_{\mathbf{q}_1} \chi^{zz}(\mathbf{q}_1, \tau_2 - \tau_1) \langle n_{\mathbf{q}_1\downarrow}(\tau_1) n_{-\mathbf{q}_1\downarrow}(\tau_2) \rangle_0, \\
&= -U^2 \int d\tau_1 d\tau_2 \sum_{\mathbf{k}'_1, \mathbf{k}'_2, \mathbf{q}_1} \chi^{zz}(\mathbf{q}_1, \tau_2 - \tau_1) \langle \mathcal{T}_\tau \tilde{c}_{\mathbf{k}'_1 - \mathbf{q}_1\downarrow}(\tau_1) \tilde{c}_{\mathbf{k}'_2 + \mathbf{q}_1\downarrow}(\tau_2) \\
&\quad c_{\mathbf{k}'_1\downarrow}(\tau_1) c_{\mathbf{k}'_2\downarrow}(\tau_2) \rangle_0.
\end{aligned} \tag{B.0.30}$$

Fig.B.4(a) shows first order bubble diagram.

Third order

$$\Gamma_3^L(\tau_1, \tau_2, \tau_3) = U^3 \mathcal{G}_{\mathbf{k}'_1 - \mathbf{q}_1, \downarrow}(\tau_2 - \tau_1) \mathcal{G}_{\mathbf{k}'_2 - \mathbf{q}_2, \downarrow}(\tau_1 - \tau_2) \mathcal{G}_{\mathbf{k}_2 + \mathbf{q}_2, \uparrow}(\tau_3 - \tau_2) \mathcal{G}_{\mathbf{k}_3 + \mathbf{q}_3, \uparrow}(\tau_2 - \tau_3) \delta_{\mathbf{k}'_2, \mathbf{k}'_1 - \mathbf{q}_1} \delta_{\mathbf{k}'_2 - \mathbf{q}_2, \mathbf{k}'_1} \delta_{\mathbf{k}_2 + \mathbf{q}_2, \mathbf{k}_3} \delta_{\mathbf{k}_3 + \mathbf{q}_3, \mathbf{k}_2}. \quad (\text{B.0.31})$$

The δ -function gives four conditions on momentum, (a) $\mathbf{k}'_2 = \mathbf{k}'_1 - \mathbf{q}_1$, (b) $\mathbf{k}'_2 - \mathbf{q}_2 = \mathbf{k}'_1$, (c) $\mathbf{k}_2 + \mathbf{q}_2 = \mathbf{k}_3$, (d) $\mathbf{k}_3 + \mathbf{q}_3 = \mathbf{k}_2$. These momentum conservations leads to (e) $\mathbf{q}_2 = -\mathbf{q}_1 = -\mathbf{q}_3$.

Therefore, from Eq. (B.0.30) we obtain,

$$\frac{\mathcal{Z}}{\mathcal{Z}_0} \Big|_{n=3}^{\text{2nd term}} = \sum_{\mathbf{k}_1, \mathbf{k}'_3, \mathbf{q}_1} \int d\tau_1 d\tau_3 U^3 \left(\int d\tau_2 \chi^{\downarrow\downarrow}(\mathbf{q}_1, \tau_1 - \tau_2) \chi^{\uparrow\uparrow}(\mathbf{q}_1, \tau_2 - \tau_3) \right) \langle \mathcal{T}_\tau \tilde{c}_{\mathbf{k}_1 + \mathbf{q}_1 \uparrow}(\tau_1) \tilde{c}_{\mathbf{k}'_3 - \mathbf{q}_1 \downarrow}(\tau_3) c_{\mathbf{k}'_3 \downarrow}(\tau_3) c_{\mathbf{k}_1 \uparrow}(\tau_1) \rangle_0. \quad (\text{B.0.32})$$

Using longitudinal susceptibility definition from Eq. (B.0.18),

$$\begin{aligned} \sum_{\mathbf{k}'_2} \mathcal{G}_{\mathbf{k}'_1 - \mathbf{q}_1, \downarrow}(\tau_2 - \tau_1) \mathcal{G}_{\mathbf{k}'_2 - \mathbf{q}_2, \downarrow}(\tau_1 - \tau_2) &= \sum_{\mathbf{k}'_2} \mathcal{G}_{\mathbf{k}'_2, \downarrow}(\tau_2 - \tau_1) \mathcal{G}_{\mathbf{k}'_2 + \mathbf{q}_1, \downarrow}(\tau_1 - \tau_2), \\ &= -\chi^{\downarrow\downarrow}(\mathbf{q}_1, \tau_1 - \tau_2), \end{aligned} \quad (\text{B.0.33})$$

$$\begin{aligned} \sum_{\mathbf{k}_3} \mathcal{G}_{\mathbf{k}_2 + \mathbf{q}_2, \uparrow}(\tau_3 - \tau_2) \mathcal{G}_{\mathbf{k}_3 + \mathbf{q}_3, \uparrow}(\tau_2 - \tau_3) &= \sum_{\mathbf{k}_3} \mathcal{G}_{\mathbf{k}_3, \uparrow}(\tau_3 - \tau_2) \mathcal{G}_{\mathbf{k}_3 + \mathbf{q}_3, \uparrow}(\tau_2 - \tau_3), \\ &= -\chi^{\uparrow\uparrow}(\mathbf{q}_3, \tau_1 - \tau_2). \end{aligned} \quad (\text{B.0.34})$$

Below we change label, (a) $\mathbf{k}_1 + \mathbf{q}_1 \rightarrow \mathbf{k}'_3$, (b) $\tau_3 \rightarrow \tau_1$

$$\begin{aligned}
\frac{\mathcal{Z}}{\mathcal{Z}_0} \Big|_{n=3}^{2\text{nd term}} &= \sum_{\mathbf{k}_1, \mathbf{k}'_3, \mathbf{q}_1} \int d\tau_3 d\tau_1 U^3 \left(\int d\tau_2 \chi^{\downarrow\downarrow}(\mathbf{k}'_3 - \mathbf{k}_1, \tau_3 - \tau_2) \chi^{\uparrow\uparrow}(\mathbf{k}'_3 - \mathbf{k}_1, \tau_2 - \tau_1) \right) \\
&\quad \langle \mathcal{T}_\tau \tilde{c}_{\mathbf{k}'_3\uparrow}(\tau_3) \tilde{c}_{-\mathbf{k}'_1+\mathbf{q}_1\downarrow}(\tau_1) c_{\mathbf{k}'_1\downarrow}(\tau_1) c_{-\mathbf{k}'_3+\mathbf{q}_1\uparrow}(\tau_3) \rangle_0, \\
&= \sum_{\mathbf{k}, \mathbf{k}', \mathbf{q}} \int d\tau' d\tau U^3 \left(\int d\tau'' \chi^{\downarrow\downarrow}(\mathbf{k}' - \mathbf{k}, \tau' - \tau'') \chi^{\uparrow\uparrow}(\mathbf{k}' - \mathbf{k}, \tau'' - \tau) \right) \\
&\quad \langle \mathcal{T}_\tau \tilde{c}_{\mathbf{k}'\uparrow}(\tau') \tilde{c}_{-\mathbf{k}+\mathbf{q}\downarrow}(\tau) c_{\mathbf{k}\downarrow}(\tau) c_{-\mathbf{k}'+\mathbf{q}\uparrow}(\tau') \rangle_0. \tag{B.0.35}
\end{aligned}$$

We add all bubble diagrams,

$$\begin{aligned}
&-U^3(\chi^{zz}(\mathbf{k}' - \mathbf{k}))^2 - U^5(\chi^{zz}(\mathbf{k}' - \mathbf{k}))^4 - U^7(\chi^{zz}(\mathbf{k}' - \mathbf{k}))^6 \dots \\
&= -U^3(\chi^{zz}(\mathbf{k}' - \mathbf{k}))^2 \left(1 + U^2(\chi^{zz}(\mathbf{k}' - \mathbf{k}))^2 + U^3(\chi^{zz}(\mathbf{k}' - \mathbf{k}))^4 + \dots \right), \\
&= -\frac{U^3(\chi^{zz}(\mathbf{k}' - \mathbf{k}))^2}{1 - U^3(\chi^{zz}(\mathbf{k}' - \mathbf{k}))^2}, \\
&= -\Gamma_{Bubble}^{RPA}(\mathbf{k}' - \mathbf{k}). \tag{B.0.36}
\end{aligned}$$

From Fig.B.5 we obtain spin-fluctuation potential,

$$\begin{aligned}
\Gamma^{RPA}(\mathbf{k}', \mathbf{k}) &= U + \Gamma_{Ladder}^{RPA}(\mathbf{k}' + \mathbf{k}) + \Gamma_{Bubble}^{RPA}(\mathbf{k}' - \mathbf{k}), \\
&= U + \frac{U^2 \chi^{+-}(\mathbf{k}' + \mathbf{k})}{1 + U \chi^{+-}(\mathbf{k}' + \mathbf{k})} + \frac{U^3 (\chi^{zz}(\mathbf{k}' - \mathbf{k}))^2}{1 - U^3 (\chi^{zz}(\mathbf{k}' - \mathbf{k}))^2}. \tag{B.0.37}
\end{aligned}$$

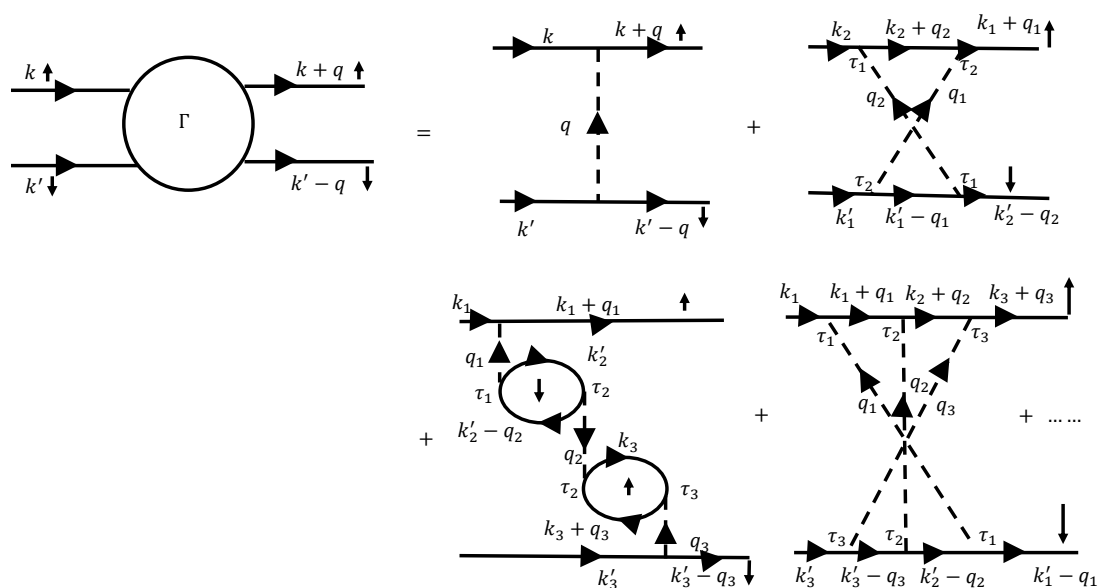


Figure B.5: Feynman diagrams of the Hubbard model for the spin-fluctuation mediated pairing strength. The incoming and outgoing solid lines represent fermionic operators, and the dashed line represents Coulomb interactions U . The circle on the left side of the figure is the effective interaction vertex potential. To the right side of the figure, the first diagram is the bare interaction, the second and fourth diagram is the second and third-order ladder diagrams, and the third diagram is called bubble diagram.

Bibliography

- [1] T Das, RS Markiewicz, A Bansil, Adv. Phys. **63**, 151 (2014).
- [2] G. R. Stewart, Rev. Mod. Phys. **73**, 797 (2001).
- [3] T. Das, and C. Panagopoulos, New J. Phys. **18**, 103033 (2016).
- [4] D. J. Scalapino, Rev. Mod. Phys. **84**, 1383 (2012).
- [5] C. M. Varma, Rev. Mod. Phys. **48**, 219 (1976).
- [6] J. Bardeen, L. N. Cooper, and J. R. Schrieffer, Phys. Rev. **108**, 1175 (1957).
- [7] W. Kohn, and J. M. Luttinger, Phys. Rev. Lett. **15**, 524 (1965).
- [8] D. J. Scalapino, Phys. Rep. **250**, 329 (1995).
- [9] D. J. Scalapino, Jr E. Loh, and J. E. Hirsch, Phys. Rev. B **35**, 13 (1987).
- [10] Fisk, Z and Sarrao, J L and Smith, J L and Thompson, J D, The physics and chemistry of heavy fermions. Proc. Nat. Acad. Sci. **92**, 15 (1995).
- [11] F. Steglich *et al* Phys. Rev. Lett. **43**, 1892 (1979).
- [12] Robert Joynt and Louis Taillefer, Rev. Mod. Phys. **74**, 235 (2002).
- [13] J.L. Sarrao and E.D. Bauer and J.N. Mitchell and P.H. Tobash and J.D. Thompson, Superconductivity in plutonium compounds. Physica C **514**, 184-188 (2015).
- [14] S. Nakatsuji *et al*, Nature Physics **4**, 603-607 (2008).

-
- [15] Okawa, M *et al*, Strong Valence Fluctuation in the Quantum Critical Heavy Fermion Superconductor β -YbAlB₄: A Hard X-Ray Photoemission Study. *Phys. Rev. Lett.* **104**, 247201 (2010).
- [16] Erwin Schuberth, *et al.*, Emergence of superconductivity in the canonical heavy-electron metal YbRh₂Si₂. *Science* **351**, 485-488 (2016).
- [17] P. W. Anderson, Localized Magnetic States in Metals, *Phys. Rev.* **124**, 41 (1961).
- [18] Piers Coleman, *Introduction to Many-Body Physics*, Cambridge University Press (2015).
- [19] Philip Phillips, *Advanced Solid State Physics*, Cambridge University Press (2012).
- [20] J. R. Schrieffer, and P. A. Wolff, *Phys. Rev.* **149**, 491 (1966).
- [21] Gerald D. Mahan, *Many-Particle Physics*, Springer (2008).
- [22] J. Kondo, *Prog. Theor. Phys.* **32**, 37 (1964).
- [23] A. Hewson, *The Kondo Problem to Heavy Fermions*, Cambridge University Press (1993).
- [24] S. Doniach, Kondo lattice and weak antiferromagnetism, *Physica B+C* **91**, 231 (1977).
- [25] M. A. Ruderman and C. Kittel, *Phys. Rev.* **78**, 99 (1950).
- [26] Tadao Kasuya, *Prog. Theor. Phys.* **16**, 1 (1956).
- [27] Kei Yosida, *Phys. Rev.* **106**, 893 (1957).
- [28] Neil Ashcroft and N. Mermin, *Solid State Physics*, Cengage (2003).
- [29] Alexander L. Fetter and John Dirk Walecka, *Quantum Theory of Many-Particle Systems*, Dover Publication (2012).

- [30] Henrik Bruus , Karsten Flensberg, Many-Body Quantum Theory in Condensed Matter Physics: An Introduction, Oxford Graduate Texts (2004).
- [31] Sarachik, M., E. Corenzwit, and L. D. Longinotti, Phys. Rev. **135**, A1041 (1964).
- [32] R.D. Mattuck, A Guide to Feynman Diagrams in the Many-body Problem, Dover Publications Inc. (1992).
- [33] K. G. Wilson, Rev. Mod. Phys. **47**, 773(1975).
- [34] Krishna-murthy, H. R., J. W. Wilkins, and K. G. Wilson, Phys. Rev. B **21**, 1003(1980); *ibid.* Phys. Rev. B **21**, 1044 (1980).
- [35] Ralf Bulla, Theo A. Costi, and Thomas Pruschke, Numerical renormalization group method for quantum impurity systems, Rev. Mod. Phys. **80**, 395(2008).
- [36] S. E. Barnes, J. Phys. F **6**, 1375 (1976); *ibid* J. Phys. F **7**, 2637 (1977).
- [37] Martin C. Gutzwiller, Phys. Rev. Lett. **10**, 159 (1963).
- [38] Martin C. Gutzwiller, Phys. Rev. **137**, A1726 (1965).
- [39] K. A. Chao, J. Spalek and A. M. Oles, Degenerate perturbation theory and its application to the Hubbard model, Phys. Lett. A **64**, 163 (1977).
- [40] K. A. Chao, J. Spalek, and A. M. Oleś, Kinetic exchange interaction in a narrow S-band, J. Phys. C **10**, L271 (1977).
- [41] Patrick A. Lee, Naoto Nagaosa, and Xiao-Gang Wen, Rev. Mod. Phys. **78**, 17 (2006).
- [42] J. Hubbard, Calculation of Partition Functions, Phys. Rev. Lett. **3**, 2 (1959).
- [43] R. L. Stratonovich, On a Method of Calculating Quantum Distribution Functions, Soviet Physics Doklady, **2** (1958).
- [44] T. Holstein and H. Primakoff, Phys. Rev. **58**, 1098 (1940).

- [45] Frésard, R. <https://www.cond-mat.de/events/correl15/manuscripts/fresard.pdf> (2015).
- [46] P. Coleman, Phys. Rev. B **29**, 3035 (1984).
- [47] Alexander Altland, Ben D. Simons, Condensed Matter Field Theory, Cambridge University Press (2010).
- [48] https://en.wikipedia.org/wiki/High-temperature_superconductivity.
- [49] Bednorz, J.G., Müller, K.A. Possible high T_c superconductivity in the Ba-La-Cu-O system. Z. Physik B - Condensed Matter **64**, 189–193 (1986).
- [50] M. K. Wu, J. R. Ashburn, C. J. Torng, P. H. Hor, R. L. Meng, L. Gao, Z. J. Huang, Y. Q. Wang, and C. W. Chu, Phys. Rev. Lett. **58**, 908 (1987).
- [51] Putilin, S. N., Antipov, E. V., Chmaissee, O. and Marezio, M. Nature **362**, 226–228 (1993).
- [52] Schilling, A., Cantoni, M., Guo, J. D. & Ott, H. R. Nature **363**, 56–58 (1993).
- [53] Xiaojia Chen and Changde Gong, Phys. Rev. B **59**, 4513 (1999).
- [54] M. Jarrell, T. Maier, M. Hettler, and A. Tahvildarzadeh, Europhys. Lett. **56**, 563 (2001).
- [55] A. Comanac, L. de' Medici, M. Capone, and A. Millis, Nat. Phys. **4**, 287 (2008).
- [56] Cédric Weber, Kristjan Haule, and Gabriel Kotliar, Nat. Phys. **6**, 574 (2010).
- [57] F. C. Zhang and T. M. Rice, Phys. Rev. B **37**, 3759(R) (1988).
- [58] Shengwei Zeng, Chi Sin Tang, Xinmao Yin, Changjian Li, Zhen Huang, Junxiong Hu, Wei Liu, Ganesh Ji Omar, Hariom Jani, Zhi Shiuh Lim, Kun Han, Dongyang Wan, Ping Yang, Andrew T. S. Wee, Ariando Ariando, arXiv:2004.11281.
- [59] D. Li, K. Lee, B. Y. Wang, M. Osada, S. Crossley, H. R. Lee, Y. Cui, Y. Hikita, H. Y. Hwang, Nature **572**, 624 (2019).

- [60] M. A. Hayward, M. A. Green, M. J. Rosseinsky, J. Sloan, *J. Am. Chem. Soc.* **121**, 8843 (1999).
- [61] V. I. Anisimov, D. Bukhvalov, and T. M. Rice, *Phys. Rev. B* **59**, 7901 (1999).
- [62] K.-W. Lee and W. E. Pickett, *Phys. Rev. B* **70**, 165109 (2004).
- [63] M. Hepting, D. Li, C. J. Jia, H. Lu, E. Paris, Y. Tseng, X. Feng, M. Osada, E. Been, Y. Hikita, Y.-D. Chuang, Z. Hussain, K. J. Zhou, A. Nag, M. Garcia-Fernandez, M. Rossi, H. Y. Huang, D. J. Huang, Z. X. Shen, T. Schmitt, H. Y. Hwang, B. Moritz, J. Zaanen, T. P. Devereaux, W. S. Lee, *Nature Materials*, **19**, 381-385 (2020).
- [64] Danfeng Li, Bai Yang Wang, Kyuho Lee, Shannon P. Harvey, Motoki Osada, Berit H. Goodge, Lena F. Kourkoutis, Harold Y. Hwang, *Phys. Rev. Lett.* **125**, 027001 (2020).
- [65] Motoki Osada, Bai Yang Wang, Kyuho Lee, Danfeng Li, and Harold Y. Hwang *Phys. Rev. Materials*, **4**, 121801(R) (2020).
- [66] S. W. Zeng, C. J. Li, L. E. Chow, Y. Cao, Z. T. Zhang, C. S. Tang, X. M. Yin, Z. S. Lim, J. X. Hu, P. Yang, and A. Ariando, arXiv:2105.13492.
- [67] Leon N. Cooper, *Phys. Rev.* **104**, 1189 (1956).
- [68] Michael Tinkham, *Introduction to Superconductivity*, Dover Publications Inc. (2004).
- [69] S. Maiti, and A. V. Chubukov, *AIP Conf. Proc.* **1550**, 373 (2013).
- [70] S. Raghu, S. A. Kivelson, and D. J. Scalapino, *Phys. Rev. B* **81**, 224505 (2010).
- [71] Tetsuya Takimoto, Takashi Hotta, and Kazuo Ueda, *Phys. Rev. B* **69**, 104504 (2004); K. Kubo, *Phys. Rev. B* **75**, 224509 (2007); T. Das, J.-X. Zhu, M. J. Graf, *Sci. Rep.* **5**, 8632 (2015). T. Nomoto, H. Ikeda, *Phys. Rev. Lett.* **117**, 217002 (2016); T. Nomoto, H. Ikeda, *J. Phys. Soc. Jpn.* **86**, 023703 (2017).

- [72] A. V. Chubukov, D. Pines, J. Schmalian, In: Bennemann K.H., Ketterson J.B. (eds) *The Physics of Superconductors*. Springer, Berlin, Heidelberg; T Das, RS Markiewicz, A Bansil, *Adv. Phys.* **63**, 151 (2014).
- [73] D. J. Scalapino, E. Loh, Jr., and J. E. Hirsch, *Phys. Rev. B* **34**, 8190 (R) (1986); *ibid* *Phys. Rev. B* **34**, 6420 (1986); J. R. Schrieffer, *Theory of Superconductivity* (W. A. Benjamin, New York) (1964); J. R. Schrieffer, X. G. Wen, and S. C. Zhang, *Phys. Rev. B* **39**, 11663 (1989); P. Monthoux, A. V. Balatsky, and D. Pines, *Phys. Rev. Lett.* **67**, 3448 (1991); M. Sigrist, and Kazuo Ueda, *Rev. Mod. Phys.* **63**, 239 (1991); J. C. Seamus Davis and Dung-Hai Lee, *PNAS* **110**, 17623-17630 (2013).
- [74] I. I. Mazin, D. J. Singh, M. D. Johannes, and M. H. Du, *Phys. Rev. Lett.* **101**, 057003S (2008); Zi-Jian Yao, Jian-Xin Li, and Z D Wang, *New J. Phys.* **11**, 025009 (2009); T. Das, A. V. Balatsky, *Phys. Rev. B* **84**, 014521 (2011); A. Chubukov, *Ann. Rev. Condens. Mat. Phys.* **3**, 57-92 (2012).
- [75] J. Schmalian, *Phys. Rev. Lett.* **81**, 4232 (1998); G. Saito, and Y. Yoshida, *Chem Rec* **11**, 124-145 (2011).
- [76] A. Bhattacharyya *et. al.*, *Phys. Rev. Lett.* **122**, 147001 (2019).
- [77] R. Nandkishore, Leonid Levitov, Andrey Chubukov, *Nat. Phys.* **8**, 158-163 (2012); Gia-Wei Chern, Rafael M. Fernandes, Rahul Nandkishore, Andrey V. Chubukov, *Phys. Rev. B* **86**, 115443 (2012); Sujay Ray, J. Jung, Tanmoy Das, *Phys. Rev. B* **99**, 134515 (2019).
- [78] N. Bulut and D.J. Scalapino, *J. Phys. Chem. Solids*, **54**, 10 (1993).
- [79] A. T. Rømer, *Spin-fluctuation mediated superconductivity and magnetic order in the cuprate $La_{1.88}Sr_{0.12}CuO_4$* . The Niels Bohr Institute, Faculty of Science, University of Copenhagen (2015).
- [80] T. Das, and K. Dolui, *Phys. Rev. B* **91**, 094510 (2015).
- [81] S. Graser, T. A. Maier, P. J. Hirschfeld, D. J. Scalapino, *New J. Phys.* **11**, 025016 (2009);

-
- [82] I. M. Vishik, Rep. Prog. Phys. **81**, 062501 (2018).
- [83] B. Keimer, S. A. Kivelson, M. R. Norman, S. Uchida, and J. Zaanen, Nature **518**, 179 (2015).
- [84] P. Monthoux, D. Pines, and G. Lonzarich, Nature **450**, 1177-1183 (2007).
- [85] G. W. Scheerer, *et al* npj Quantum Materials **3**, 41 (2018).
- [86] A. T. Holmes, and D. Jaccard, Physica B **378-380**, 339-342 (2006).
- [87] P. Coleman, and N. Andrei, J. Phys. Cond. Matter. **1**, 26 (1989).
- [88] K. Miyake, O. Narikiyo, and Y. Onishi, Physica B **259**, 676 (1999).
- [89] Y. Onishi, and K. Miyake, J. Phys. Soc. Jpn. **69**, 3955-3964 (2000).
- [90] R. Tazai, and H. Kontani, J. Phys. Soc. Jpn **88**, 063701 (2019).
- [91] R. Tazai, Y. Yamakawa, M. Tsuchiizu, and H. Kontani, J. Phys. Soc. Jpn. **86**, 073703 (2017).
- [92] O. Bodensiek, R. Zitko, and M. Vojta, M. Jarrell, and T. Pruschke, Phys. Rev. Lett. **110**, 146406 (2013).
- [93] R. Flint, A. H. Nevidomskyy, and P. Coleman, Phys. Rev. B **84**, 064514 (2011).
- [94] Y. Liu, G. M. Zhang, and L. Yu, Chin. Phys. Lett. **31**, 087102 (2014).
- [95] R. Flint, M. Dzero, P. Coleman, Nat. Phys. **4**, 643 - 648 (2008).
- [96] O. Erten, R. Flint, and P. Coleman, Phys. Rev. Lett. **114**, 027002 (2014).
- [97] R. Flint, and P. Coleman, Phys. Rev. Lett. **105**, 246404 (2010).
- [98] Z. P. Yin, A. Kutepov, and G. Kotliar, Phys. Rev. X **3**, 021011 (2013).
- [99] Y. Kitaoka, *et al*, J. Phys. Soc. Jpn. **55**, 723 (1986).
- [100] K. Ishida, *et al*, Phys. Rev. Lett. **82**, 5353 (1999).

-
- [101] K. Fujiwara, *et al.*, J. Phys. Soc. Jpn. **77**, 123711 (2008).
- [102] H.A. Vieyra, *et. al.*, Phys. Rev. Lett. **106**, 207001 (2011).
- [103] T. Das, A. B. Vorontsov, I. Vekhter, and M. J. Graf, Phys. Rev. B **87**, 174514 (2013).
- [104] O. Stockert, *et. al.* Nat. Phys **7**, 119-124 (2011).
- [105] Y. De Wilde, *et al.*, Phys. Rev. Lett. **72**, 2278 (1994).
- [106] Y. De Wilde, *et al.*, Physica C **235-240**, 1915 - 1916 (1994).
- [107] S. Kittaka, *et al.*, Phys. Rev. Lett. **112**, 067002 (2014).
- [108] S. Kittaka, *et al.*, Phys. Rev. B **94**, 054514 (2016).
- [109] T. Yamashita, *et al.*, Sci. Adv. **3**, e1601667 (2017).
- [110] G. Panga, *et al.*, Proc. Natl. Acad. Sci. **115**(21), 5343-5347 (2018).
- [111] T. Takenaka, *et al.*, Phys. Rev. Lett. **119**, 077001 (2017).
- [112] H.Q. Yuan, *et al.*, Science **302**, 2104-2107 (2003).
- [113] G. Seyfarth, *et al.*, Euro. Phys. Lett. **98**, 17012 (2012).
- [114] H. Kim, *et al.* Phys. Rev. Lett. **114**, 027003 (2015).
- [115] Y. Li *et al.*, Phys. Rev. Lett. **120**, 217001 (2018).
- [116] T. Hua, *et al.*, Proc. Nat. Acad. Sci. **110**, 7160 (2013).
- [117] D. M. Newns, and N. Read, Adv. Phys. **36**, 799 (1987).
- [118] N. Read, D. M. Newns, J. Phys. C **16**, L1055 (1983).
- [119] P. Gegenwart, Q. Si, and F. Steglich, Nat. Phys. **4**, 186-197 (2008).
- [120] P. Coleman, A. J. Schofield, Nature **433**, 226-229 (2005).
- [121] Y. F. Yang, D. Pines, Proc. Natl. Acad. Sci. **111**(51), 18178-18182 (2014).

- [122] H. Ikeda, M. T. Suzuki, and R. Arita, Phys. Rev. Lett. **114**, 147003 (2015).
- [123] C. Zhang, H.-F. Li, Yu Song, Y. Su, G. Tan, T. Netherton, C. Redding, S. V. Carr, O. Sobolev, A. Schneidewind, E. Faulhaber, L. W. Harriger, S. Li, X. Lu, D. Yao, T. Das, A. V. Balatsky, Th. Bruckel, J. W. Lynn, P. Dai, Phys. Rev. B **88**, 064504 (2013).
- [124] W. K. Park, L. H. Greene, J. L. Sarrao, and J. D. Thompson, AIP Conference Proceedings **850**, 715 (2006); *ibid.* Physica C **460-462**, 206-209 (2007); W. K. Park, J. L. Sarrao, J. D. Thompson, L. H. Greene, Phys. Rev. Lett. **100**, 177001 (2008).
- [125] S. Kitagawa, G. Nakamine, K. Ishida, H. S. Jeevan, C. Geibel, and F. Steglich, Phys. Rev. Lett. **121**, 157004 (2018).
- [126] W. L. McMillan, Phys. Rev. **167**, 331 (1968).
- [127] C. C. Tsuei and J. R. Kirtley, Rev. Mod. Phys. **72**, 969 (2000).
- [128] JR Kirtley, CC Tsuei, JZ Sun, CC Chi, Lock See Yu-Jahnes, A Gupta, M Rupp, MB Ketchen, Nature **373**, 225-228 (1995).
- [129] D. A. Wollman, D. J. Van Harlingen, W. C. Lee, D. M. Ginsberg, and A. J. Leggett, Phys. Rev. Lett. **71**, 2134 (1993); C. C. Tsuei, J. R. Kirtley, C. C. Chi, Lock See Yu-Jahnes, A. Gupta, T. Shaw, J. Z. Sun, and M. B. Ketchen, Phys. Rev. Lett. **73**, 593 (1994).
- [130] AG Loeser, Z-X Shen, DS Dessau, DS Marshall, CH Park, P Fournier, A Kapitulnik, Science **273**, 325-329 (1996); J Mesot, MR Norman, H Ding, M Randeria, JC Campuzano, A Paramekanti, HM Fretwell, A Kaminski, T Takeuchi, Takayoshi Yokoya, T Sato, T Takahashi, T Mochiku, K Kadowaki, Phys. Rev. Lett. **83**, 840 (1999); A. Damascelli, Zahid Hussain, and Zhi-Xun Shen, Rev. Mod. Phys. **75**, 473 (2003).
- [131] Makoto Hashimoto, Inna M. Vishik, Rui-Hua He, Thomas P. Devereaux, Zhi-Xun Shen, Nature Physics **10**, 483-495 (2014).

- [132] E. W. Hudson, S. H. Pan, A. K. Gupta, K.-W. Ng, J. C. Davis, *Science* **285**, 88-91 (1999); Ali Yazdani, C. M. Howald, C. P. Lutz, A. Kapitulnik, and D. M. Eigler, *Phys. Rev. Lett.* **83**, 176 (1999);
- [133] M.A. Hossain, J.D.F. Mottershead, A. Bostwick, J.L. McChesney, E. Rotenberg, R. Liang, W.N. Hardy, G.A. Sawatzky, I.S. Elfimov, D.A. Bonn, A. Damascelli *Nat. Phys.* **4**, 527 (2008).
- [134] D. Fournier, G. Levy, Y. Pennec, J.L. McChesney, A. Bostwick, E. Rotenberg, R. Liang, W.N. Hardy, D.A. Bonn, I.S. Elfimov, A. Damascelli *Nat. Phys.* **6**, 905 (2010).
- [135] V. B. Zabolotnyy, A. A. Kordyuk, D. Evtushinsky, V. N. Strocov, L. Patthey, T. Schmitt, D. Haug, C. T. Lin, V. Hinkov, B. Keimer, B. Behner, and S. V. Borisenko, *Phys. Rev. B* **85**, 064507 (2012).
- [136] W. N. Hardy, D. A. Bonn, D. C. Morgan, R. Liang, and K. Zhang, *Phys. Rev. Lett.* **70**, 3999-4002 (1993); R. Prozorov and R. W. Giannetta, Magnetic penetration depth in unconventional superconductors, *Supercond. Sci. Technol.* **19**, R41 (2006).;
- [137] A Rigamonti, F Borsa and P Carretta, *Rep. Prog. Phys.* **61**, 1367–1439 (1998).
- [138] D. N. Basov and T. Timusk, *Rev. Mod. Phys.* **77**, 721 (2005).
- [139] J.W.Loram, K.A.Mirza, J.R.Cooper, and J.L.Tallon, *Physica C*, **282-287**, 1405-1406 (1997).
- [140] R. Ocana, and P. Esquinazi, *Phys. Rev. B* **66**, 064525 (2002).
- [141] L. Taillefer, *Annu. Rev. Condens. Matter Phys.* **1**, 51-70 (2010).
- [142] D. H. Wu *et. al.*, *Phys. Rev. Lett.* **70**, 85 (1993); S. M. Anlage *et. al.*, *Phys. Rev. B.* **50**, 523 (1994).
- [143] A. Andreone *et. al.*, *Phys. Rev. B.* **49**, 6392 (1994).

- [144] C.W. Schneider, Z.H. Barber, J.E. Evetts, S.N. Mao, X.X. Xi, T. Venkatesan
Physica C, 233, 77 (1994).
- [145] L. Alff *et al.*, Eur. Phys. J. B **5**, 423 (1998); S. Kashiwaya *et al.*, Phys.
Rev. B. **57**, 8680 (1998).
- [146] J. A. Skinta *et al.*, Phys. Rev. Lett., **88**, 207005 (2002).
- [147] A. Snezhko *et al.*, Phys. Rev. Lett. **92**, 157005 (2004).
- [148] A. Biswas *et al.*, Phys. Rev. Lett. **88**, 207004 (2002).
- [149] M. M. Qazilbash *et al.*, Phys. Rev. B. **68**, 024502 (2003).
- [150] B. Chesca *et al.*, Phys. Rev. B. **71**, 104504 (2005).
- [151] Ariando *et al.*, Phys. Rev. Lett. **94**, 167001 (2005).
- [152] T. Das, R. S. Markiewicz, and A. Bansil, Phys. Rev. Lett **98**, 197004 (2007).
- [153] Qingshan Yuan, Xin-Zhong Yan, and C. S. Ting, Phys. Rev. B **74**, 214503
(2006).
- [154] A. Ino, C. Kim, M. Nakamura, T. Yoshida, T. Mizokawa, Z.-X. Shen, A.
Fujimori, T. Kakeshita, H. Eisaki, and S. Uchida, Phys. Rev. B **62**, 4137
(2000).
- [155] E. Razzoli, G. Drachuck, A. Keren, M. Radovic, N. C. Plumb, J. Chang,
Y.-B. Huang, H. Ding, J. Mesot, and M. Shi, Phys. Rev. Lett. **110**, 047004
(2013).
- [156] K. Tanaka, W. S. Lee, D. H. Lu, A. Fujimori, T. Fujii, Risdiana, I. Terasaki,
D. J. Scalapino, T. P. Devereaux, Z. Hussain, and Z.-X. Shen, Science **314**,
1910 (2006).
- [157] I. M. Vishik, *et al.* Proc. Nat. Acad. Sci. (USA) **109**, 18332 (2012).
- [158] Y. Peng, J. Meng, D.Mou, J. He, L. Zhao, Y.Wu, G. Liu, X. Dong, S. He,
J. Zhang, X. Wang, Q. Peng, Z. Wang, S. Zhang, F. Yang, C. Chen, Z. Xu, T.
K. Lee, X. J. Zhou, Nat. Commun. **4**, 2459 (2013).

- [159] K. M. Shen, *et al.*, Phys. Rev. B **69**, 054503 (2004).
- [160] D. Gustafsson, D. Golubev, M. Fogelström, T. Claeson, S. Kubatkin, T. Bauch, and F. Lombardi, Nat. Nanotechnology **8**, 25-30 (2013).
- [161] S. Sakai, and M. Civelli, JPS Conf. Proc. **3**, 015033 (2014) .
- [162] A. Go, and A. J. Millis, Phys. Rev. Lett. **114**, 016402 (2015).
- [163] W. Chen, G. Khaliullin, and O. P. Sushkov, Phys. Rev. B **80**, 094519 (2009).
- [164] A. M. Black-Schaffer, D. S. Golubev, T. Bauch, F. Lombardi, and M. Fogelström, Phys. Rev. Lett. **110**, 197001 (2013).
- [165] Y.-M. Lu, T. Xiang, and D.-H. Lee, Nat. Phys., **10**, 634–637(2014).
- [166] T. Das, arXiv:1312.0544.
- [167] Amit Gupta, and Debanand Sa, Eur. Phys. J. B **89**, 24 (2016).
- [168] I.S. Elfimov, G.A. Sawatzky, A. Damascelli, Phys. Rev. B **77**, 060504(R) (2008).
- [169] N. E. Hussey, M. Kibune, H. Nakagawa, N. Miura, Y. Iye, H. Takagi, S. Adachi and K. Tanabe, Phys. Rev. Lett. **80**, 2909 (1998); N. E. Hussey, H. Takagi, Y. Iye, S. Tajima, A. I. Rykov, and K. Yoshida, Phys. Rev. B **61**, 6475(R) (2000).
- [170] S. C. Riggs, O. Vafek, J. B. Kemper, J.B. Betts, A. Migliori, W. N. Hardy, Ruixing Liang, D. A. Bonn, G.S. Boebinger, Nat. Phys. **7**, 332 (2011).
- [171] Gang Xiao, M. Z. Cieplak, D. Musser, A. Gavrin, F. H. Streitz, C. L. Chien, J. J. Rhyne, and J. A. Gotaas, Nature **332**, 238-240 (1988).
- [172] Martin Magnuson, Thorsten Schmitt Vladimir N. Strocov, Justina Schlappa, Alex S. Kalabukhov, Laurent Duda, Sci. Rep. **4**, 7017 (2014).
- [173] G. Uimin, J. Rossat-Mignod, Physica C, **199**, 251-261 (1992).

- [174] A. Tavana, and M. Akhavan, *The European Physical Journal B* **73**, 79-83 (2010).
- [175] R. Combescot and X. Leyronas, *Phys. Rev. Lett.* **75**, 3732 (2005).
- [176] X. X. Xi, C. Doughty, A. Walkenhorst, C. Kwon, Q. Li, and T. Venkatesan, *Phys. Rev. Lett.* **68**, 1240 (1992).
- [177] T. Das, *Phys. Rev. B* **85**, 144510 (2012).
- [178] T. Das, *Phys. Rev. B* **86**, 064527 (2012).
- [179] W. A. Atkinson, *Phys. Rev. B* **59**, 3377 (1999).
- [180] S. Middey, unpublished data.
- [181] A. J. Achkar, R. Sutarto, X. Mao, F. He, A. Frano, S. Blanco-Canosa, M. Le Tacon, G. Ghiringhelli, L. Braicovich, M. Minola, M. Moretti Sala, C. Mazzoli, Ruixing Liang, D. A. Bonn, W. N. Hardy, B. Keimer, G. A. Sawatzky, and D. G. Hawthorn, *Phys. Rev. Lett.* **109**, 167001 (2012); Le Quy Doung, and T. Das, *Phys. Rev. B* **96**, 125154 (2017).
- [182] J. A. Sauls, *Adv. Phys.* **43**, 113 (1994); G. Yang and K. Maki, *Europhys. Lett.* **48** (2), 208-214 (1999).
- [183] Qing-Kun Tang, Lin Yang, Da Wang, Fu-Chun Zhang, and Qiang-Hua Wang, *Phys. Rev. B* **99**, 094521 (2019).
- [184] Hadi Goudarzi, Maryam Khezerlou, Hasan Sedghi, Afifeh Ghorbai, *Superlattices and Microstructures*, **104**, 1-9 (2017).
- [185] H.-h. Hung, W.-C. Lee, and C. Wu, *Phys. Rev. B* **83**, 144506 (2011).
- [186] Li Mao, J. Shi, Qian Niu, and C. Zhang, *Phys. Rev. Lett.* **106**, 157003 (2011).
- [187] S. Hesselmann, D. D. Scherer, M. M. Scherer, and S. Wessel, *Phys. Rev. B* **98**, 045142 (2018).

- [188] H. Won, Q. Yuan, P. Thalmeier, and K. Maki, *Braz. J. Phys.* **33**, 4 (2003).
- [189] T. Ishiguro and K. Yamaji, *Organic Superconductors* (Springer-Verlag, Berlin, 1990); G. M. Danner, W. Kang, and P. M. Chaikin, *Phys. Rev. Lett.* **72**, 3714 (1994); T. Sasaki and N. Toyota, *Phys. Rev. B* **49**, 10120 (1994).
- [190] M.A.Hayward and M.J.Rosseinsky, *Solid State Sci.* **5**, 839 (2003).
- [191] H. Sakakibara, H. Usui, K. Suzuki, T. Kotani, H. Aoki, K. Kuroki, arXiv:1909.00060.
- [192] X. Wu, D. D. Sante, T. Schwemmer, W. Hanke, H. Y. Hwang, S. Raghu, R. Thomale, *Phys. Rev. B* **101**, 060504(R) (2020).
- [193] J. Karp, A. S. Botana, M. R. Norman, H. Park, M. Zingl, A. Millis, arXiv:2001.06441
- [194] M. Kitatani, L. Si, O. Janson, R. Arita, Z. Zhong, K. Held, arXiv:2002.12230.
- [195] P. Jiang, *et al* arXiv:1909.13634.
- [196] Y. Gu, *et al.* arXiv:1911.00814
- [197] Y. Nomura *et al.* arXiv:1909.03942.
- [198] M. Osada, B. Y. Wang, B. H. Goodge, K. Lee, H. Yoon, K. Sakuma, D. Li, M. Miura, L. F. Kourkoutis, H. Y. Hwang, arXiv:2006.13369.
- [199] Y.-H. Zhang, and A. Vishwanath, arXiv:1909.12865.
- [200] J. Chang, J. Zhao, and Y. Ding, arXiv:1911.12731.
- [201] G.-M. Zhang, *et al.* arXiv: 1909.11845.
- [202] Priyo Adhikary, Subhadeep Bandyopadhyay, Tanmoy Das, Indra Dasgupta, and Tanusri Saha-Dasgupta, *Phys. Rev. B* **102**, 100501(R) (2020).
- [203] Subhadeep Bandyopadhyay, Priyo Adhikary, Tanmoy Das, Indra Dasgupta, Tanusri Saha-Dasgupta, *Phys. Rev. B* **102**, 220502(R)(2020).

- [204] Yusuke Nomura, Motoaki Hirayama, Terumasa Tadano, Yoshihide Yoshimoto, Kazuma Nakamura, and Ryotaro Arita Phys. Rev. B **100**, 205138 (2019).
- [205] A. S. Botana, M. R. Norman, Phys. Rev. X **10**, 011024 (2020).
- [206] In general, we find λ varies much more weakly with U_d , and U_s than with V_{sd} . However, at the quantitative level, the λ versus U_i plot depends on choice of V_{sd} . For small V_{sd} , λ tends to increase with both U_i , while for large V_{sd} , we see an opposite trend. The result suggests that V_{sd} presumably increases charge fluctuations faster than spin fluctuations. Since these two fluctuations have opposite sign in the pairing interaction (Eq. (1.6.11)), the increased charge fluctuation decreases the pairing interaction. In addition, charge fluctuation also decreases intra-orbital interactions U_i due to enhanced screening effect.
- [207] Byungkyun Kang, Corey Melnick, Patrick Semon, Gabriel Kotliar, Sangkook Choi, arXiv:2007.14610.
- [208] Gu *et al.*, Nat. Commun. **11**, 6027 (2020).
- [209] <https://www.radiochemistry.org/periodictable/la-series/A6.html>.
- [210] Mi-Young Choi and Kwan-Woo Lee, arXiv:1911.02999.
- [211] J. Zhang, Y.-S. Chen, D. Phelan, H. Zheng, M. R. Norman, J. F. Mitchell, Proc. Natl. Acad. Sci. USA **113**, 8945 (2016).
- [212] J. Zhang, A. S. Botana, J. W. Freeland, D. Phelan, H. Zheng, V. Pardo, M. R. Norman, J. F. Mitchell, Nat. Phys. **13**, 864 (2017).
- [213] D. Li, B. Y. Wang, K. Lee, S. P. Harvey, M. Osada, B. H. Goodge, L. F. Kourkoutis, H. Y. Hwang, arXiv:2003.08506.
- [214] Y. Wang, C.-J. Kang, H. Miao, and G. Kotliar, Phys. Rev. B **102**, 161118(R) (2020).